

ABSTRACT

Title of dissertation: Spatio-Temporal Dynamics of the Magnetosphere during Geospace Storms

Jian Chen
Doctor of Philosophy, 2007

Dissertation directed by: Dr. A. Surjalal Sharma
Department of Astronomy

Nonlinear dynamical models have become powerful tools for studying and forecasting magnetospheric dynamics driven by solar wind inputs. In this thesis, the techniques of phase space reconstruction from time series data are used to develop new methods for modeling and predicting the spatio-temporal dynamics of the magnetosphere. For these studies, new databases covering the solar maximum period were compiled to enable accurate modeling of the magnetosphere during intense geospace storms. The main contributions of the thesis are:

Weighted Mean Field Model and Its Application to the Intense Storms. The nonlinear dynamical models of the coupled solar wind-magnetosphere system derived from observational data yield efficient forecasts of space weather. An improved version of the mean field model, derived from a set of nearest neighbors in the phase space reconstructed from the data, was developed by assigning weights to the nearest neighbors. A new correlated database was compiled and used to model and forecast the geospace storms of October-November 2003 and April 2002, and resulted in improved forecasts of the intense storms.

Mutual Information Analysis of Spatio-Temporal Dynamics. The mutual information functions enable studies of the nonlinear correlations of dynamical systems. A high resolution database for a six month period of solar wind and ground-based magnetometer data from 12 high latitude stations was used to compute the mutual information functions representing the correlations inherent in the system. Using two different window lengths of 6 and 24 hr, the spatio-temporal dynamics was analyzed using these functions for the different stations. The spreads in the average mutual information show strong correlations with the solar wind changes and the time evolution of mutual information yields a westward expansion of the disturbed region, starting from the near midnight sectors.

Modeling and Predictions of Spatio-Temporal Dynamics of the Magnetosphere. The spatial structure of the magnetospheric dynamics is crucial to space weather forecasting. The database of the magnetic field perturbations at 39 magnetometers belonging to the IMAGE and CANOPUS during year 2002 was used to study the spatio-temporal structure. A longitudinal sampling process utilizing the daily rotation of Earth was used to construct a two-dimensional representation of the high latitude magnetic perturbations. The nonlinear model was used to predict the spatial structure of geomagnetic disturbances during geospace storms.

Results presented in this dissertation provide a comprehensive study of the magnetosphere using nonlinear data derived models. The new weighted mean field model, mutual information analysis and spatio-temporal dynamics advance our understanding of the solar wind-magnetosphere coupling. These results can be used to develop new and more detailed space weather forecasting tools.

Spatio-Temporal Dynamics of the Magnetosphere
during Geospace Storms

by

Jian Chen

Dissertation submitted to the Faculty of the Graduate School of the
University of Maryland, College Park in partial fulfillment
of the requirements for the degree of
Doctor of Philosophy
2007

Advisory Committee:
Dr. A. Surjalal Sharma, Chair
Dr. Parvez N. Guzdar
Dr. M. Coleman Miller
Dr. Dennis K. Papadopoulos
Dr. Rajarshi Roy
Dr. Robert S. Weigel

© Copyright by
Jian Chen
2007

To my parents and my wife who made it all possible

Acknowledgements

I thank my advisor A. Surja Sharma who supported my work and encouraged me to develop independently. I appreciate his encouragement, guidance and friendship. It's a lifelong enjoyable experience to work with him. Also, I want to thank Dennis Papadopoulos, Gennady Milikh and Juan Valdivia for their general guidance and advice as well as other member of Space Plasma Group. A very special thanks to Xi Shao for numerous suggestions and countless hours of conversations.

I thank CDAWeb for the WIND and ACE data of year 2001, also thank IMAGE and CANOPUS for the ground magnetometer measurements. I thank Aaron Ridley for the *AL* data of year 2001.

I thank R. M. Skoug for solar wind SWEFAM data and G. Lu for the *AL* data of November superstorms of year 2003, and both for many fruitful discussions.

This work was supported in part by NSF grants ATM-0318629 and DMS-0417800.

Table of Contents

List of Tables	vi
1 Introduction	1
2 Solar Wind-Magnetosphere Coupling: Data Derived and Global MHD Models	11
2.1 Magnetospheric Dynamics during Substorms	12
2.2 Global and Multi-scale Phenomena of the Magnetosphere	14
2.3 Summary	20
3 Nonlinear Dynamical Techniques for Driven Systems	23
3.1 Linear Prediction Filter	23
3.2 Nonlinear Dynamical Studies Using Time Series Data	26
3.3 Time Delay and Embedding Dimension	32
3.3.1 Mutual Information Function	33
3.3.2 Correlation Integral	35
3.3.3 Singular Spectrum Analysis	40
3.4 Phase Space Reconstruction	41
3.5 Nonlinear Input-Output Modeling of the Magnetosphere	45
3.5.1 Nonlinear Moving Average Filter	46
3.6 Low-Dimensional Models with Specified Processes	55
3.7 New Database for Spatio-Temporal Dynamics during Active Periods .	57
3.8 Summary	58
4 Modeling and Prediction of the Magnetospheric Dynamics During Intense Geospace Storms	61
4.1 Introduction	61
4.2 Correlated Database of Solar Wind-Magnetosphere Coupling under Strong Driving	62
4.2.1 Year 2001 Storm Database for Solar Maximum Period	62
4.2.2 The Intense Geospace Storms during October-November 2003 and April 2002	66
4.3 Local-Linear Weighted Mean Filter	68
4.4 Modeling and Prediction During Superstorms	69
4.4.1 October-November 2003 Superstorms	69
4.4.2 April 2002 Superstorm	78
4.4.3 Comparison of Predictions using Bargatze <i>et al.</i> [1985] and Year 2001 databases	81
4.5 Discussion	86

5	Spatio-Temporal Dynamics of the Magnetosphere During Geospace Storms: Mutual Information Analysis	91
5.1	Introduction	91
5.2	Mutual Information Function and Spatially Distributed Geospace Data	93
5.2.1	Average Mutual Information	94
5.2.2	Localized Integrated Mutual Information	97
5.3	Database of Spatio-Temporal Variability of the Magnetosphere	99
5.4	Average Mutual Information Analysis of Magnetospheric Dynamics	102
5.4.1	Analysis with Window Length $w = 24$ hour	104
5.4.2	Substorm Dynamics from LIM1 with Window Length $w = 6$ hour	110
5.4.3	Longer Time Scale Features of LIM1	114
5.5	Spatio-Temporal Dynamics Averaged over 6 and 24 hr Windows	116
6	Spatial Structure of the High Latitude Magnetic Perturbations	124
6.1	Introduction	124
6.2	Database of Solar Wind-Magnetosphere Coupling	127
6.3	Spatial Structure from High Latitude Measurements	130
6.3.1	Partition of Distributed Magnetometer Data	137
6.4	Discussion	146
7	Summary	149
	Bibliography	156

List of Tables

2.1	Key observed features of the solar wind, ionosphere and different regions of magnetosphere during substorms	15
3.1	Ground Magnetometer Stations	60
4.1	Comparison between BBMH [<i>Bargatze et al.</i> , 1985] and Year 2001 databases	66
4.2	Intensities of October 2003, November 2003, and April 2002 storms	79
4.3	The normalized mean square error (NMSE) of the predictions of all three storms using the BBMH, Year 2001 and combined databases. Both the NMSE of the whole event and of the main phases are shown	84
5.1	Auroral Magnetometer Stations	106

Chapter 1

Introduction

Above the Earth's atmosphere, there is a vast region extending into interplanetary space that is permeated by highly fluctuating magnetic fields, plasma and energetic particles. The collective, often violent, changes in space environment of Earth driven by the solar wind are commonly referred to as space weather. Variations in the solar wind plasma density, flow velocity, the direction of the interplanetary magnetic field (IMF), etc. cause significant changes throughout the Earth's magnetosphere, ionosphere, and on the ground with severe consequences in our technological infrastructure [*Baker et al.*, 1998]. In the recent several decades, humans have increasingly used space-based assets for navigation, communication, military reconnaissance and exploration. Changes in the currents flowing through the ionosphere can cause disruption to power distribution systems, long-line telephone networks, radio communications, and corrosion of pipelines on the ground. Changes in the radiation environment near Earth can seriously affect satellite operations through spacecraft charging and generation of false commands. Thus with more satellites launched into space, more reliance on wired and wireless communication, understanding and predicting the geospace environment is becoming increasingly important. Space weather and its predictability has now become a focus of magnetospheric physics.

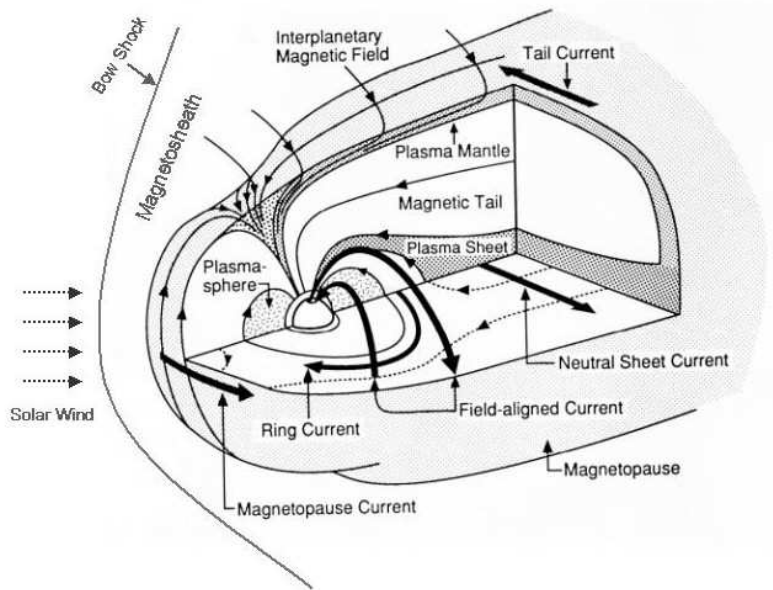


Figure 1.1: Three dimensional view of the Earth’s magnetosphere and the associated currents, fields and plasma regions (From *Kivelson and Russell* [1995].)

The solar wind couples to the magnetosphere and ionosphere at higher latitudes. Figure 1.1 shows schematically a three dimensional view of Earth’s magnetosphere and the associated currents, fields and plasma regions. The magnetosphere-ionosphere-atmosphere system is complicated and constitutes a highly coupled system.

A fascinating and easily observed manifestation of the solar wind-magnetosphere coupling is the aurora. Figure 1.2 shows a picture of an auroral display taken above Alaska. Earth’s magnetic field acts as “wires” to transmit the solar wind energy to the ionosphere, where the energy is dissipated mainly as heat, and to accelerate charged particles circling fairly close to Earth. The ionosphere in the northern and southern regions acts as the primary resistor in the circuit that is responsible for

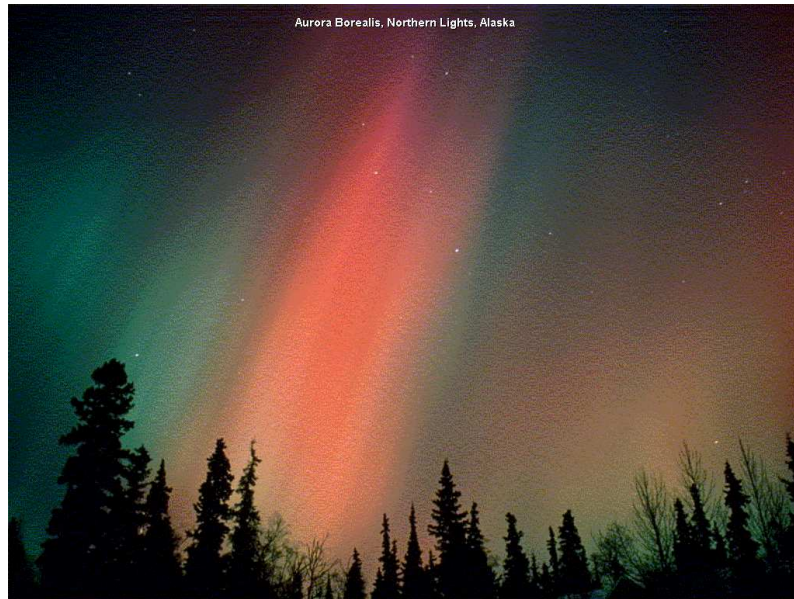


Figure 1.2: Picture of an auroral display taken above Alaska (From www.webshots.com).

the aurora. The auroral radiation is emitted by atmospheric constituents that are excited by particles precipitating from the magnetosphere.

As depicted in Figure (1.1), the solar wind flow brings energy and momentum to Earth. The presence of Earth's magnetic field prevents direct entry of the solar wind through the outer boundary of the magnetosphere, the magnetopause, and the solar wind is deflected around it after having been slowed down to sub-Alfvénic velocities by the Earth's bow shock. Earth's magnetic field is sufficiently strong that it can usually keep the solar wind from approaching closer than about 10 Earth radii (R_E). The boundary between the magnetosphere and the solar wind is the magnetopause. The region between the bow shock and the magnetopause is the magnetosheath. The kinetic pressure of the shocked solar wind compresses the

dipolar terrestrial magnetic field and, on the nightside of Earth, transforming it into a long, tail-like structure, the magnetotail. The tail lobe of the magnetotail consists of two regions with nearly antiparallel magnetic fields. The transition region is called the neutral sheet. The central part of the magnetotail, in the neighborhood of the neutral sheet, is populated with plasma with energies of several KeV. This region, the plasma sheet, is connected to the auroral ionosphere along magnetic field lines. Closer to Earth, energetic ions with energies of some tens of KeV oscillate between the converging magnetic fields in the northern and southern ionosphere and drift westward under the influence of gradient and curvature drift. The westward drift constitutes a considerable current encircling Earth at radial distance of several R_E , and is called the ring current.

The direction of the solar wind interplanetary magnetic field (IMF) is a controlling factor on the configuration of Earth's magnetosphere. The solar wind-magnetosphere coupling is enhanced when the IMF turns southward, a portion of the transferred energy accumulates in the magnetotail and is often explosively released in a process called magnetospheric substorm. The magnetosphere is a highly dynamic system under these conditions and the magnetospheric substorms are the elementary disturbances with a typical time scale of an hour. When the IMF remains southward for an extended interval, the energy transfer from the solar wind into magnetosphere continues over extended periods of time and the ring current grows under the influence of the solar wind variations, leading to geospace storms with typical time scales of days, and are characterized by strong decreases in the surface magnetic field. The extremes of space weather occur when intense solar ac-

tivity is strongly coupled to the solar wind-magnetosphere-ionosphere system during geospace storms.

The Earth's magnetosphere is a non-autonomous dynamical system, driven by the solar wind. Studies of the magnetospheric dynamics using dynamical models derived from correlated databases of the solar wind - magnetosphere system have enhanced our understanding of the complex behavior of the magnetosphere.

The evolution of a dynamical system is described by a trajectory in an appropriately defined state space and such a trajectory characterizes the system completely. Recent developments in dynamical systems theory can be used to obtain these trajectories from observational data, thus yielding a good understanding of the system dynamics, and leading to predictive capability. This dynamical model derived from data is referred to as data derived model and has given a new framework for describing the complex behavior of the magnetosphere. The advantage of this model based on the observational data is its ability to yield the inherent dynamics, independent of modeling assumptions. The global dynamical nature of the magnetosphere is evident from its phenomenology [*Siscoe, 1991*], from the global MHD simulations [*Lyon, 2000*] and from dynamical studies using observational data [*Sharma, 1995*]. The data derived models have led to considerable progress in the modeling and forecasting of the solar wind-magnetosphere coupling as an input-output system.

One of the earliest methods used to analyze the solar wind-magnetosphere coupling is the linear prediction filter, which assumes a linear relationship between the input time series $I(t)$ (solar wind convective electric field VB_S) and output time

series $O(t)$ (geomagnetic activity index AE or AL)(details see Chapter 3). Many studies have shown that the linear analysis alone is not sufficient to describe the complex behavior from the coupling of the solar wind and magnetosphere [*Baker et al.*, 1990; *Vassiliadis and Klimas*, 1995]. The nonlinear dynamical approach has been used to yield a new insight into the behavior of the magnetosphere during geomagnetic storms and substorms [*Vassiliadis et al.*, 1990; *Sharma*, 1995]. These studies have established the nonlinear dynamical behavior of the magnetosphere, in spite of being driven by the turbulent solar wind. These results are further strengthened by the good agreement between the data derived models and global MHD simulations [*Shao et al.*, 2003].

The application of the phase space reconstruction techniques to the auroral electrojet index AE , which is among the most widely used indices in the study of substorms, showed evidence that the global dynamics represented by AE time series is low dimensional [*Vassiliadis et al.*, 1990]. In this low dimensional state the dynamical behavior can be described by a small number of variables, and this implies that the magnetosphere is predictable. This has stimulated the study of forecasting substorms [*Vassiliadis et al.*, 1995; *Weigel et al.*, 1999], storms [*Valdivia et al.*, 1996], and space weather in general.

The nonlinear dynamical techniques have been used to develop models for several types of magnetospheric and ionospheric activities. The simplest form of this prediction technique is the local-linear technique, which uses only the linear term in an expansion around the initial conditions. Considering the solar wind - magnetosphere to be an input - output system, the phase space is reconstructed using the

geomagnetic indices and the solar wind data [Vassiliadis et al., 1992; Price et al., 1994; Valdivia et al., 1995; Vassiliadis et al., 1995a]. In this reconstructed space, the time evolution is characterized by trajectories computed from the data by time delay embedding [Packard et al., 1980; Takens, 1981; Abarbanel et al., 1993]. A collection of neighboring points in this phase space evolves in a similar fashion, and the evolution of a specified initial condition is then determined by its nearest neighbors. The high degree of predictability of these models gave strong evidence that nonlinear models can be used to develop accurate and reliable forecasting tools for space weather. Recent studies using time series data have shown that the coherence on the global magnetospheric scale can be obtained by averaging over the dynamical scales. A model for the global features can be obtained by a mean field technique of averaging outputs corresponding to similar states of the system in the reconstructed phase space [Ukhorskiy et al., 2002, 2004]. The mean field model was used to obtain the center of mass by a simple averaging of all the states in the specified NN nearest neighbors around the current state. Under the mean field model, it is assumed that all of the nearest neighbors should be within similar distances from the center of mass of the nearest neighbors. However the states close to the current state should be expected to contribute more than those farther away in deciding the predicted state. Based on this recognition, the weighted mean field filter based on the mean field filter is proposed to improve the accuracy and efficiency of predictions [Chen and Sharma, 2006]. This technique takes into account the distances of the nearest neighbors to the center of mass, and a set of weight factors which depend inversely on the distances of each nearest neighbor from the mass center are introduced. The

neighbors closer to the center of mass contribute more than those farther away, thus yield improved predictions.

During geomagnetically active periods, the global response has been studied extensively using nonlinear dynamical techniques [*Valdivia et al.*, 1996; *Ukhorskiy et al.*, 2002; *Chen and Sharma*, 2006]. However, the global features of magnetosphere are in general captured by the geomagnetic indices. For example, the auroral electrojet index AL , used in the studies of substorms, is the lower envelope of the combined plots of the magnetic field variations at the designated magnetometer stations in the auroral region [*Mayaud*, 1984], and thus has no spatial dependence. Similarly, the Dst index, used in the studies of geospace storm, is an average of the magnetic field variations at the mid-latitude stations and is thus a global index.

However the regional and local features measured by spacecraft-based imagers and ground-based instruments are essential for advancing our understanding of the magnetosphere. The importance of understanding the spatial structure of magnetosphere has led to the development of dynamical models based on the data from the magnetometer stations [*Valdivia et al.*, 1999a,b]. Thus the spatial structure of geomagnetic activity is the next key issue that would enable the understanding of the dynamics of the different regions. This is a prerequisite to developing the capability to make regional forecasts of space weather. At the same time, recognizing the nonlinear nature of the magnetosphere and its evident complexity, it is essential to use functions which can reveal the more complicated dependence. The average mutual information is an effective measure of correlation on the spatial distribution structure than the commonly used linear autocorrelation functions for a spatially

extended time series data [Chen *et al.*, 2007]. The studies of other nonlinear dynamical systems [Fraser and Swinney, 1986; Roulston, 1999] also conclude that the average mutual information has a more general applicability than previously recognized and can be used to yield new details of large scale open systems, such as the magnetosphere.

Although the studies using geomagnetic indices [Price *et al.*, 1994; Vassiliadis *et al.*, 1995a; Ukhorskiy *et al.*, 2002, 2004; Chen and Sharma, 2006] have shown the potential of nonlinear time series analysis in yielding predictive models, they lack the spatial dependence of the magnetospheric dynamics. The importance of understanding the spatial structure of geospace disturbances has led to the development of dynamical models based on the data from the magnetometer stations distributed around the globe. Valdivia *et al.* [1999a] modeled the evolution of the spatial structure of the ring current using the time series data from six mid-latitude ground magnetometers. A similar approach led to a two dimensional representation of the high latitude geomagnetic perturbations in magnetic latitude and magnetic local time from 15 magnetometers of the IMAGE magnetometer array [Valdivia *et al.*, 1999b]. These models however lack the ability to predict, due mainly to the limited data used to develop the models.

Recognizing the need for extensive data in building the models, large databases from the magnetometers in the CANOPUS and IMAGE chain is compiled for the periods of strong geomagnetic activity at all local times. This database is then used to reconstruct regional dynamical models of substorms, covering both latitude and longitude. Such a two-dimensional model is reconstructed in the same way as

the nonlinear filter techniques, e.g. the local input-output filters, but taking into consideration different local times.

The following chapters present the research results of this dissertation: The phenomenology of solar wind-magnetosphere coupling is reviewed in Chapter 2, with emphasis on the global and multi-scale properties of magnetospheric dynamics during substorms. Chapters 3 - 6 comprise the main body of the thesis. Chapter 3 discusses the applications of the new nonlinear techniques on the well known Lorenz attractor, the observational data of AE index, and the prediction using the local linear filter methods. Chapter 4 discusses an improved filter, the weighted mean field filter, and its applications on three intense storms in years 2002 and 2003. In Chapter 5, the mutual information function is used to study the inherently nonlinear spatial dynamics of the magnetosphere through a spatially extended time series data. In Chapter 6, the time series data of the distributed observations are used to develop spatio-temporal dynamics of the magnetosphere using phase space reconstruction techniques. The nonlinear model is used to predict the spatial structure of geomagnetic disturbances during geospace storms. The main results are summarized in Chapter 7.

Chapter 2

Solar Wind-Magnetosphere Coupling: Data Derived and Global MHD Models

Observations have shown that the direction of solar wind interplanetary magnetic field (IMF) has a controlling role on the configuration of Earth's magnetosphere. This is because the coupling between the solar wind and the magnetosphere is controlled by the solar wind magnetic field through the process of magnetic reconnection. When regions with differently directed magnetic fields come in contact, it is possible for magnetic field lines to break and reconnect. *Dungey* [1963] first sketched the topology of the magnetosphere for northward and southward IMF. Figure (2.1) (from *Dungey* [1963]) shows schematic plots of the magnetospheric topology for northward and southward IMF. For steady northward IMF, magnetic reconnection occurs in the cusp region, where oppositely directed field lines of solar wind and terrestrial origin intersect. While for steady southward IMF, magnetic reconnection occurs on the dayside magnetopause, turning closed field into open field lines (that is one end connected to the Earth and the other in the solar wind). The reconnected, open field lines take part in the antisunward motion of the solar wind and get dragged to the nightside where the tail lobe field is enhanced. To maintain a steady state, reconnection must occur on the nightside that feeds magnetic flux back to the dayside through magnetospheric convection. Geomagnetic substorms

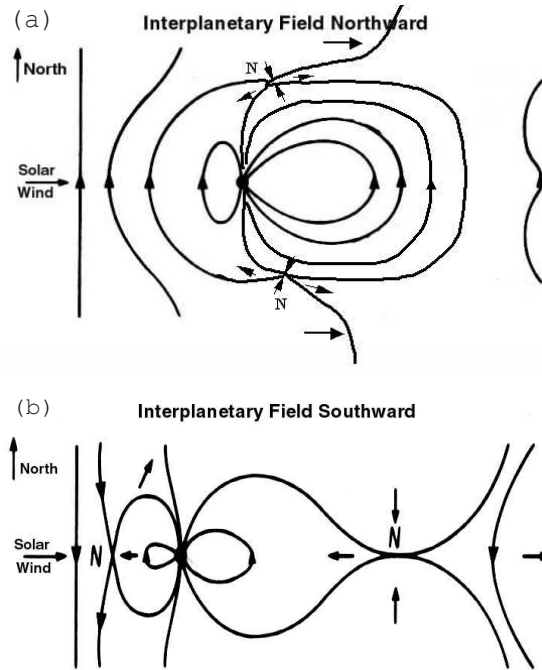


Figure 2.1: Topology of the magnetosphere in north-south plane for northward and southward interplanetary field, according to *J. W. Dungey* in the early 1960s. In the steady state, the plasma flows as indicated by the short arrows. Symbol “N” refers to the neutral point of the magnetic reconnection. (a) With northward IMF. (b) With southward IMF. (From *Dungey* [1963])

occur when the magnetospheric convection is enhanced, generally by a strong continuous southward IMF. The magnetospheric substorms continue to be one of the most actively studied phenomenon in space physics.

2.1 Magnetospheric Dynamics during Substorms

The magnetospheric substorm is a dynamic reconfiguration of the magnetosphere accompanied by strong energy dissipation, that returns the magnetosphere from a high to a low energy state. Observations show that the kinetic energy flux

of the solar wind impinging on the dayside magnetopause with its cross-section of about $30 R_E$ (Earth radii) is about 10^4 GW for typical solar wind conditions. During a typical substorm event, about 10^{15} joule of energy is deposited into the ionosphere on a 30 minutes timescale [*Kamide and Baumjohann, 1993*].

The substorm is a global phenomenon whose manifestation can be observed in nearly all regions of the magnetosphere and ionosphere, as it involves a large number of processes occurring in a wide variety of spatial and temporal scales. They are the most pronounced manifestations of the storage and release processes and have typical time scales of a few hours, with well-defined phases, viz. growth, expansion and recovery phases. In the growth phase, energy from the solar wind is stored in the magnetosphere, resulting in a stressed tail-like configuration. This phase is typically associated with southward turning of the IMF which causes the magnetic reconnection at the day side magnetopause. The reconnection of an originally closed magnetic field line with IMF leads to a transfer of energy and momentum from the solar wind to the magnetosphere. The free end of the open lines are convected to the nightside and are reconnected at $50 - 80R_E$. These reconnected field lines are then convected back towards the inner-magnetosphere. The motion of magnetic field lines across the polar cap leads to the formation of regular two cell convection pattern in the polar ionosphere. This process lasts several tens of minutes to an hour before substorm onset. During the expansion phase of a substorm, the stored magnetic energy in the tail is released. The substorm onset can be due to reconnection of stressed field lines, a northward turning of the IMF or an increase of solar wind dynamic pressure. During the expansion phase, observations show

an earthward bulk flow and particle injection towards the auroral zones along the field lines. In the same time, the plasma beyond the reconnection region is ejected downstream. In the ionosphere, at the expansion phase onset, the equatorward discrete auroral arc brightens. A westward traveling surge and auroral bulge are also formed. The growth of ionospheric currents is initially localized in a longitude sector centered around the midnight at high latitude, and leads to a rapid increase in westward electrojet current. After the release of energy, the system slowly returns to ‘normal’ during the recovery phase. The main observational features [*Kamide and Baumjohann, 1993; Lui, 1990; Kivelson and Russell, 1995; Wiltberger, 1998*], are summarized in Table 2.1.

2.2 Global and Multi-scale Phenomena of the Magnetosphere

The terrestrial magnetosphere is driven by the solar wind and exhibits complex dynamical features. It is prototypical of large-scale open systems and its dynamics is essentially determined by the interactions between its different components or regions, and the characteristics of its driver, the solar wind. Underlying cause of the complex dynamics of the magnetosphere is the inherent nonlinearity of the magnetospheric plasma and the turbulent nature of the solar wind. Furthermore, the magnetosphere is far from equilibrium, especially during geomagnetically active periods, mainly due to the solar wind variability.

Substorms exhibit multi-scale behavior, viz. they have broad band power spectra in a wide range of spatial and temporal scales. The multiscale behavior of

Table 2.1: Key observed features of the solar wind, ionosphere and different regions of magnetosphere during substorms

Regions	Growth Phase	Expansion Phase	Recovery Phase
Solar Wind	Southward turning of IMF	Substorm expansion onset triggered externally by changes in the IMF/solar wind characteristics.	Leakage of magnetospheric particle upstream.
Ionosphere	Enlargement of polar cap size; two convection cell; ionospheric electrojets enhancements; Quiet auroral arcs drift equatorwards.	Aurora brightens and expands in nightside; a westward travelling surge (WTS); magnetic bays; Substorm electrojet; Pi2 and PiB pulsations.	Double oval structure forms, and eastward propagating omega bands are seen on the equatorward one.
Near-Earth	Tail lobe field strength increases; Cross-tail current increases; stretched field lines form; Thin current sheet; tailward of the dipole-like field lines	Earthward high speed plasma flows; Decrease in tail cross-section; Injections of accelerated (tens of keV) particles. dipolarization spread in local time.	Magnetosphere returns into the pre-substorm state.
Mid-tail		Lobe field reduction; Plasma sheet thinning.	Plasma sheet recovers.

the magnetosphere has been recognized in many different ways. The power law dependence of the AE index provided a quantitative measurements of the multiscale behavior [Tsurutani *et al.*, 1990]. The studies of power law nature of the magnetospheric response AE index using structure function show multiscale behavior features [Takalo *et al.*, 1992]. During the global auroral energy deposition events, the studies of the UVI images show that auroral images of the internal scales of the magnetosphere were found to have similar power laws in both quiet and active pe-

riods. However, during active periods, the global energy dissipation had a different scale. These features were interpreted as consistent with an avalanching system [Lui *et al.*, 2000].

The coexistence of global coherence and multiscale behavior is a key feature of the magnetosphere [Sitnov *et al.*, 2000]. The global coherence can be viewed as a first order phase transition, and the multiscale behavior as arising from a second order phase transition with the accompanying scale invariance [Sitnov *et al.*, 2000, 2001; Sharma, 2001; Ukhorskiy, *et al.*, 2002; Shao *et al.*, 2003].

The phase transition-like behavior of the magnetosphere during substorms was derived from the correlated input-output data of the solar wind - magnetosphere system, the solar wind input being the induced electric field VB_S , and the magnetospheric response, the auroral electrojet index AL [Bargatze *et al.*, 1985; Sharma *et al.* 2000; Sitnov *et al.* 2000, 2001]. The magnetospheric dynamics was reconstructed from this data using the singular spectrum analysis (SSA) [Broomhead and King, 1986]. This technique uses the embedding of the original time series into a multi-dimensional space by using the time delay embedding and then sorting the linear combinations of the delayed time series to provide a suitable approximation of the dynamics [details see Chap.3]. The phase space reconstructed from the three leading eigenvectors reveals the regular component of magnetospheric dynamics. The SSA spectrum of the database during substorm time shows clear power-law dependence, as shown in Figure 2.2(a).

After the analysis of the observational data using the singular spectrum analysis, similar time series produced using the AL index generated by global MHD

simulations were studied. The same characteristics showing global and multiscale features [Shao *et al.*, 2003] were obtained and are shown in Figure 2.2(b). Figure 2.2(a) indicates that the singular spectrum of the observed- AL index data obeys power law with an exponent of around -1. Also Figure 2.2(b) indicates that the singular spectrum of the pseudo- AL index data, computed from the global MHD simulation [Shao *et al.*, 2003] obeys power law with an exponent of around -1.5. Thus both the observed and pseudo- AL index show multi-scale behavior, although the latter is cleaner than the former. This is because the global MHD model works well on large scales and low frequency regions and smoothes local and high frequency fluctuations. It is clear from this comparison that both actual and simulated $VB_S - AL$ data show multiscale feature.

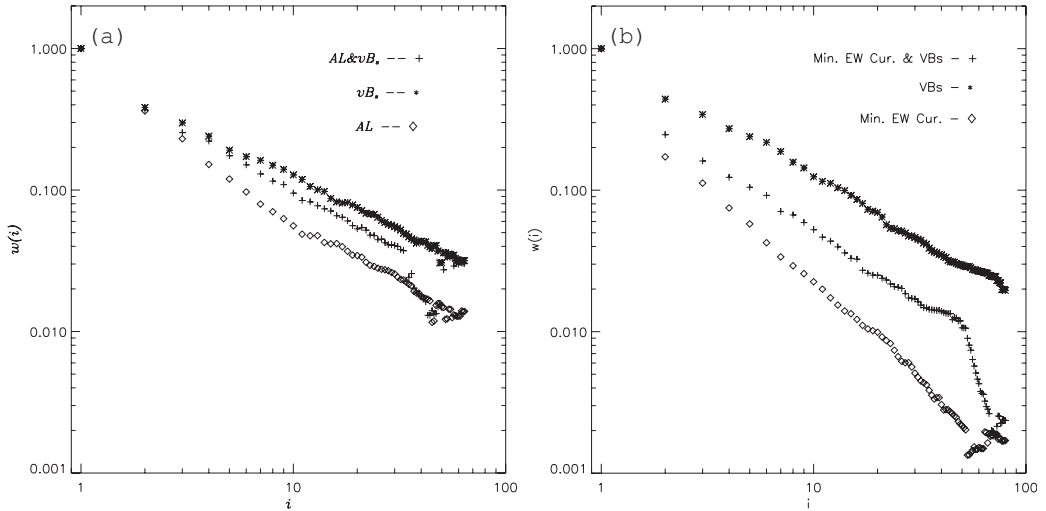


Figure 2.2: Log-Log Plots of SSA eigenvalues for observed- AL or pseudo- AL index and VB_S parameters alone as well as for the combined data. (a) Singular spectrum of $AL - VB_S$ data inferred from *Bargatze et al.* [1985] data (first 20 intervals) (from [Sitnov *et al.*, 2000]) (b) the coupled vB_S -pseudo- AL index system derived from global MHD model. (from [Shao *et al.*, 2003]).

The three principal components in the SSA analysis [*Sitnov et al.*, 2000; *Shao et al.*, 2003] have been used to represent the dynamics of substorms. By projecting the original trajectory matrix along these eigenvectors, a time series data of the dynamical evolution is obtained. The eigenvectors are rotated to minimize or maximize the output and input components in each, and the first three eigenvectors are shown in Figure 2.3. These three eigenvectors are P_o , P_i and P_3 , which are closely related to time averaged value of input (VB_S), output (AL) and the time derivative of the input, respectively. The magnetospheric dynamics represented by these three variables computed from the actual and simulated data are shown in Figure 2.4(a) and (b), respectively. In this figure, the component P_o is color coded and the circulation flows given by dP_3/dt and dP_o/dt are represented by the arrows. Both the 3D surface plots exhibit a two level structure. These figures represent the substorms as transition from a high (red/orange) level to a low (green/blue) level, and thus exhibit a phase transition-like behavior of substorms. Also from these two plots, the substorm cycle patterns are clear, with the arrows showing the trajectory of the substorm evolution. On the average, the dynamical manifolds obtained from the SSA of the actual and simulated AL with the same solar wind conditions are similar. Both plots show that the evolution of the magnetosphere on the largest scale is quite regular and resembles the temperature-pressure-density diagram of equilibrium phase transitions in a two phase system, .e g., the water-steam system.

Sitnov et al. [2001] suggested that the scale free properties of the data can be attributed to the dynamics in the vicinity of a critical point and associated with second-order phase transitions. The magnitude of the largest fluctuations of AL time

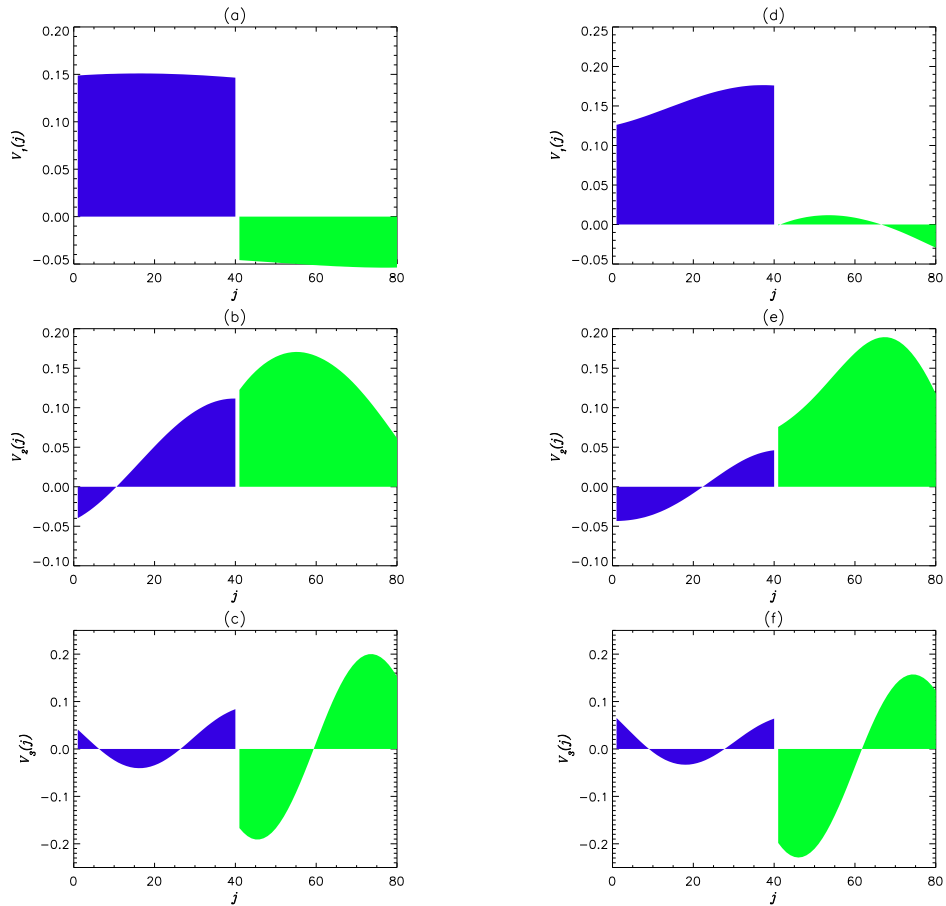


Figure 2.3: (a)-(c) are the original three leading eigenvectors obtained from the singular spectrum analysis (SSA). (a)The first eigenvector; (b)The second eigenvector; (c)The third eigenvector. (d)-(f) are the three leading eigenvectors after the eigenvectors in (a)-(c) are rotated. Each eigenvector is composed of output and input components. The output component is blue-shaded and the input component is green-shaded (*Shao et al., 2003*).

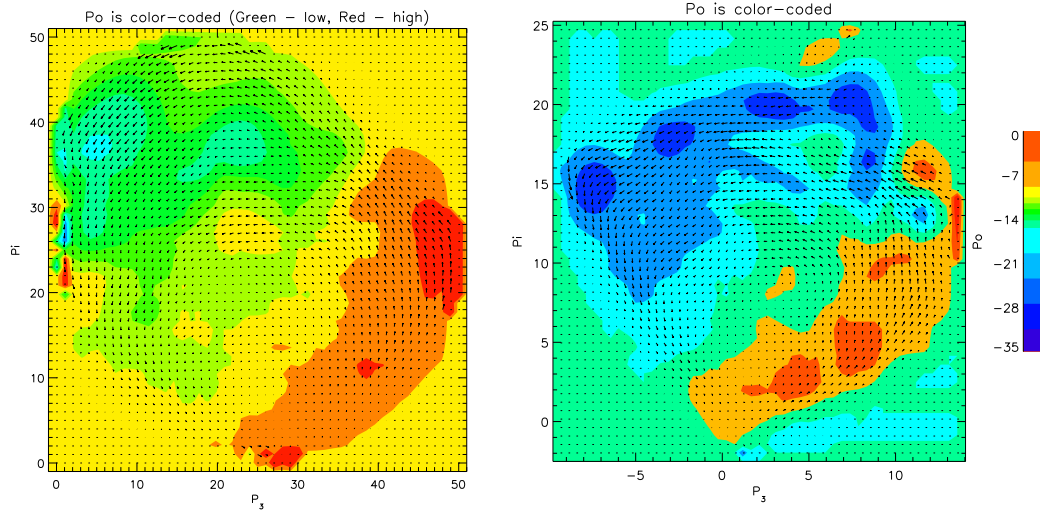


Figure 2.4: The 2D surface approximation of the manifold representing magnetospheric dynamics on the basis plane (P_3, P_i) . The principle component P_o is color-coded. The circular flows given by dP_i/dt and dP_o/dt are represented by arrows. The phase transition map (Left) is from actual observed AL data (*Sitnov et al., 2000*); (Right) is from the pseudo-AL index derived from global MHD mode (*Shao et al., 2003*).

derivative has a power-law dependence on the average value of VB_S , as shown in Figure 2.5. This scenario of substorms is similar to a model in which the dynamical manifold has a cusp catastrophe [*Lewis, 1991*], shown in Figure 2.6. The evolution of an isolated substorms is indicated by dashed arrows.

2.3 Summary

The global and multi-scale aspects of the magnetosphere have been recognized and studied separately. The data derived and global MHD models provide integrated models of these inherent properties of solar wind – magnetosphere coupling. The good agreement between these models show that the global and multi-scale

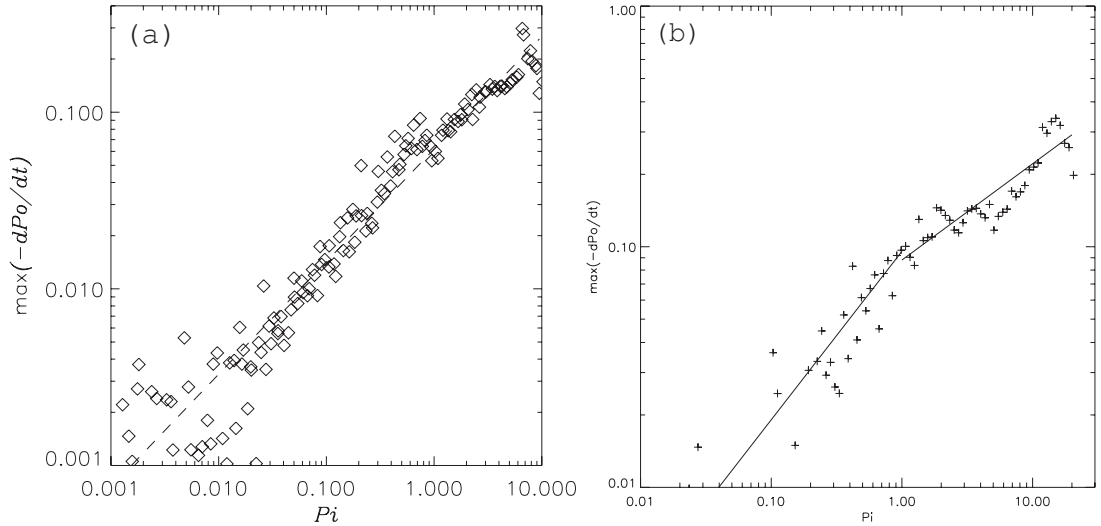


Figure 2.5: An analogue of the input-output critical exponent inferred from *Bargatze et al.* [1985] data (first 20 intervals) (left) and from the data of global MHD simulation (right).

features are inherent in the magnetospheric dynamics. The coherent behavior of the magnetosphere is evident in large scale phenomena like the formation of plasmoids, the recovery of the field line and the formation of global current systems. The multi-scale features are manifested in the small scale phenomena like MHD turbulence, and current disruption during substorms.

Most contemporary approaches to the data derived modeling of the magnetospheric substorm do not account for the existence of global and multi-scale phenomena and thus do not provide a complete description of the observed time series. The low dimensional dynamical models effectively extract the time series constituent generated by the large-scale coherent behavior, but are unable to predict the high dimensional multi-scale features. Also the avalanche and turbulence models can reproduce a variety of the scale free power spectra for multi-scale portion of the

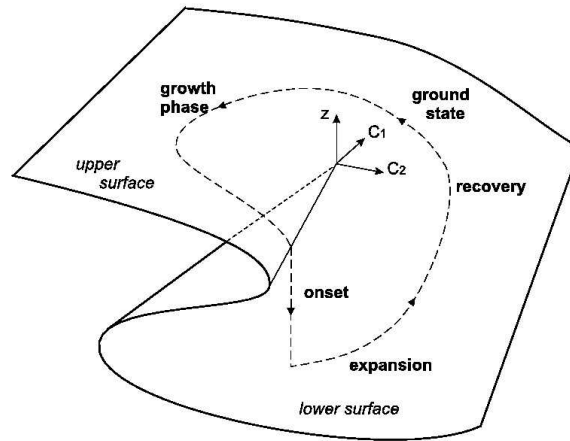


Figure 2.6: Hypothetical cusp catastrophe manifold that was expected to approximate the substorm dynamics of the magnetosphere according to the model of *Lewis* [1991]. The evolution of an isolated substorms is shown by dashed arrows. (*Sitnov et al., 2000*)

observed time series, but can not relate them to the global features of the magnetospheric dynamics and the variations in the solar wind input. The global and multi-scale constituents of the solar wind-magnetosphere coupling co-exist and are critical in the understanding the magnetosphere dynamics.

Chapter 3

Nonlinear Dynamical Techniques for Driven Systems

The solar wind-magnetosphere coupling is an input-output system and the techniques of nonlinear dynamical system theory have been used to model and forecast its dynamics. Earlier, the linear filter techniques have been used extensively to model input-output systems and have provided the linear response characteristics. However these techniques are not sufficient for describing the magnetospheric response to the solar wind. Among the nonlinear dynamical techniques, time delay embedding and phase space reconstruction play a key role in data derived modeling, and led to time series forecasting techniques based on local-linear filters. The local linear filter techniques have been used to study the global and multi-scale features of the magnetospheric dynamics by using the input-output phase space reconstructed from the time series data of VB_G as the input and AL index as the output. These techniques and their applications to the solar wind-magnetosphere coupling are briefly reviewed in this chapter.

3.1 Linear Prediction Filter

A major problem in solar-terrestrial physics is the understanding of how solar wind mass, momentum and energy couple into and subsequently flow through the magnetosphere. There are two models which have been used widely: direct driven

model and loading-unloading model. In both the models, the energy transfer or coupling process is initiated by enhanced magnetic energy input in the magnetosphere due to solar wind variability. The magnetosphere is essentially a non-autonomous system because its dynamics is continuously driven by the solar wind.

One of the earliest methods used to analyze the solar wind-magnetosphere coupling is linear prediction filters [Bargatze *et al.*, 1985; Clauer, 1986]. This method uses a filter to model the linear relationship between measured magnetospheric and solar wind quantities. A linear relationship between the solar wind input time series $I(t)$ and the geomagnetic activity output time series $O(t)$ driven by the solar wind is assumed so that

$$O(t) = \int_0^{\infty} f(\tau)I(t - \tau)d\tau \quad (3.1)$$

where $f(\tau)$ is the linear prediction filter. This filter is calculated only based on the previous inputs and not on previous outputs, which means there is no feedback in the system. Clauer *et al.* [1981] used the solar wind input VB_S , V^2B_S and the solar wind coupling function ε along with the linear filtering routines to model the response of the AL and AU indices to solar wind variation. The solar wind coupling function $\varepsilon = VB^2l_0^2 \sin^4(\theta/2)$ is identified as the dynamo power delivered from the solar wind to the open magnetosphere [Akasofu, 1979]. Clauer *et al.* [1981] suggested that the response of the magnetosphere is not completely linear because the properties of the filter vary with the magnitude of the geomagnetic activity.

Bargatze *et al.* [1985] compiled a large database of simultaneously measured

time series data of the solar wind induced electric field VB_S and the auroral electrojet index AL . This database has been used widely in many studies. The solar wind data is from IMP8 satellite and the period spans from November, 1973 to December 1974. The whole database consists 34 isolated intervals, which contain 42,216 points with 2.5 min resolution. These data intervals are selected as isolated intervals preceded and followed by at least 2-hour segments of quiet solar wind input and AL index values and are arranged in the order of increasing geomagnetic activity. A stack plot of the linear prediction filters obtained from dataset, arranged in order of increasing geomagnetic activity level from bottom to top, is shown in Figure 3.1.

The filters 1-18 have two response pulses near 20 min and 60 min. The filters 19-30 have only a response pulse which reach an amplitude peak near 20 min and decay thereafter. The geomagnetic activity corresponding to the filters 19-30 is stronger than that corresponding to the filters 1-18. Thus the filter peak at a time lag near 20 min for intervals of strong geomagnetic activity is interpreted as the time scale of the dynamic response of the magnetosphere and is associated with direct dissipation. It corresponds to electrojet activity related to direct interaction between the solar wind and the magnetosphere. The 60 min time lag of the other peak for intervals of moderate activity corresponds to the loading of energy in the magnetotail and its energy release at expansion phase onset. The absence of the second peak at the 60 minute time lag at the highest levels of the activity motivated an analogue model based on a dripping faucet [Baker *et al.*, 1990]. In this model, the loading-unloading cycle of the magnetosphere was considered to be chaotic when the loading rate is increased beyond a threshold value. It was concluded that the

response of the magnetosphere to VB_S , represented by AL index, is not completely linear.

These studies have motivated many studies of the nature of the solar wind-magnetosphere coupling. For example, *Vassiliadis and Klimas* [1995] compared the moving average filter with LRC-circuit filters, which were derived from the solar wind-magnetosphere coupling linear model. It was suggested that the discrepancy between the details in filter structure is due to intrinsic nonlinearity of the system, and the assumption of system linearity is almost certainly invalid. However, linear analysis alone is not sufficient to describe this complex behavior. The tools of nonlinear dynamics and deterministic dynamical theory are expected to yield a new insight into the behavior of the magnetosphere during geomagnetic storms and substorms.

3.2 Nonlinear Dynamical Studies Using Time Series Data

The multi-scale nature of the magnetosphere has been recognized mainly by the power law dependence of many observed variables [*Tsurutani et al.*, 1990, *Lui et al.*, 2000; *Sitnov et al.*, 2003]. Recent studies using time series data have shown that the magnetosphere is inherently multiscale, and the solar wind - magnetosphere coupling can be treated as a nonlinear dynamical system. The recent developments in the theory of nonlinear dynamical systems have led to new techniques based on the characterization of the intrinsic phase space structure using time series data. In this section, we review these nonlinear dynamical approaches, in particular the

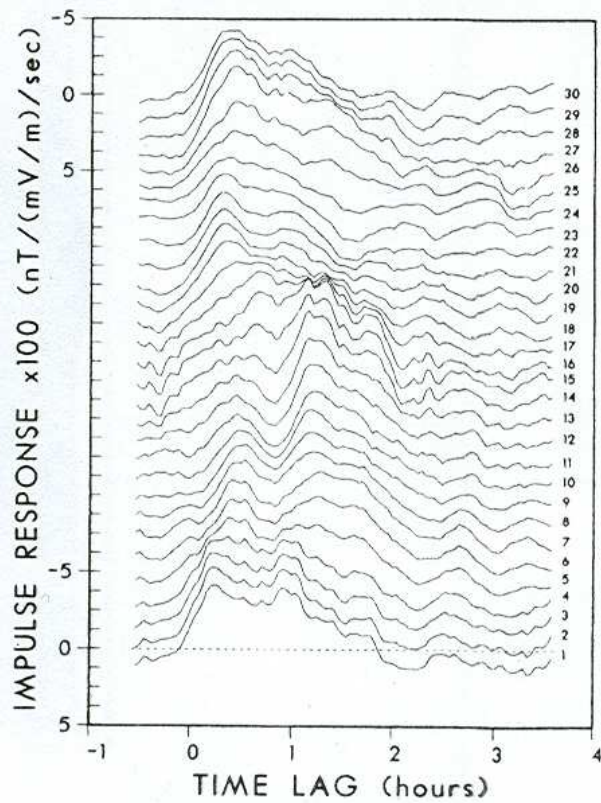


Figure 3.1: A stock plot of linear prediction filter for all levels of geomagnetic activity. The impulse response functions relating the input VB_S with the output AL index [from *Bargatze et al., 1985*]

techniques of phase space reconstruction.

Dynamical systems are mathematical objects used to model physical phenomena whose state changes over time. The evolution rule of the dynamical system is a fixed rule that describes what future states follow from the current state. The rule is deterministic: for a given time interval only one future state follows from the current state, e.g., as a map:

$$\mathbf{y}_{t+1} = f(\mathbf{y}_t) \tag{3.2}$$

where each vector \mathbf{y}_t represents a state of the systems in N -dimension phase space, f is a nonlinear operator acting on all points. At any given time, the solution of the map can be written as a flow of known points in the phase space. In the case of a dissipative system, the flow eventually contract to a set of few degrees of freedom which is called an attractor. The nonlinear systems with a few degrees of freedom can create output signals that look complex and mimic stochastic signals from the point of view of conventional time series analysis. The reason for this is that trajectories with nearly identical initial conditions will separate from one another at an exponentially fast rate, leading to chaos. The key difference is that the short-term prediction is not ruled out for a chaotic system if there are a reasonably low number of active degrees of freedom. For this purpose, however, the state of the system has to be specified in terms of the complete set of its components in the phase space. At the same time, it is common that only a limited number of variables can be measured in experiments. It turns out that the complete set of dynamical variables can still be reconstructed using the delay embedding technique.

An embedding is a smooth map, say Φ , from the manifold S to a space \mathcal{R} such that its image $\Phi(S) \subset \mathcal{R}$ is a smooth submanifold of S . So the embedding Φ , a diffeomorphism between S and $\Phi(S)$, is a smooth invertible function with smooth inverse. The space which contains the image will be called the embedding space and its dimension the embedding dimension.

Before applying the nonlinear techniques on the solar wind - magnetosphere coupling system, we study a specific time series data generated from the well known Lorenz attractor[Lorenz, 1963].

$$\begin{aligned}\frac{dx(t)}{dt} &= \sigma(y(t) - x(t)), \\ \frac{dy(t)}{dt} &= -x(t)z(t) + rx(t) - y(t), \\ \frac{dz(t)}{dt} &= x(t)y(t) - bz(t).\end{aligned}\tag{3.3}$$

These equations are derived from a finite mode truncation of the partial differential equations describing the thermal driving of convection in the lower atmosphere. The time series $x(t)$ which results from solving the Lorenz equations using a fourth-order Runge-Kutta integrator using time step $dT = 0.009$ is shown in Figure 3.2. When the parameter values $r = 28, b = 8/3$ and $\sigma = 10.0$ are selected, the system produces chaotic dynamics. The trajectory of the three degrees of freedom system $[x(t), y(t), z(t)]$ in a three dimensional space is shown as Figure 3.3. The characteristic structure of the long term orbit of the Lorenz system, the Lorenz attractor, is apparent. The time evolution is organized by the two unstable foci and intervening saddle point.

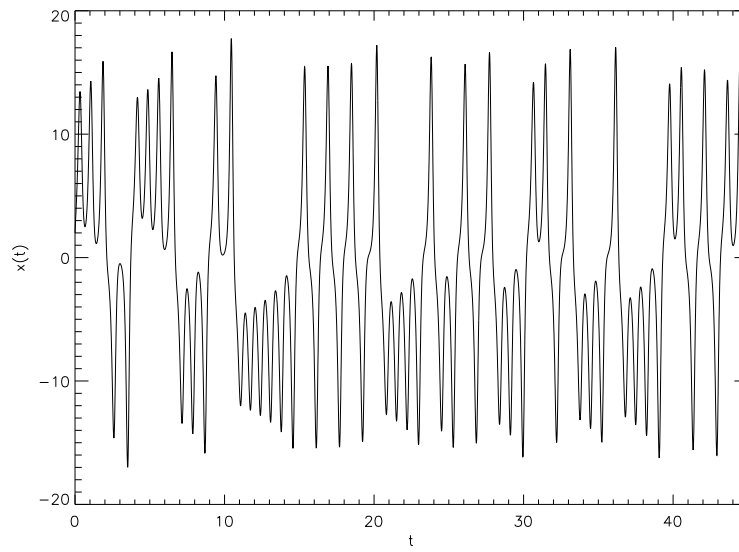


Figure 3.2: A sample of the time series $x(t)$ corresponding to motion on the attractor of the full Lorenz model.

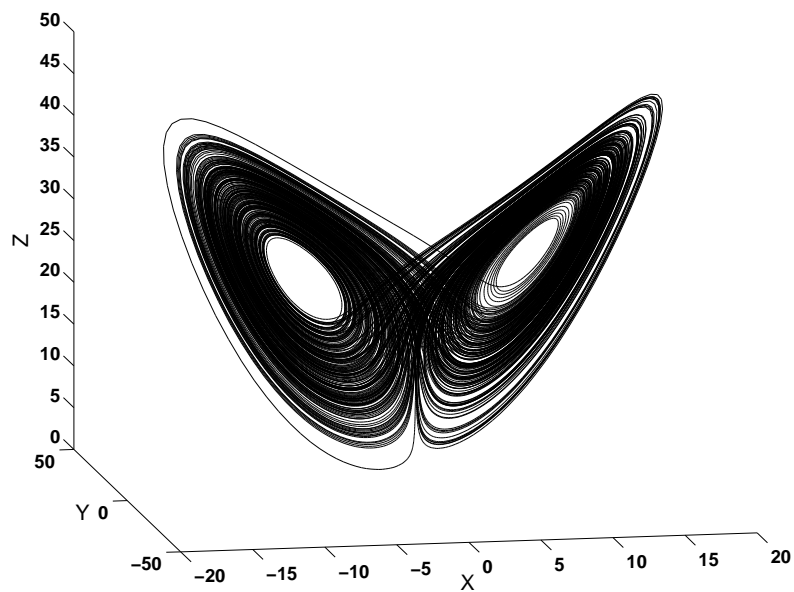


Figure 3.3: The attractor of the full Lorenz model ($\sigma = 10, b = 8/3, r = 28$) in three-dimension phase space.

A chaotic nonlinear system can be modeled by a few nonlinearly coupled ordinary differential equations. This remarkable property arises from the inherent characteristic of a dissipative nonlinear system, viz. its phase space volume contracts as the system approaches its asymptotic state. This dynamical state may generally be described by fewer variables than the original system. The attractor is characterized by its dimension, which is the lower bound to the number of independent variables necessary to describe the attractor.

One of the hallmarks of chaotic behavior is the sensitivity of any orbit to small changes in initial condition or small perturbations anywhere along the orbit. Because of this sensitivity, it is inappropriate to compare two orbits of a nonlinear system directly with each other. However, the attractor is the same which each orbit visits during its evolution. These are independent of initial conditions and provide a direct analogy to the Fourier frequencies of a linear dynamical system. System identification in nonlinear chaotic systems means establishing a set of invariants for each system of interest and then comparing observations to that library of invariants. In nonlinear dissipative systems the dimension has fractional values and is called a fractal. This property is indicative of chaotic dynamics governing the motion on the attractor.

If the system variables are sufficiently nonlinearly coupled, the details of the characteristic quantities of the phase space can be computed from one or few variables [Packard *et al.*, 1980, Takens, *et al.*, 1980; Ruelle, 1989]. The time delay embedding technique is an appropriate approach for using time series data to reconstruct the phase space and obtain the system's characteristic quantities. We construct a

m -component phase vector X_i from a time series $x(t)$ as:

$$X_i = \{x_1(t_i), x_2(t_i), \dots, x_m(t_i)\}. \quad (3.4)$$

where $x_m(t_i) = x(t_i + (m - 1)T)$ and T is a proper time delay.

The time lag T and the dimension of the space m in the time-lagged vectors X_i need to be specified in Equation 3.4. If the dimension m is larger than the attractor dimension $2m_A$, which can be fractional, then the attractor as seen in the space with lagged coordinates will be smoothly related to the attractor as viewed in the original physical coordinates, which we do not know. In practice, if we choose m large enough, physical properties of the attractor that we wish to extract from the measurements will be the same when computed on the representative in lagged coordinates and when computed in the physical coordinates. The procedure of choosing sufficiently large m is known as embedding, and the dimension that work is called an embedding dimension m_E . Time-delay embedding is the only systematic method for going from scalar data to multidimensional phase space [*Abarbanel et al.*, 1993].

3.3 Time Delay and Embedding Dimension

The time delay T and embedding dimension m are two key parameters in phase space reconstruction. Several methods are used to estimate these two key parameters, such as mutual information, correlation integral, singular value decomposition, etc. In the following these methods and applications to the Lorenz Attractor and

the real time series observation data of AE index are discussed.

3.3.1 Mutual Information Function

Consider two random systems variables, X_1 and X_2 , with possible outcomes i_1 and i_2 from the measurements of the systems. There is a probability distribution associated with each system governing the possible outcomes of observations on them. The average mutual information between measurements of i_1 and i_2 is defined as [*Cover and Thomas, 1991*]:

$$I(X_1, X_2) = \sum_{i_1} \sum_{i_2} \varphi_{12}(i_1, i_2) \log_2 \left[\frac{\varphi_{12}(i_1, i_2)}{\varphi_1(i_1)\varphi_2(i_2)} \right] \quad (3.5)$$

where $\varphi_1(i_1)$ and $\varphi_2(i_2)$ are the probability distributions of random variables X_1 and X_2 assuming states i_1 and i_2 , respectively, and $\varphi_{12}(i_1, i_2)$ is their joint distribution. The average mutual information is a generalization to the nonlinear world from the linear correlation function. When the measurements of systems X_1 and X_2 are completely independent, $\varphi_{12}(i_1, i_2) = \varphi_1(i_1)\varphi_2(i_2)$, and $I(X_1, X_2) = 0$. To place this abstract definition into the context of observations from a physical system $x(n)$, The average mutual information between observations at n and $n+T$ is [*Gallager, 1968*]:

$$I(T) = \sum_{n=1}^N p(x(n), x(n+T)) \log_2 \left| \frac{p(x(n), x(n+T))}{p(x(n))p(x(n+T))} \right|. \quad (3.6)$$

The proper time delay T depends on the property of $I(T)$. If T is too small, the measurements $x(n)$ and $x(n+T)$ tell us so much about one another that we need not make both measurements. If T is too large, then $I(T)$ will approach zero, and

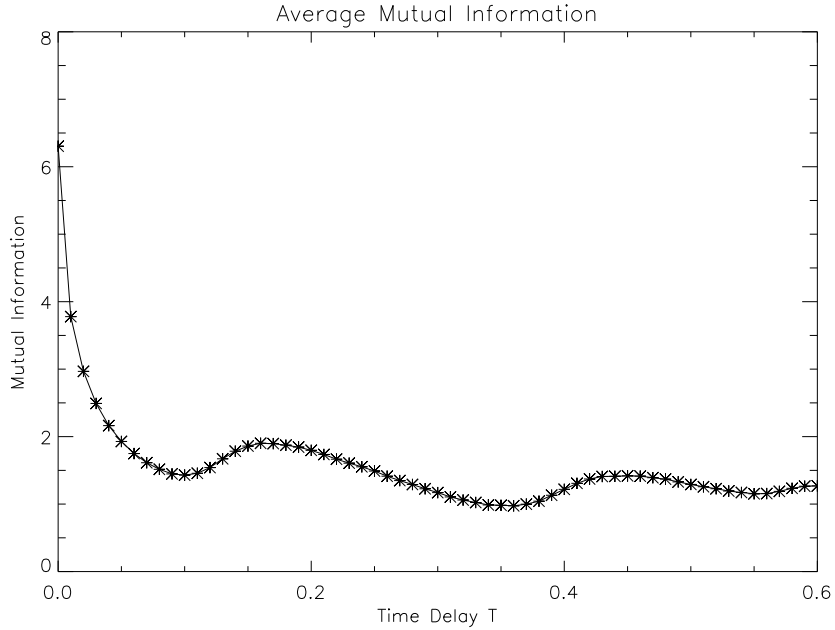


Figure 3.4: Average mutual information $I(T)$ as a function of time lag T for the Lorenz data.

nothing connects $x(n)$ and $x(n+T)$, so this is not useful. *Fraser* and *Swinney* [1986] suggest that we choose that T_m where the first minimum of $I(T)$ occurs as a useful selection of time lag T . This minimum can be used as a time lag for phase space reconstruction. The mutual information of the Lorenz attractor is shown in Figure 3.4. The first minimum of the mutual information is around 0.1, about 10 times of the integration time step $\Delta t = 0.009$, and this value can be used as a proper time delay in the phase space reconstruction.

In order to estimate the time delay for the reconstruction of the magnetospheric dynamics, we use the time series data of 1-min averaged time series AE index for January 1983 (Figure 3.5). The average mutual information $I(T)$ in this case is shown in Figure 3.6. There is no apparent minimum value at some specific time lag

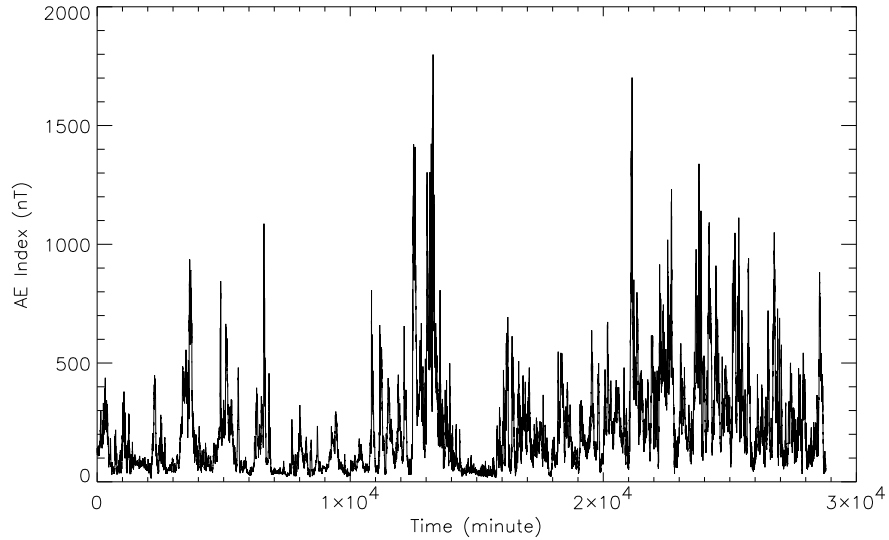


Figure 3.5: Time series data of the auroral electrojet index AE on January 1983 with 1 minute resolution

T and this does not mean that $I(T)$ loses its role as a good standard for selection of T , but only the first minimum criterion need to be replaced, e. g., $(T)/I(0) \approx 1/5$ [Abarbanel *et al.*, 1993]. From Figure 3.6, we estimate $T = 10 - 20$ min as a suitable time delay for this AE time series data.

3.3.2 Correlation Integral

An attractor is characterized by a set of points determined by the evolution of the system variables and the space in which these points are located is determined by its dimension. When the 3D Lorenz attractor (Figure 3.3) is projected onto 1D, e. g., in the x axis (Figure 3.2), we cannot see the structure of this nonlinear system properly. So it is necessary to unfold the system in a larger embedding space in

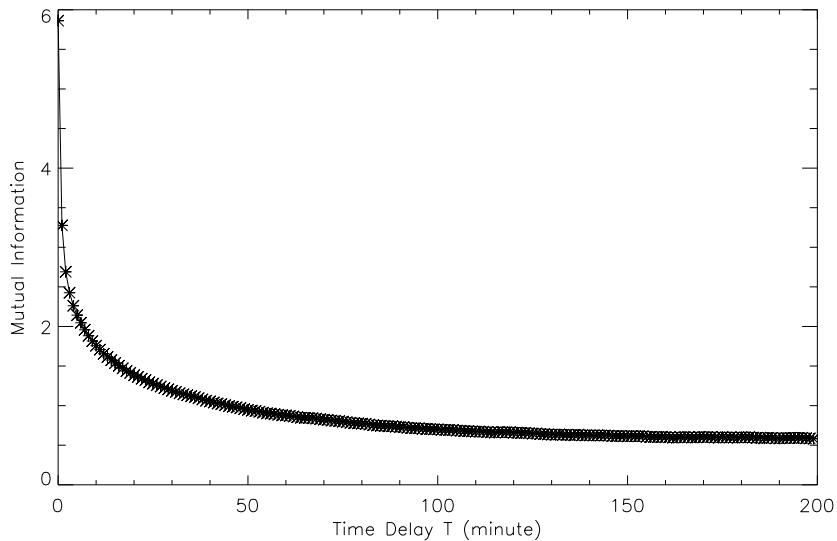


Figure 3.6: Average mutual information $I(T)$ as a function of time lag T for AE index.

order to discern the dynamical structure. Once a time delay has been chosen, the embedding dimension can be obtained from the time series data, e. g., by using the correlation integral.

If an attractor is properly unfolded by choosing a large enough dimension, the properties of this attractor depend on the distance between points in the phase space, and the characteristic quantities should be preserved for higher values of the embedding dimension. Thus increasing the embedding dimension m after its attractor dimension has been reached will not affect on these properties. The correlation integral function is defined for N vectors in an m -dimensional space for the distance r as [*Eckmann and Ruelle 1985*]:

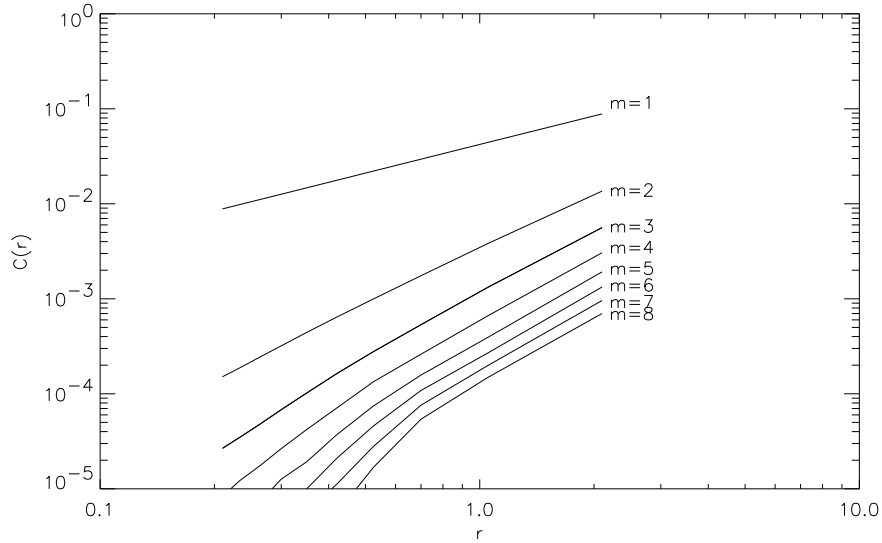


Figure 3.7: Sequence of correlation integrals $C(r)$ for Lorenz data in embedding dimension $m = 1, \dots, 8$

$$C(r, m) = \lim_{N \rightarrow +\infty} \frac{1}{N^2} \sum_{i=1}^N \sum_{j=1}^N \Theta(r - |X_i - X_j|), \quad (3.7)$$

where Θ is the Heavyside function. The correlation dimension is defined as

$$\nu = \lim_{r \rightarrow 0} \frac{\log C(r, m)}{\log r} \quad (3.8)$$

We can evaluate $C(r)$ as a function of m and determine when the slope of its logarithm as a function of $\log(r)$ becomes independent of m . We applied the correlation integral function defined by Equation 3.7 on the Lorenz attractor data set and on the *AE* index data for 1983; the results are shown as log – log plots of $C(r)$ as a function of m in Figures 3.7 and 3.8, respectively. In Figure 3.7, it is clear that for $m \geq 3$, the slope of function $C(r)$ becomes independent of the value of m . Thus we can choose $m = 3$ as a proper embedding dimension for Lorenz attractor.

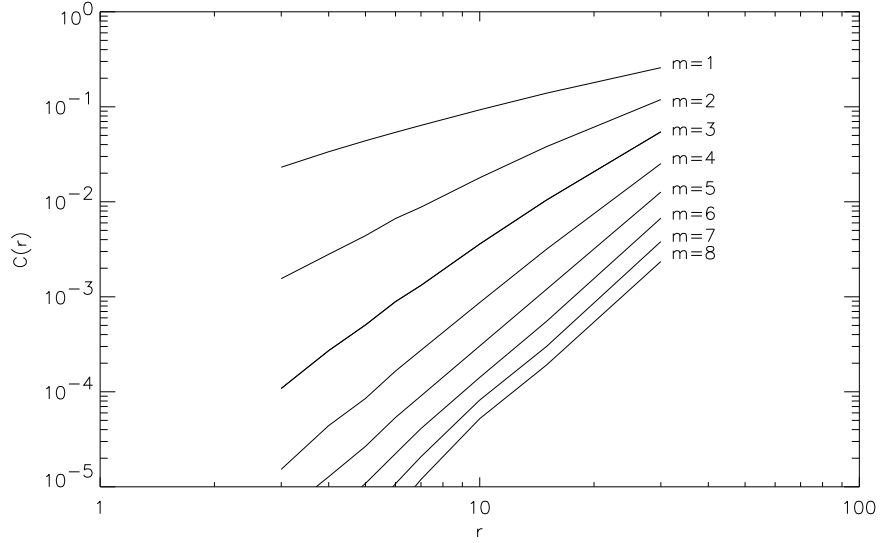


Figure 3.8: Sequence of correlation integrals $C(r)$ for AE index data in embedding dimension $m = 1, \dots, 8$

Also for the function $C(r)$ of the AE index of 1983 in Figure 3.8, when $m \geq 4$, the slope of $C(r)$ are nearly parallel each other and are independent of the value of m . So we can choose $m = 4$ as an approximate embedding dimension in the phase space of auroral electrojet.

If the number of points is large enough, the distribution of $C(r, m)$ will exhibit a power law distribution with a small r as:

$$C(r, m) \sim r^\nu, \quad (3.9)$$

where ν is the correlation dimension, and can be computed from Equation 3.8. In practice, ν is computed as:

$$\nu = \frac{\Delta \log C(r, m)}{\Delta \log r}, \quad (3.10)$$

With the increase of the dimension m , the correlation dimension will converge to a value, and the nearest integer greater than this value is the minimum number of degrees freedom of the system, if an attractor exists. But, in the absence of an attractor, the phase space will be filled, and the computed dimension will correspond to the embedding dimension m . The correlation dimension of the AE index of January 1983 converges to a value between 3-4 [Vassiliadis *et al.*, 1990] when m is large than 10, and thus the magnetosphere behaves as a low dimensional dynamical system.

Although the computation of the correlation dimension from the time series data has limitations [Shan *et al.*, 1991a, 1991b; Robert, 1991], such as the choice of the time delay, the finite data length and the data noise level, similar value were obtained from other datasets. The Bargatze [et al. 1985] dataset, with 40,000 points of 2.5 minute resolution AL index, gives a correlation dimension between 3 and 4 [Vassiliadis *et al.*, 1990; Roberts, et al., 1991]. For the 1-5 April 1983 AE index, 7200 points of 1 minute resolution AE gives a smaller correlation dimension at 2.4 [Shan *et al.*, 1991a]. These studies indicate that the phase space of the magnetospheric activity can be considered as a low dimensional system. However, as Prichard and Price [1992] pointed out the estimate of the dimension of non-stationary time series with long autocorrelation time, such as AE and AL indices, is low. This is because the datasets used to compute the correlation dimension include not only the correlation between the different passes of the trajectory but also those along the trajectory. If the highly correlated parts along the trajectory are dominant in the computation when the length of the sampling time is roughly the same as the

autocorrelation time, the dimension may be spurious. Upon excluding the points within a specified distance from the reference point [*Theiler*, 1986], the convergence to a fixed slope was not obtained for most segments of *AE* and *AL* data, which means the low dimensionality is questionable. However this issue can be resolved, at least in part, by using singular spectrum analysis and it was shown that global magnetospheric dynamics is indeed low dimensional [*Sharma, et al.*, 1993].

3.3.3 Singular Spectrum Analysis

Singular spectrum analysis [*Broomhead and King*, 1986] can estimate the effective variable number needed to describe the system from its spectrum of eigenvalues.

We can construct an m -dimension delay vector matrix:

$$A = N^{-1/2} \begin{bmatrix} x_1(t_1) & x_2(t_1) & \cdots & x_m(t_1) \\ x_1(t_2) & x_2(t_2) & \cdots & x_m(t_2) \\ \vdots & \vdots & \ddots & \vdots \\ x_1(t_N) & x_2(t_N) & \cdots & x_m(t_N) \end{bmatrix} \quad (3.11)$$

where N is the total number of the vectors. This $N \times m$ matrix contains all the dynamical information in the data. If the system is a low dimensional system, there exist a small number of the linearly independent vectors obtained from the singular spectrum analysis. In the absence of noise, the eigenvalues corresponding to these few independent vectors are nonzero, and the rest of the other eigenvalues are zeros. So the number of nonzero eigenvalues is the number of independent vectors, and also the number of the variables required to describe the system. However, the time series data of a real dynamical system are inevitably noisy. This leads to a small

number of significant eigenvalues, while the other eigenvalues define a noise floor. The number of the eigenvalues above the noise floor is an estimate of the number of degrees of freedom. The corresponding eigenvectors define the orthogonal directions in the embedding phase space.

3.4 Phase Space Reconstruction

The singular value decomposition (SVD) approach was applied on the data obtained from the Lorenz model (Equation 3.4), in which time evolution is organized by two unstable foci and an intervening saddle point. The first plot of Figure 3.9 is the time delay reconstruction from a time delay embedding $x(t)$ versus $x(t + \tau)$, where $\tau = 20$. The time series data of the x component of Lorenz attractor, shown in Figure 3.2, can be used to compute the singular spectrum, and obtain its dominant eigenvalues, and then the time series can be projected on the corresponding eigenvectors, which are the principal coordinates in the embedding space. The projected variables (y_1, y_2, y_3) can then be used to describe and reconstruct the dynamics of the original Lorenz attractor.

The three projections on the planes obtained from three orthogonal principal directions are shown in Figure 3.9(b)-(d). It is clear that there is a qualitative relationship between the Lorenz attractor itself and its reconstruction from one of the coupled variables. The dynamical features are seen to be preserved.

In the solar wind-magnetosphere system, the state space reconstructed by time-delay embedding is quite noisy, due in part to the randomness of the solar

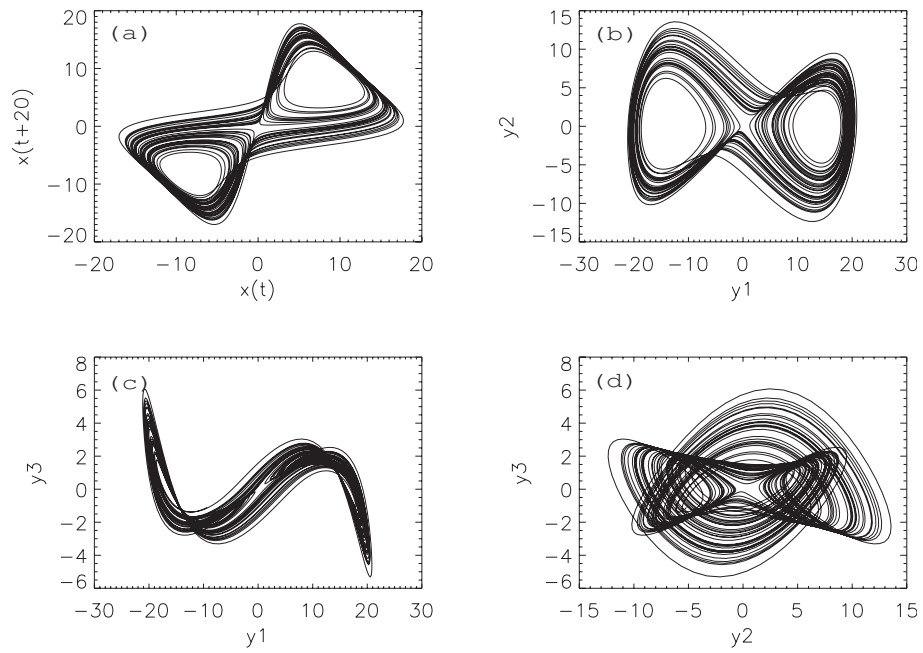


Figure 3.9: Application of singular spectrum analysis on Lorenz attractor (a) the projection of attractor from a time delay embedding $x(t)$ vs. $x(t + \tau)$ with $\tau = 20$. (b)-(d) Plots of variable y_1, y_2, y_3 obtained from projection on three orthogonal principle directions.

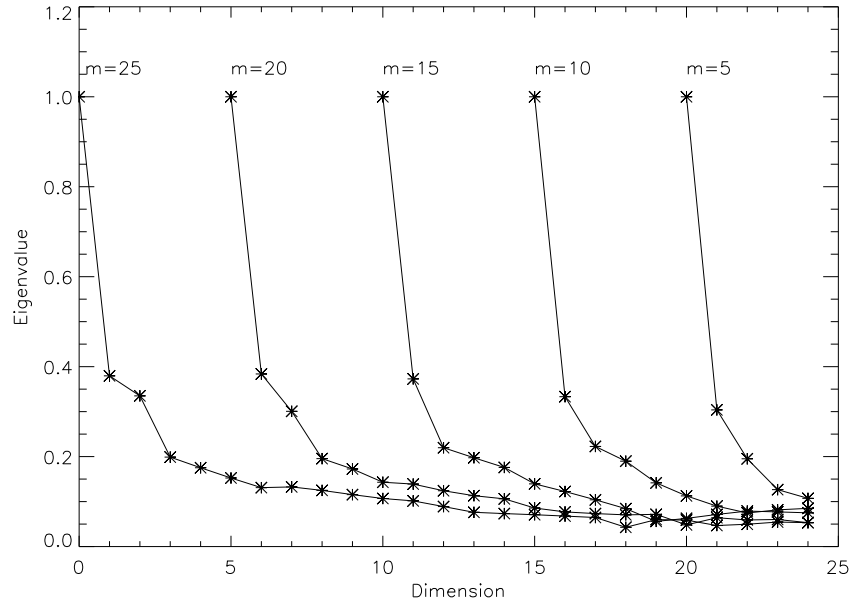


Figure 3.10: The normalized singular spectra computed from the AE index for $T=40$ min and $m = 5, 10, 15, 20, 25$ as labeled.

wind driver. Applying the technique of singular spectrum analysis on the time series measurements of AE index (1983) [Sharma *et al.*, 1993], the three dominant eigenvalues for this nonlinear system are shown in Figure 3.10, where the eigenvalues are normalized to the largest eigenvalue. Each curve corresponds to the different embedding dimension m and $\tau = 40$ min is chosen as the time delay after consideration of the loading-unloading time scales of 20-60 min for substorms. The first three eigenvalues are far away from the near-zero noise floor for all values of m . However, the higher order eigenvalues lie within a “noise floor” with different dimension m . In the m -dimensional embedding space, the eigenvalues yield the relatively strong orthogonal principal directions. So these first three eigenvalues and their corresponding eigenvectors define a three dimension system in the embedding

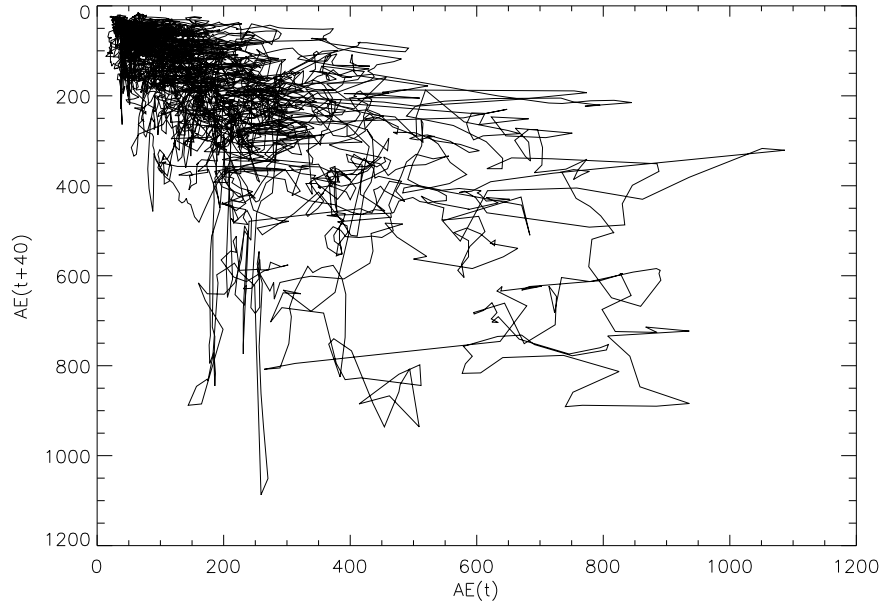


Figure 3.11: The phase space of the magnetospheric activity reconstructed from a time-delay embedding $x(t)$ versus $x(t+T)$, with $T = 40$ min

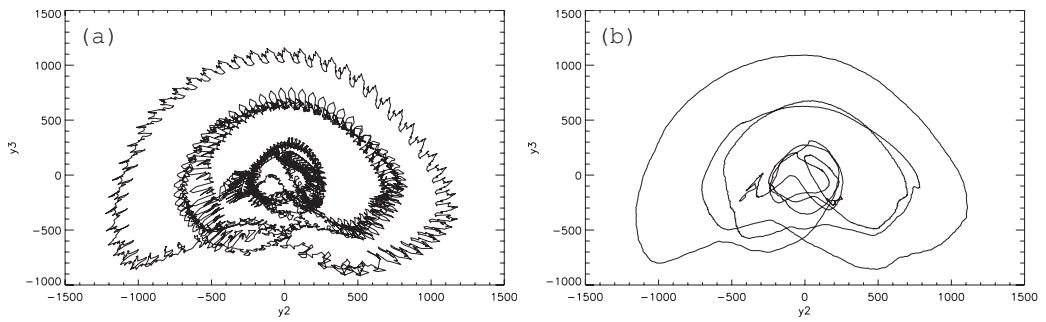


Figure 3.12: The phase space of the magnetospheric activity reconstructed from the AE index. (a) a plot of variables y_2 and y_3 obtained by projections along 2nd, 3rd eigenvector. (b) smoothed by adjacent 19 points

space.

The reconstructed phase space from the embedding technique is shown in Figure 3.11. Also the reconstructed phase space by using singular spectrum analysis to project the trajectory matrix onto the $(y_2 - y_3)$ plane is shown in Figure 3.12. Although both reconstructed phase spaces show clearly the dynamic trajectory patterns, the one based on time-delay embedding shows a high level of random noise along the orbit, while the trajectory pattern from the SVD shows much less noise, indicating that the SVD method can remove noise significantly. Thus the SVD method not only removes the random effect of the turbulent solar wind and reveals the inherent nonlinear dynamic aspect of the system, but also yields a new way to analyze the time series. This cleaner trajectory in Figure 3.12(b) is obtained by a moving average along the trajectory.

3.5 Nonlinear Input-Output Modeling of the Magnetosphere

The driven nature of the magnetosphere is ubiquitous in many input-output models, either linear or nonlinear, of the solar wind (input) driving the geomagnetic activity (output). A dynamical input-output model can be constructed from the time series data of the input $I(t)$ and the output $O(t)$ of the system. As before, it is assumed that if a phase space is large enough to unfold the dynamical attractor, the phase space reconstructed from the time series is appropriate for modeling the evolution of the system. Consequently, the future states can be derived from the known evolution of the similar states.

In an input-output model of the solar wind-magnetosphere system during substorms, the solar wind convective electric field VB_S is commonly used as the input and the geomagnetic activity index AL or AE as the output. Thus the input-output vector in the $2m$ dimensional embedding space can be constructed as

$$X_i = \{I_1(t_i), I_1(t_i), \dots, I_{M_I}(t_i), O_1(t_i), O_1(t_i), \dots, O_{M_O}(t_i)\} \quad (3.12)$$

where $M_I = M_O = m$. The $2m$ -dimensional state vector X_i at $t = t_1, t_2, \dots, t_N$, can now be used to construct a trajectory matrix for the dynamics of the system as:

$$X = N^{-1/2} \begin{bmatrix} I_1(t_1) & I_2(t_1) & \cdots & I_m(t_1) & O_1(t_1) & O_2(t_1) & \cdots & O_m(t_1) \\ I_1(t_2) & I_2(t_2) & \cdots & I_m(t_2) & O_1(t_2) & O_2(t_2) & \cdots & O_m(t_2) \\ \vdots & \vdots & \ddots & \vdots & \vdots & \vdots & \ddots & \vdots \\ I_1(t_N) & I_2(t_N) & \cdots & I_m(t_N) & O_1(t_N) & O_2(t_N) & \cdots & O_m(t_N) \end{bmatrix} \quad (3.13)$$

where N is the number of vectors. This $N \times 2m$ matrix contains all the dynamical features of the system contained in the data and yields its evolution in the reconstructed phase space.

3.5.1 Nonlinear Moving Average Filter

The local linear prediction technique is an extension of the linear prediction filter that allows for nonlinear coupling. The local-linear technique uses only the linear term in an expansion around the initial conditions. It should be noted that the reconstructed phase space captures the nonlinearity of the system and the linearity

used in this technique is only local, thus retaining the nonlinearity in the dynamical behavior. At this point, a linear approximation to the nonlinear curve can be used to predict the next step in the evolution. This approximation is valid only locally in a small range, thus the linear-local fitting must be repeated at each time steps to predict the next step. This implies that the local-linear filter varies along the dynamical trajectory, and thus takes into account the nonlinear features of the system.

The main idea of this method is the use of the trajectories in the neighborhood of the state at time t to predict its location at the next time step. Knowing how the neighboring trajectories evolve, the location of the current state $x(t)$ at next time step $t + T$ can be predicted. As noted above, the procedure is locally linear but is essentially nonlinear as the features of the neighboring trajectories are taken into account by considering a small neighborhood. For a given time series, a proper embedding dimension is obtained when two states x_k and x_n , which are close together in the embedded phase space, yield the next states of O_{k+1} and O_{n+1} which are also close together [Vassiliadis *et al.*, 1995, Valdivia *et al.*, 1996; Ukhorskiy *et al.*, 2002].

The predicted output O_{n+1} can be described as a nonlinear function of the input I_n and current output O_n as

$$O_{n+1} = F(I_n, O_n). \quad (3.14)$$

In this model, the geomagnetic activity is represented by a state vector and the function F governing the evolution of the magnetospheric state O_n depends on both the input and the previous states. A Taylor expansion of F up to the linear

terms gives:

$$\begin{aligned} O_{n+1} &\approx F^{(0)}(I_n^c, O_n^c) + \sum_{i=0}^{M_I-1} A_i \delta I_{i+1,n} + \sum_{j=0}^{M_O-1} B_j \delta O_{j+1,n} \\ &= F^{(0)}(I_n^c, O_n^c) + A \delta I_n + B \delta O_n. \end{aligned}$$

The zero order term $F^{(0)}$ is a function of (I_n^c, O_n^c) , the center of expansion, while δO_n and δI_n are small deviations from the center. All the three parameters $F^{(0)}$, δO_n , δI_n can be obtained from the known data, which is referred to as the training set. Given the current state, the states similar to it in the training set are selected as the first step. The similarity of the current state with any other state in the training set is quantified by the Euclidean distance between them in the embedding space. The states within a specified distance of the current state are referred to as the nearest neighbors (NN).

The average value of the state vectors of the nearest neighbors is usually defined as the center of the expansion, referred as the center of mass, and is used in defining the nonlinear filters for short term and long-term predictions of auroral indices [Ukhorskiy *et al.*, 2002]. Thus

$$O_{n+1} = \langle O_{n+1} \rangle_{NN} + A \delta I_n + B \delta O_n. \quad (3.15)$$

where $\langle O_{n+1} \rangle_{NN} = \frac{1}{NN} \sum_{k=1}^{NN} (\vec{I}_n^k, \vec{O}_n^k)$.

Ukhorskiy *et al.* [2002] pointed out that for a long-term prediction of AL time series, the terms other than the center of mass consist of the higher order terms of the filter for local-linear ARMA filter. These terms cannot be modeled in a

consistent manner and should be ignored in developing a global model. The prediction procedure then reduces to a search of the average response of the system. In this forecasting method the choice of the nearest neighbors (NN) and the embedding dimension ($2m$) are crucial. A large number of neighbors are likely to lead to a smoothing of the variations while a small number may lead to wide variations among the chosen states. The choice of the embedding dimension of the input (output) m is based on the unfolding of the dynamics in the reconstructed phase space. For a state X_n , if the dimension $2m$ and its NN nearest neighbors represent the system properly, the average over NN nearest neighbors defines the smooth manifold of dimension $2m$ on which its dynamics can be predicted. The prediction using the mean field approach [Ukhorskiy *et al.*, 2004] is:

$$O_{n+1} = \frac{1}{NN} \sum_{k=1}^{NN} X_k. \quad (3.16)$$

The local linear ARMA and the local linear mean field filters have been used to model the magnetosphere with the correlated database [Bargatze *et al.*, 1985] of solar wind and geomagnetic activity time series [Ukhorskiy *et al.*, 2002, 2004]. Both these techniques yield good results for small or medium values of the dimension, indicating that the global aspects of the magnetospheric dynamics can be modeled as a low-dimensional system.

The prediction accuracy is quantified by the normalized mean square error (NMSE):

$$\eta = \frac{1}{\sigma_0} \sqrt{\frac{1}{N} \sum_{i=1}^N (O_i - O_i^*)^2}. \quad (3.17)$$

where O_i and O_i^* are the observed and predicted data, respectively, and σ_0 is the standard deviation of O_i .

In summary, the local moving average forecasting procedure using the delay coordinate embedding has the following steps:

- Create a trajectory matrix of time-lagged vectors describing the entire history of the system from time series data (Equation 3.13).
- Assume a functional relationship between past states and future states in the neighborhood of some x^* .
- Search the trajectory matrix for the closest states (distance sense) to the most recent states and form nearest neighbor (NN) matrix.

$$\mathbf{X}_{NN} = \begin{pmatrix} \mathbf{x}_1(t_1) \\ \vdots \\ \mathbf{x}_k(t_k) \end{pmatrix}_{k \times 2m} . \quad (3.18)$$

where \mathbf{x}_i result in smallest k values of $\|\mathbf{x}_i(t_i) - \mathbf{x}(t_N)\|$, $1 \leq i \leq k \equiv$ number of nearest neighbors.

- Obtain the evolved neighbors from the trajectory matrix and form evolved neighbor matrix (ENM.)

$$\mathbf{X}_{ENM} = \begin{pmatrix} \mathbf{x}_1(t_1 + \delta t) \\ \vdots \\ \mathbf{x}_k(t_k + \delta t) \end{pmatrix}_{k \times 2m} . \quad (3.19)$$

where δt is the resolution of the time series.

- Calculate **center-of-mass** (COM) of nearest states and form localized neighbor matrix (LNM) and evolved localized nearest neighbor matrix (ELNM).

$$\mathbf{X}_{ENM} = \begin{pmatrix} \mathbf{x}_1(t_1) - \mathbf{x}_{com}^*(t_N) \\ \vdots \\ \mathbf{x}_k(t_k) - \mathbf{x}_{com}^*(t_N) \end{pmatrix}_{k \times 2m} = \begin{pmatrix} \mathbf{x}'_1(t_1) \\ \vdots \\ \mathbf{x}'_k(t_k) \end{pmatrix} \quad (3.20)$$

where $\mathbf{x}_{com}^*(t_N) = \left(\frac{\sum_{i=1}^k \mathbf{x}_{i,1}(t_i)}{k}, \dots, \frac{\sum_{i=1}^k \mathbf{x}_{i,1}(t_i)}{k} \right)$. The ELNM is constructed with a similarly defined center-of-mass.

- Solve the matrix equation for the evolution of neighborhood to obtain the first order term of the functional. Solve the equation to obtain \mathbf{A} : $\mathbf{X}'_{LNM} \mathbf{A} = \mathbf{X}'_{ELNM} \Rightarrow \mathbf{A}_{m \times m} = (\mathbf{X}'_{LNM})^{-1} \mathbf{X}'_{ELNM}$. One may use SVD to find $(\mathbf{X}'_{LNM})^{-1} = \mathbf{V} \mathbf{W}^{-1} \mathbf{U}^T = \mathbf{V}(\text{diag}(1/\omega_j)) \mathbf{U}^T$.
- Form the affine model which best fits the reduced LNM to the reduced ELNM.

$$\mathbf{L}[\mathbf{x}] = \mathbf{A} \mathbf{x} + \mathbf{c}. \quad (3.21)$$

where $\mathbf{c} \equiv \mathbf{x}_{com}^*(t_N + \delta t)$

- Project the COM-subtracted recent state onto the LNM reduced subplane and evaluate the affine model. Evaluate $\mathbf{L} \left[(\mathbf{x}(t_N) - \mathbf{x}_{com}^*(t_N))' \right]$ which gives a linear approximation to $\mathbf{x}(t_{N+1})$
- The first component of the model output vector is the scalar prediction for the time series.

$$(\tilde{\mathbf{x}}(t_{N+1}))_1 \approx \mathbf{F}[\mathbf{x}(t_N)] = O(t_{N+1}). \quad (3.22)$$

To illustrate the applications of the method on time series forecasting, we apply this procedure to a well known input-output system, viz. synchronized Lorenz system. In this system, the x -component of the first Lorenz attractor is used as a driver for the second Lorenz attractor. Both attractor use same parameters $r = 28, b = 8.0/3, \sigma = 10$. And the y -component of the second Lorenz can be considered as an output of the non-autonomous chaotic dynamical system driven by the x -component of the first Lorenz attractor as an input. The input x -component of the first attractor is shown on Figure 3.13(a), and the output y -component of the second attractor and its forecasts are shown in Figure 3.13(b). The NMSE of the real output data and its prediction results is only 0.05.

The modeling of the solar wind-magnetosphere coupling with the use of local-linear average moving filter has provided many new results on the nature of the dynamics of the magnetosphere system. Before we describe the new studies, we revisit some of the results by using the local-linear average moving filters [*Vassilidis et al., 1995*]. The 31st *Bargatze et al. [1985]* interval is used to make forecasts by using the local moving average filter with the optimized parameters as shown in Figure 3.14. The local linear SVD filter and mean field filter are used to calculate the evolution function of the neighborhood, respectively. From Figure 3.14(b) and 3.14(d), it is clear that the both predicted AL indices capture the main changes of the magnetospheric dynamics during substorms in both nonlinear prediction filters. Thus both these filters yield good prediction results and are feasible forecasting tools.

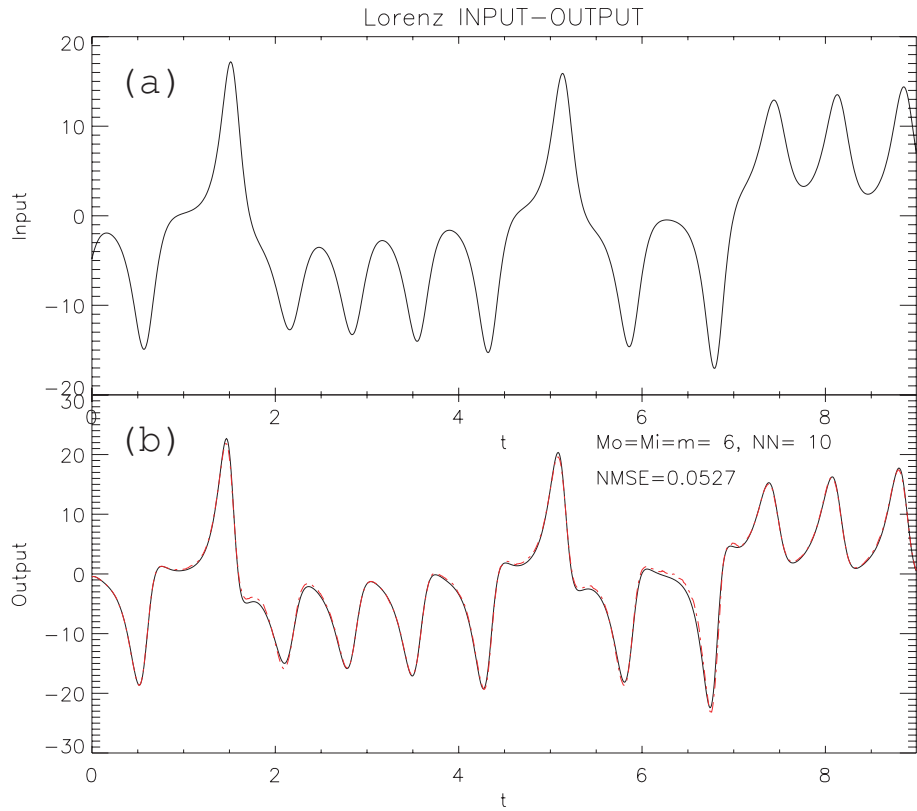


Figure 3.13: Long-term prediction on y component of synchronized Lorenz attractor. The driven x component of Lorenz is shown on the upper panel, the local linear moving average model output and the observed data are shown on the bottom panel. (black solid line is observed data, red dashed line is predicted data)

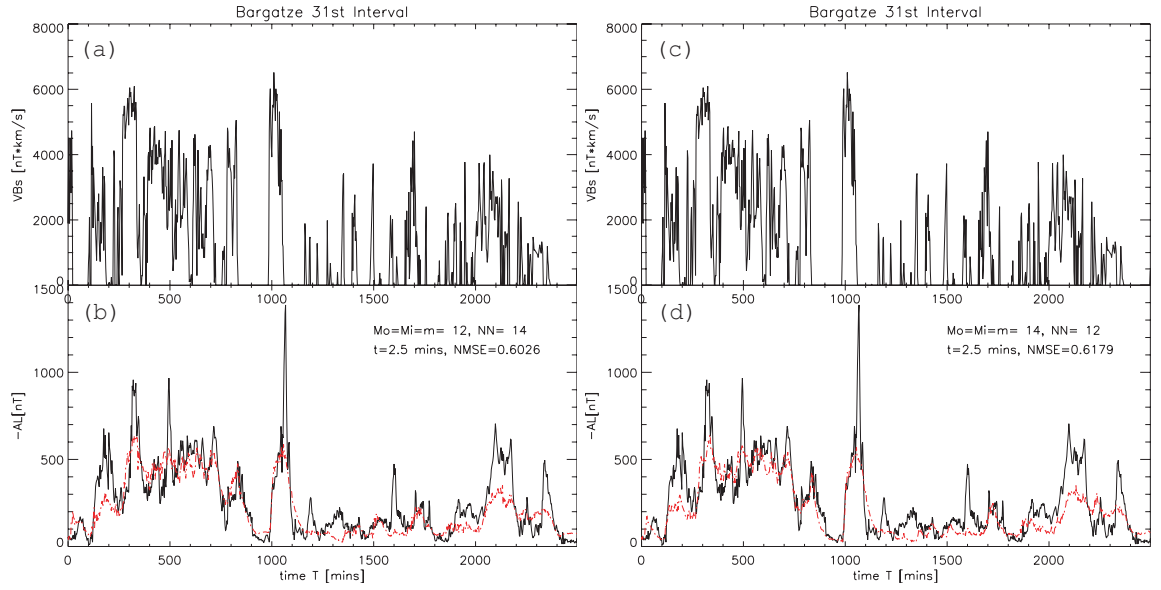


Figure 3.14: Long-term predictions of AL time series in the 31st interval of *Bargatze et al.*[1985] database. The model input $-VB_S$ time series is shown on the upper panels. The bottom panel shows the model output (red line) together with the observed AL (black line) data. The left panels are from Local linear filter, and the right panels are from mean field filter.

3.6 Low-Dimensional Models with Specified Processes

The nonlinear dynamical model derived from time series data does not depend on the physical process but contain all the dynamical details inherent in the data. Considering the leading process during substorms to be magnetic reconnection, simplified low-dimensional models with a set of coupled ordinary differential equations have been developed [*Klimas, 1992; Horton and Doxas, 1996*].

A three dimensional Faraday loop model of the magnetotail was developed considering the magnetic field geometry and plasma content of the magnetotail [*Klimas et al., 1992*]. This time-dependent global convection model is a nonlinear model and motivated by the transition from regular to chaotic loading and unloading. The model can be characterized as a nonlinear damped harmonic oscillator that is driven by the loading-unloading cycle. It is a second-order ordinary differential equation with variable coefficients that governs the time evolution of the cross-tail electric field in the current sheet. Several of the parameters which enter the Faraday loop model are fixed by requiring the model to reproduce observable substorm behavior.

Another model of the solar wind driven magnetosphere-ionosphere system (WINDMI) was developed for the substorm dynamics [*Horton and Doxas, 1996, 1998*]. This model considers the global flow of energy from the solar wind through the magnetosphere to the ionosphere. The WINDMI model, which is a six dimensional model, is based on the magnetic reconnection in the night-side magnetotail, coupled to the ionosphere by the region 1 currents. The equations of this model describe a complex driven-damped dynamical system and exhibits a variety of dy-

namical states including low-level steady plasma convection, quasiperiodic releases of geotail stored plasma energy into the ionospheric substorms, and states of continuous strong unloading provisionally identified as magnetic storms. The six ODEs representing the magnetosphere-ionosphere system, with the consideration of the energy balance relations, can provide physically meaningful values for the major energy distribution in the magnetosphere [*Thiffeault and Horton, 1996*].

The WINDMI model provides a possibility of understanding truly global aspects of magnetospheric physics in a simple way, but not from local or point measurements [*Smith et al., 2000*]. An important advantage of the WINDMI model is that energy conservation guarantees a bound on the division of the solar wind power into the various major energy components. The value of the parameters used in the model were initially selected from geometrical and plasma parameters known from the physics of the magnetotail-ionosphere system. These value were adjusted by comparisons between the model output and observational data, known as the minimum of the average relative variance. The database of intermediate and high level of geomagnetic activity [*Bargatze et al., 1985*] were chosen to test the performance of the system [*Horton et al., 1999, 2001*]. The WINDMI model can capture many magnetospheric features, although the errors are relative large.

The low dimensional models with specified process, such as WINDMI model, can be considered as alternatives to the predictive models derived entirely from the data. These methods of modeling and forecasting complement each other and a better understanding their strengths and weaknesses can lead to improved space weather forecasting tools.

3.7 New Database for Spatio-Temporal Dynamics during Active Periods

The widely used database [Bargatze *et al.*, 1985] is for a low activity period and thus is not suitable for modeling the periods of high activity. Two new databases are compiled to overcome this difficulty. The first database is for the years 2001, corresponding to the peak of the last solar cycle, and consists of the solar wind and auroral electrojet index data. The second database is for year 2002 and consists of the data of the solar wind, *AL* and magnetic field variations at 57 ground magnetometer stations.

The datasets compiled for the studies in this thesis contain solar wind plasma and IMF key parameters, and ground magnetometer measurements (years 2001 and 2002). The first database includes the solar wind data obtained from ACE through Coordinated Data Analysis Web (CDAWEB) at 64 sec and 4 min time resolution in the geocentric solar magnetospheric (GSM) coordinates, and the year 2001 *AL* index data obtained from the World Data Center (WDC), Kyoto. This database is discussed in detail in Chapter 4. The second database includes year 2002 *AL* index data derived from the Assimilative Mapping of Ionospheric Electrodynamics (AMIE) model [Aaron Ridley, private communication], and the ground measurements from three ground-based observation network: CANUPOS (Canadian Auroral Network for the Open Program Unified Study), IMAGE (International Monitor for Auroral Geomagnetic Effects) and WDC. Currently the data from a total 57 ground magnetometers, 13 of them from CANOPUS, 26 from IMAGE and 18 from WDC, have

been compiled. The specifications of these magnetometer stations are given in Table. 3.1. And the details of the database used in the different parts in this thesis are fully discussed in the following chapters.

3.8 Summary

The solar wind is the driver of geomagnetic activity and the coupled solar wind-magnetosphere system can be viewed as an input-output system. The phase space in which the dynamics of the coupled system evolves can be reconstructed from the geomagnetic indices and solar wind data using the techniques of time delay embedding. The basis for using this technique is the nonlinearity of the magnetosphere which couples different degrees of freedom and the dissipation which limits the phase space volume, thus yielding a system that can be described in terms of a small number of leading variables obtained from the data. Predictability is a natural consequence of the property of low dimensionality. To develop forecasting tools and to forecast geomagnetic activity, the use of the nonlinear dynamical models derived from time series data is critical.

Nonlinear dynamical models of the magnetosphere derived from observational time series data using phase space reconstruction techniques have advanced our understanding of its dynamics. In particular, it is now recognized that the dynamics is dominated by global features, thus showing an overall coherence in the magnetosphere. This forms the basis for the predictability of the magnetospheric behavior and space weather. These techniques have been successful in developing nonlinear

models for predicting the global dynamics in terms of the geomagnetic indices, such as the auroral electrojet index AL .

To overcome the deficiency of the databases in the high activity periods, two new databases near the peak of the last solar cycle were compiled for the further studies.

Table 3.1: Ground Magnetometer Stations

CANOPUS				IMAGE			
COfde	Full Name	Geographic Coordinates		Code	Full Name	Magnetic Coordinates	
		Lat.(° N)	Lon.(° E)			Lat.(° N)	Lon.(° E)
CH	Fort-Churchill	265.920	58.763	NAL	Ny-Alesund	11.950	78.920
CO	Contwoyto-Lake	248.750	65.754	LYR	Longyearbyen	15.820	78.200
DA	Dawson	220.890	64.048	HOR	Hornsund	15.600	77.000
ES	Eskimo-Point	265.950	61.106	HOP	Hopen-Island	25.010	76.510
GI	Gillam	265.360	56.376	BJN	Bear-Island	19.200	74.500
IS	Island-Lake	265.340	53.856	TRO	Tromso	18.940	69.660
MM	Fort-Mcmurray	248.790	56.657	AND	Andenes	16.030	69.300
PI	Pinawa	263.960	50.199	LEK	Leknes	13.540	68.130
RA	Rankin-Inlet	267.890	62.824	ABK	Abisko	18.820	68.350
RB	Rabbit-Lake	256.320	58.222	KIR	Kiruna	20.420	67.840
SI	Fort-Simpson	238.770	61.756	LOZ	Lovozero	35.080	67.970
SM	Fort-Smith	248.050	60.017	SOR	Soroya	22.220	70.540
TA	Taloyoak	266.450	69.540	MAS	Masi	23.700	69.460
WDC				IVA	Ivalo	27.290	68.560
Code	Full Name	Lat.(° N)	Lon.(° E)	MUO	Muonio	23.530	68.020
ALE	Alert	297.50	82.500	PEL	Pello	24.080	66.900
BJN	Bjornoya	19.200	74.500	SOD	Sodankyla	26.630	67.370
BMT	BeijingMingTombs	116.200	40.300	RVK	Rorvik	10.980	64.940
CBI	Chichijima	142.180	27.100	OUJ	Oulujarvi	27.230	64.520
CSY	Casey	100.530	-66.280	HAN	Hankasalmi	26.650	62.300
HTY	Hatizyo	139.820	33.080	DOB	Dombas	09.110	62.070
HUA	Huancayo	284.670	-12.050	NUR	Nurmijarvi	24.650	60.500
KAK	Kakioka	140.190	36.230	UPS	Uppsala	17.350	59.900
KNY	Kanoya	130.880	31.420	TAR	Tartu	26.460	58.260
LRM	Learmonth	114.100	-22.220	KIL	Kilpisjarvi	20.790	69.020
LRV	Leirvogur	338.300	64.180	KEV	Kevo	27.010	69.760
MAB	Manhay	5.680	50.300				
MAW	Mawson	62.880	-67.600				
MMB	Memambetsu	144.190	43.910				
TND	Tondano	124.950	1.290				
TRO	Tromso	18.950	69.670				
TSU	Tsumeb	17.700	-19.220				
VAL	Valentia	349.750	51.930				

Chapter 4

Modeling and Prediction of the Magnetospheric Dynamics During Intense Geospace Storms

4.1 Introduction

The solar wind-magnetosphere coupling is enhanced when IMF turns southward, leading to geospace storms and substorms. When the IMF remains southward for an extended interval, the ring current grows under the influence of the solar wind variations, leading to geospace storms with typical time scales of days, characterized by strong decreases on the surface magnetic field. The solar wind characteristics are strongly dependent on the solar activity, and thus the data derived models obtained for a dataset corresponding to a particular period need not apply to another period. For example, the well known Bargatze [1985] (hereafter referred to as the BBMH dataset) dataset corresponds to a period of weak solar activity.

During October-November 2003, nearly 2 years after the last solar maximum, two extremely big geospace storms occurred. Two strong coronal mass ejections (CME) occurred on October 28-29, 2003 with velocities of more than 2000 km/s near the Sun and reached Earth after a travel time of only 19 hours. The arrival of the first coronal mass ejection from the center of the solar disc led to an immediate start of a G5 storm, an extreme geomagnetic storm on the NOAA space weather scale

that runs from G1 to G5. During October 29-31, 2003, the Advanced Composition Explorer (ACE), located at $220 R_E$ upstream of Earth, detected extreme conditions in the solar wind. The solar wind speed reached as high as 2000 km/s and the maximum of the southward component of the interplanetary magnetic field (IMF) was -58.31 nT, leading to geomagnetic field index AL values as low as -2778 nT. On April 19, 2002 and November 20, 2003, two more extreme geomagnetic storms driven by solar wind velocities of 696 km/s and 766 km/s, and southward IMF of -32.03 nT and -53.02 nT, measured by ACE led to the AL index values of -1851 nT and -2499 nT, respectively. These three intense geospace storms provide important opportunities for the study of the nonlinear phase space reconstruction under extreme conditions. In order to model and predict such intense storms, a correlated database of the solar wind and magnetospheric variables of the year 2001, which is close to the peak period of 11-year solar cycle, is compiled.

4.2 Correlated Database of Solar Wind-Magnetosphere Coupling under Strong Driving

4.2.1 Year 2001 Storm Database for Solar Maximum Period

During the period of maximum solar activity, the magnetosphere is strongly driven and the year 2001 near the last solar maximum was chosen for compiling a database for such an epoch. This database contains solar wind flow speed V , the north-south component B_Z of the IMF and the AL index for the 11 months of 2001 (January to November). The solar wind data were obtained from ACE at 64 sec and

4 min time resolution in the geocentric solar magnetospheric (GSM) coordinates, and the AL index data were obtained from the World Data Center (WDC), Kyoto. The ACE data, obtained from Coordinated Data Analysis Web (CDAWEB), and the AL data were averaged to 5 min resolution. The ACE satellite is located at the L1 point, about 218-248 R_E from Earth and with a solar wind bulk speed of 420 km/s along the Sun-Earth direction, it gives a 60 minutes lead time. So in compiling the correlated database of the geomagnetic field measurements (AL), and the solar wind (VB_Z), a time lag of 1-hour is used. The location of ACE at a fixed position largely removes the problem of propagating the solar wind data from the spacecraft to the magnetopause.

The solar wind data for 2001 were compiled for a set of data intervals, each defined as any continuous data longer than 12 hours with no more than half-hour data gap. The dataset contains 81 intervals with periods 12 hours to 3 days long. The data gaps in these intervals were interpolated linearly to satisfy the data continuity requirement. Two criteria, similar to those used in *Bargatze et al.* [1985], were used to select the data segments: (1) A data interval bounded at both ends by around 1 hours segment of weak, nearly zero, solar wind input and small values of the AL index. (2) If more than one data segment with a day long time data interval satisfy the first criterion, the interval is separated into different intervals.

During January-November 2001, there were 81 such data intervals containing 33931 data points at 5-min resolution, satisfying the above conditions. The correlated solar wind induced electric field VB_Z and the auroral electrojet index AL for 81 intense storm intervals during year 2001 are shown on Figure 4.1. During

this period of strong solar activity, intense substorms and storms were triggered with higher frequency. If we define a strong geomagnetic storm as having Dst less than -100 nT, we find that there are 12 such storms in 2001 compared with 4 such storms in 1995 and 1 in 1996. Thus the 2001 database is appropriate for studying the properties of geomagnetic activity during a solar maximum. The selected 81 events are separated into 3 activity levels by the average values of VB_S : medium ($\langle VB_S \rangle \leq 1500$ nT·km/s), high (1500 nT·km/s $\leq \langle VB_S \rangle \leq 2500$ nT·km/s), and super ($\langle VB_S \rangle \geq 2500$ nT·km/s). To model a specific event, we choose the corresponding activity level to which it belongs and use it as a reference database.

A comparison of the characteristic parameters of the year 2001 and the BBMH is given in Table 4.1 and Figure 4.2. From the definitions of the activity levels and Table 1, we find that most data intervals of the BBMH database are in the medium activity level, and a small number of data intervals are in high activity level. However, for the 2001 dataset, only 2/5 of the data intervals are in the medium level group, and 3/5 of the data intervals are in the high and super activity levels. The counts of VB_S and AL within the proper bin sizes for the BBMH and the 2001 datasets are shown on Figure 4.2. It clearly shows that the 2001 database has much more events with VB_S bigger than 1000 nT·km/s and AL smaller than -200 nT. And also there are many cases with VB_S bigger than 10,000 nT·km/s and AL smaller than -1000 nT (belonging to the super group) in the 2001 database but none in the BBMH database. It may be noted that $B_S = -B_Z$ for southward IMF, so that VB_S is positive. We calculated the mean value of solar wind condition input for each data intervals. Among these mean value of each event, the maximum one

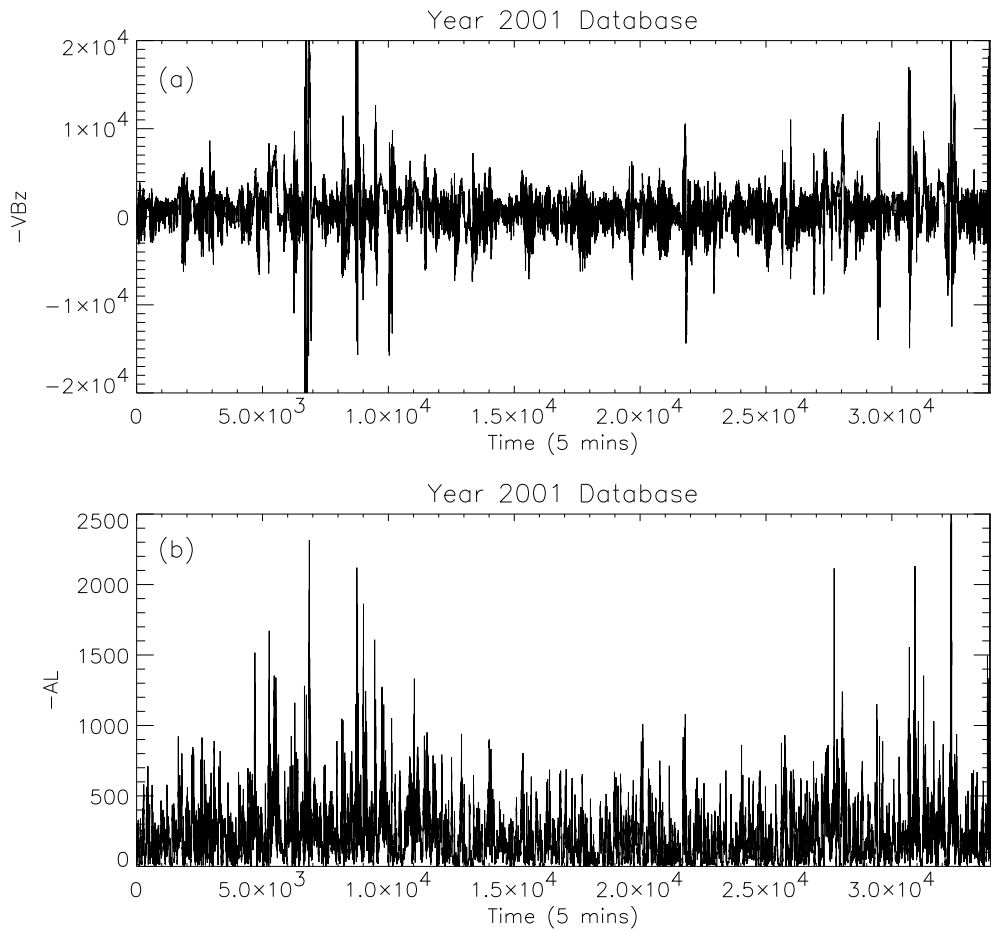


Figure 4.1: The correlated solar wind induced electric field (VB_Z) and the auroral electrojet index AL for 81 intense storm intervals during year 2001. The geomagnetic activity in these intervals during the peak of the last solar cycle is very high and corresponds to strong driving by the solar wind. (a) VB_Z (b) AL .

of VB_S for the year 2001 and the BBMH databases are 13116 nT·km/s and 2989 nT·km/s, respectively, showing the strong driving of the magnetosphere in 2001.

Table 4.1: Comparison between BBMH [*Bargatze et al.*, 1985] and Year 2001 databases

	Level 1 (Medium)	Level 2 (High)	Level 3 (Super)
BBMH Database	26	7	1
Year 2001 Database	33	32	16

4.2.2 The Intense Geospace Storms during October-November 2003 and April 2002

During 2002-2003 there were three intense storms, occurring in April 2002, October 2003, and November 2003. The solar wind data from ACE through CDAWEB and the corresponding geomagnetic field index AL were compiled for these storms. However for the October 2003 event there were some problems with the solar wind velocity data during October 28-30, 2003, the critical period for the interaction of the violent solar wind with the geomagnetic field. For this period we adopt the modified solar wind velocity data [*Skoug et al.*, 2004] from Solar Wind Electron Proton Alpha Monitor (SWEPAM) [*McComas et al.*, 1998], whose measurement capability was pushed to the limit during the event. The SWEPAM ion instrument collects data in two modes-normal (tracking) mode and search mode, each of which required

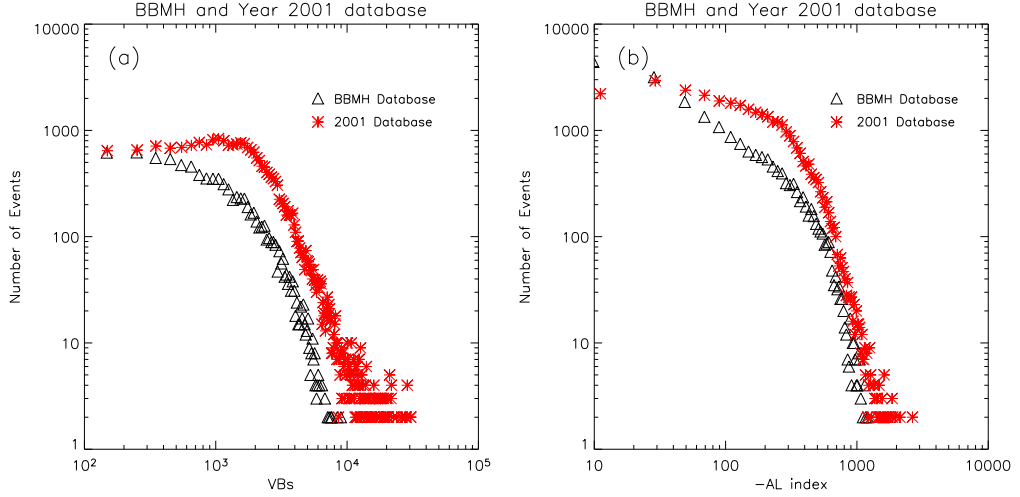


Figure 4.2: Statistics of the events in the BBMH and Year 2001 databases. (a) VB_S (bin size = 100) (b) AL (bin size = 20). The events represent averages over the indicated bin sizes. The differences in the magnetospheric response in the two databases are not as pronounced as in the solar wind variable.

64 seconds for a full measurement. During the period beginning at 1241UT on 28 October and ending at 0051UT on 31 October, the high background noise levels due to the penetrating radiation from the intense solar energetic particle caused the solar wind tracking algorithm to fail in recording the solar wind during the high-speed events. However the search mode data with 33-minute resolution are available during this high-speed solar wind period and are used in compiling the database.

For the November 2003 and April 2002 events, the solar wind velocity and IMF data are from ACE obtained through CDAWEB (<http://cdaweb.gsfc.nasa.gov/>). In the correlated databases, 1-hour time delays were applied on all these events, as in the 2001 database.

4.3 Local-Linear Weighted Mean Filter

In the mean field model discussed at Chapter 3, all the states in the specified neighborhood, the NN nearest neighbors were used to obtain the center of mass by a simple averaging procedure. It is however clear that the states close to the current state should contribute more than those farther away. A new filter based on the mean field filter is used to improve the accuracy and efficiency of predictions. This weighted filter takes into account the distance of the nearest neighbors and is not just a simple average over the NN nearest neighbors. Since some of the nearest neighbors are farther from each other and also farther away from the center of mass, a set of weight factors \mathbf{g} which depend inversely on the distances of each nearest neighbor from the center of mass is introduced as

$$g_k = \frac{1}{d_k^2} / \sum_{i=1}^{NN} \frac{1}{d_i^2}. \quad (4.1)$$

where d_i is the Euclidean distance of the i th nearest neighbor from the center of mass. Then the predicted output is modified as:

$$O_{n+1} = \frac{1}{NN} \sum_{k=1}^{NN} X_k \bullet g_k. \quad (4.2)$$

If all the nearest neighbors have the same distance from the center of mass, the weighted mean-field filter will yield the same prediction as the mean field filter. However if the NN nearest neighbors have a wide range of the distances, the nearest neighbors will dominate the output of the prediction. The inclusion of nearest neighbors farther away should not affect the prediction significantly as these will have smaller weights, thus making the predictions less sensitive on NN .

4.4 Modeling and Prediction During Superstorms

4.4.1 October-November 2003 Superstorms

The weighted mean field filter is used to model the solar wind-magnetosphere coupling during the superstorms of October-November 2003. The earlier works by *Vassiliadis et al.* [1995], *Weigel et al.* [1999] and *Ukhorskiy et al.* [2002], used VB_S as the model input and applied the nonlinear moving-average filter, neural network filter and mean field average filter, respectively. It was shown that using appropriate parameters the filter responses are stable and yield good long-term predictions. The best filter parameters were chosen to be those yielding the minima of the prediction errors. In these studies, the solar wind input was taken to be VB_S , the product of the solar wind velocity and the southward component of IMF, and consequently the input becomes zero when the IMF is northward.

In the studies below, we take the solar wind input as VB_Z , which includes both the northward and southward components of IMF. This enables the model to include the effects of northward IMF, although these may be weaker than those of the southward IMF.

In order to obtain the optimal nonlinear weighted mean field filter for superstorms, the following steps are adopted. First, the activity level of the solar wind driving is computed by averaging the southward component of VB_Z . Then both the input (VB_Z) and output (AL) of the time interval corresponding to the same activity level of the magnetospheric activity from the 2001 database are selected as the training set. For the two superstorms, the super level ($\langle VB_S \rangle \geq 2500$ nT·km/s)

of the 2001 database is selected. Second, using all the selected data intervals of input (VB_Z) and its corresponding output (AL) as a training set, the index AL is predicted for the superstorms using the weighted mean filter discussed above. The normalized mean square error (NMSE) is used to determine the optimal parameters for the prediction by comparing the predicted and actual AL . In this model, the time resolution (5 min) of the training set is chosen as the time delay T , and the other three free parameters are used to minimize the NMSE. The first two parameters are the embedding dimensions M_I and M_O , and as in the previous studies, we take $m = M_I = M_O$, which determines the vector length in the phase space to be $2m$. The third parameter is the number of nearest neighbors NN . A wide range of values of these parameters are used in the model to obtain the optimal predictions for the superstorms of November 19-23 and October 26-November 01 of 2003 and these are shown in Figure 4.3. The solar wind convective electric field ($-VB_Z$) for these events is shown in Figures 4.3a and 4.3c. There is a sudden enhancement of the solar wind convective electric field VB_S in the early part of these events that drives the geospace storms. The predicted and real AL are plotted in the panels (b) and (d) of Figure 4.3. The solid lines represent the real AL and the dotted lines represent the predicted AL . Iterative predictions of the November 2003 storm were carried out for 7500 minutes (125 hours) with a minimum NMSE of 0.792 and the maximum correlation coefficient of 0.758. Also for the predictions of the October 2003 storm, made for 10000 minutes (167 hours), yielded a minimum NMSE of 0.911 and a maximum correlation coefficient of 0.714. In these figures the model output closely reproduces the large-scale variations of AL and captures some of the most

abrupt changes. Also preceding the AL minima, there are sharp jumps with positive VB_Z , corresponding to the abrupt enhancements of the northward IMF. However, the southward IMF is the main driver of the geomagnetic storms, and it is not clear how well the model captures the effects of positive IMF enhancements.

In the earlier studies using the BBMH dataset [e.g., *Vassiliadis et al.*, 1995; *Weigel et al.*, 1999; *Ukhorskiy et al.*, 2002, 2004], a major part of the dataset was used as the training set and the predictions were made for the remainder of the dataset. Consequently there were many similar states in the phase space. However for the two superstorms of 2003, it is hard to find so many similar big substorms in the available databases, such as that of year 2001. The nearest neighbor searches in these cases yields only a few states close to the superstorms. If we use a large number of nearest neighbors and a simple arithmetic averaging, the output of the model is smoothed over these and cannot capture the peak of the substorms. In such cases the weight factor \mathbf{g} plays an important role and the averaging procedure yields improved predictions.

The dependence of the prediction errors on the filter parameters is shown in Figure 4.4, in which the panels (a) - (d) shows the surface plots of NMSE as functions of NN and m for the November and October 2003 storms. For the November 2003 storm, the NMSE surface plots have a significant drop from 1.2 to 0.75 when m is increased from 1 to 3. With a further increase of m , NMSE returns back to 0.9 and has similar values until m reaches 11. With m in the range 12-14, the NMSE surface reaches another minimum, independent of NN . With further increase of m , NMSE starts to grow again. The overall structure of the surface plot of NMSE

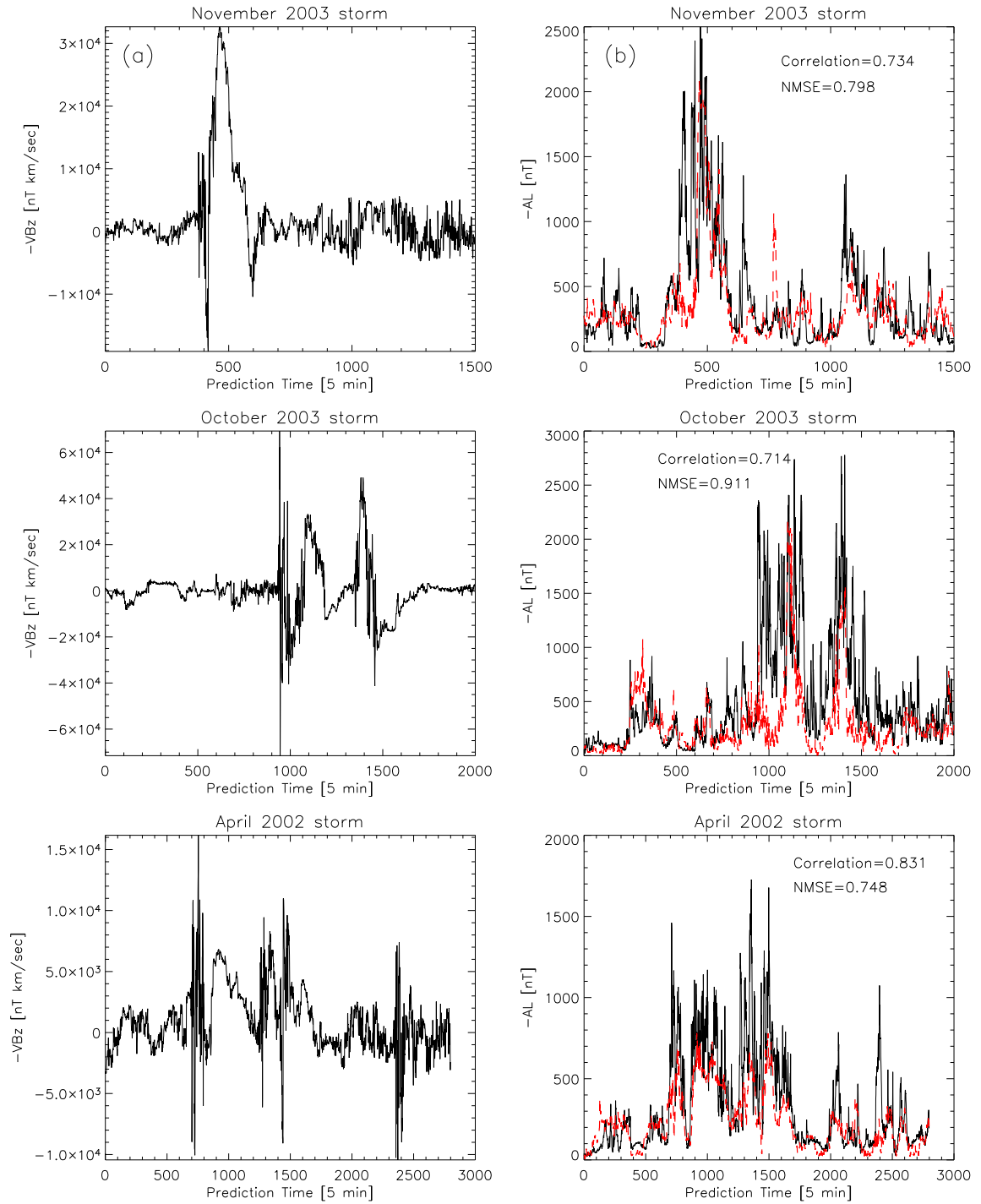


Figure 4.3: The weighted mean-field predictions for storms: (a-b): November 19-26, 2003, (c-d): October 26-November 03, 2003, and (e-f): April 15-24, 2002. The left panel is $-VB_z$, and the right panel is the real AL (black solid line) and predicted AL (red dotted line)

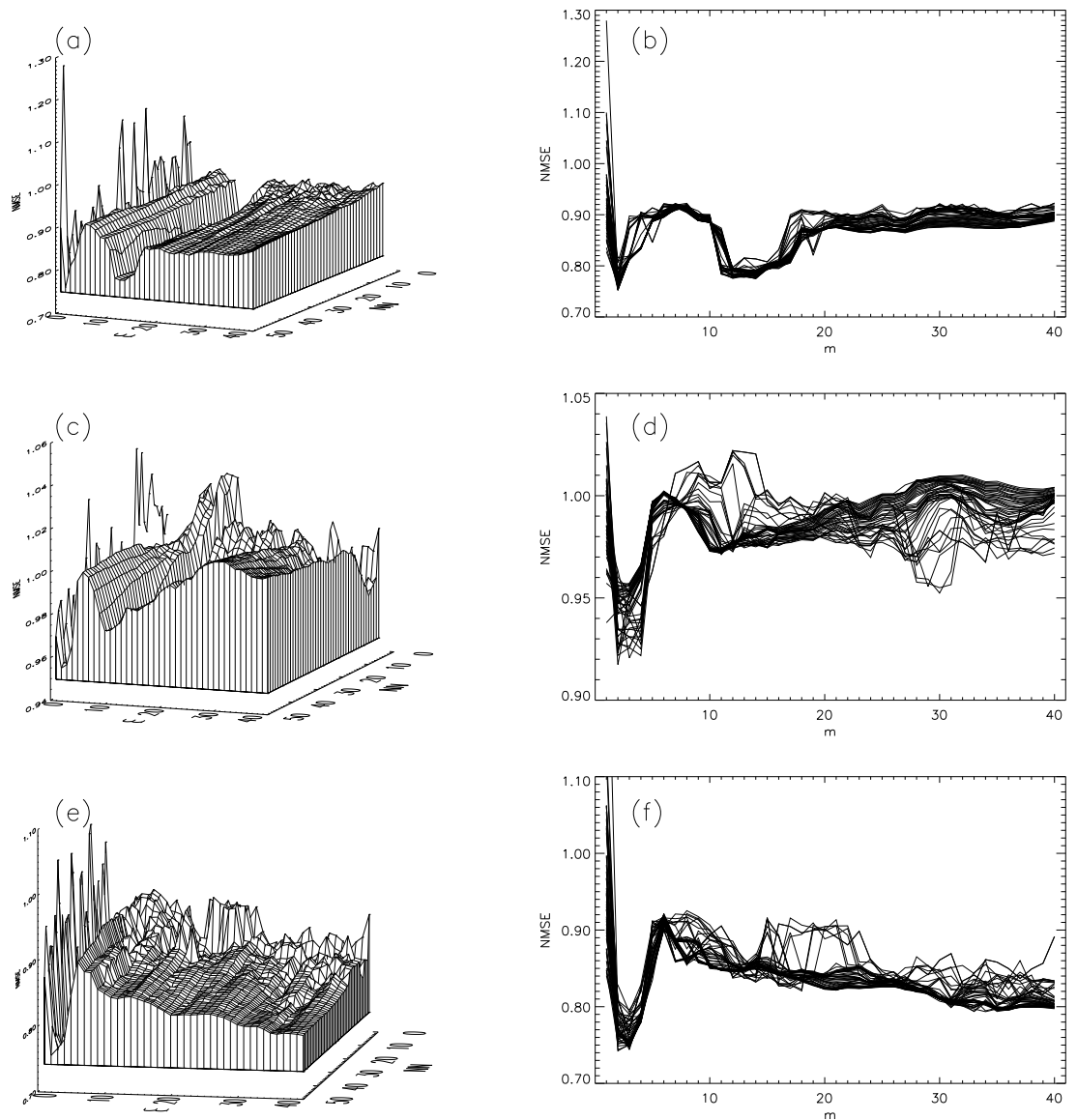


Figure 4.4: The normalized mean square error (NMSE) of the predictions plotted against the number of nearest neighbors NN and the embedding dimension m . (a-b): November storm; (c-d): October storm; (e-f): April storm. Plots on right are the 2D projection from the left panel. Each line represents a particular value of NN .

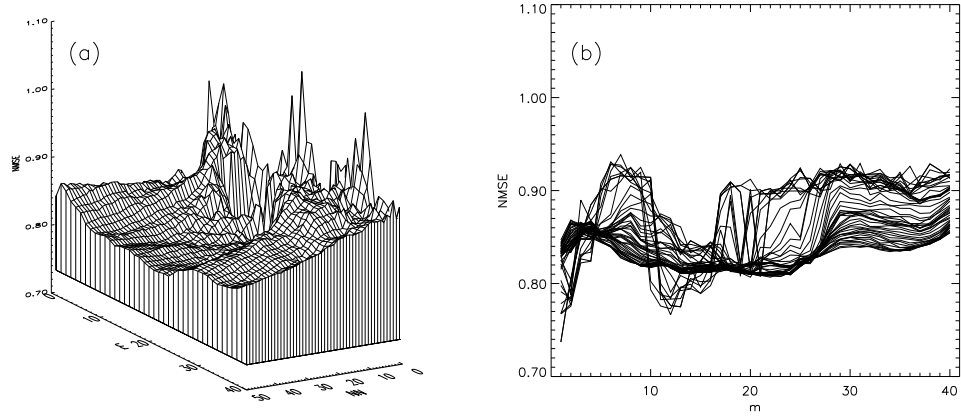


Figure 4.5: The normalized mean square error (NMSE) of the predictions of the November 2003 using mean-field filter model. (a): NMSE surface plot; (b): 2D projection of (a).

is a “canyon” with a broader range of m values for all values of NN , than in the earlier models [Vassiliadis *et al.*, 1995; Ukhorskiy *et al.*, 2002]. The prediction results have similar correlations and prediction error surfaces when m varies in the range 12 - 14, independent of the number of nearest neighbors NN . This also indicates the dimension of the magnetosphere phase space to be 12 - 14, which indicates the presence of the multiscale component of the solar wind-magnetospheric activity [Ukhorskiy *et al.*, 2002].

However for the October 2003 storm, the NMSE surface is more complicated. The valley in m around 2-4, shown in Panels (c) and (d) of Figure 4.4, is much deeper than that around 10-12, and yield better predictions. During 29-30 October 2003, SWEPAM measured solar wind speed in excess of 1850 km/s, almost the highest speed directly measured in the solar wind. But, despite the unusual high speed many of the other solar wind parameters were not particularly unusual in

comparison with other large events [Skoug *et al.*, 2004]. Comparing with the solar wind speed at 750 km/s on November 20, 2003, the October 2003 high-speed events in which the solar wind speed was 2-3 times faster than those typical for large solar wind transient events did not produce an unusually larger geomagnetic storm. This may be due to the short-lived B_S , although large in value, and so the storm of October 2003 is driven partially by the dynamic pressure and large positive B_Z . The phase space in this case is expected to be significantly different from those of the storms caused by southward IMF.

The role of the weight factor \mathbf{g} and the dominance by the first few nearest neighbors can be examined by using the values computed from the dataset. For the November 2003 storm, a total of 8 nearest neighbors are considered in the model. Out of these the weight factors for the first 3 accounts for 48% on average, with the maximum reaching as high as 85%. Thus the first three nearest neighbors dominate the predictions, which enhance the ability of such models to make better predictions under extreme conditions when the number of similar events in the database is small. To further understand the effects of the \mathbf{g} factor, we use the mean field average filter without the weight factors to predict the substorms during November 2003 using the year 2001 database. The NMSE surface plots of predicted AL are shown in Figure 4.5, following the same format as in Figure 4.4. The best prediction results are almost the same as those of the weighted mean field filter. The NMSE surface plots for the two cases, with and without the weight factors, are similar for NN values in the range 1 - 11, and when NN is larger than 12, the bottom of the NMSE profile become wider and higher in Figure 4.5. This means that the predictions become

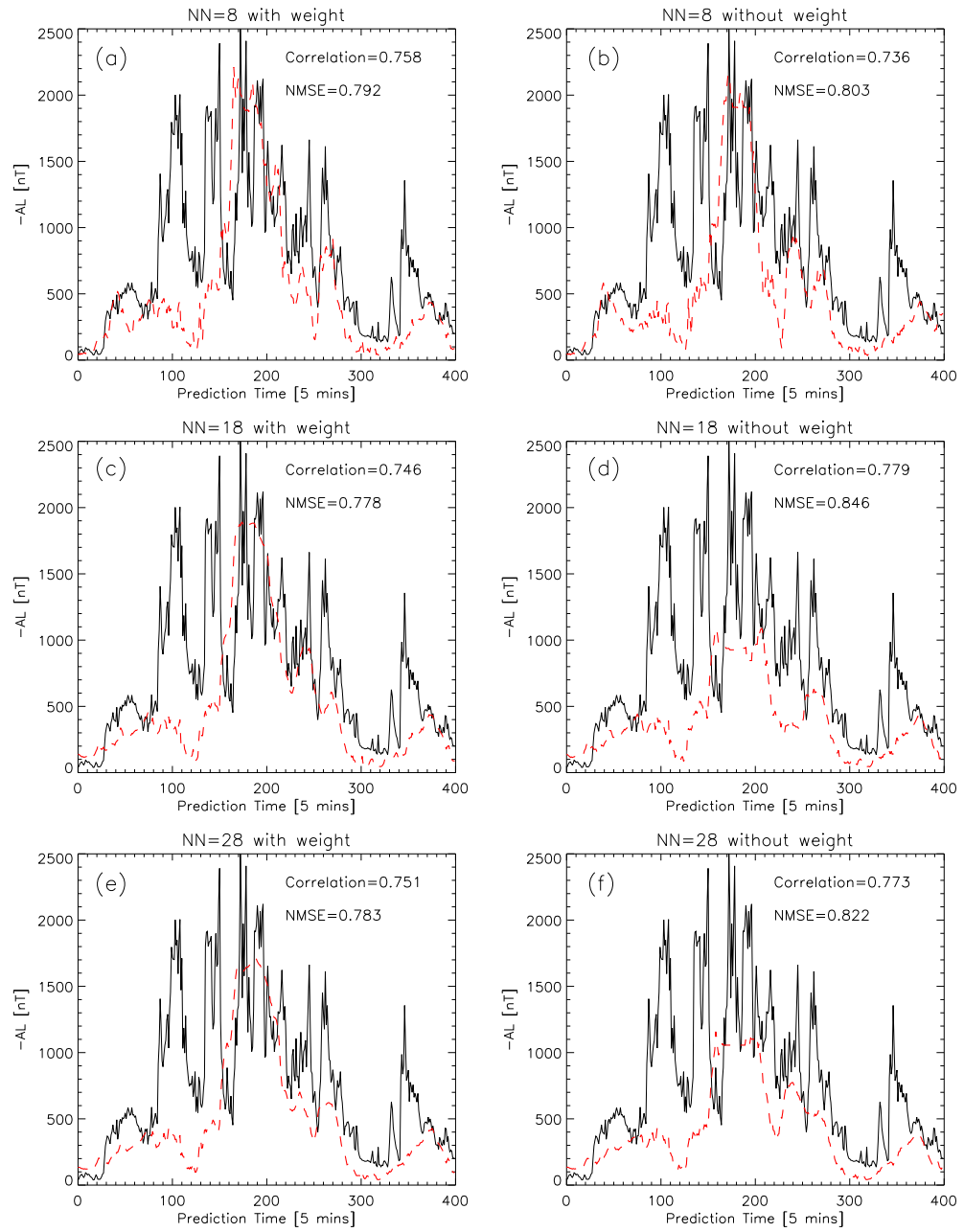


Figure 4.6: The comparison of the mean field filter model on the prediction of the November 2003 storm with weight factor and without the weight factor \mathbf{g} . (a) $NN = 8$ with \mathbf{g} ; (b) $NN = 8$ without \mathbf{g} ; (c) $NN = 18$ with \mathbf{g} ; (d) $NN = 18$ without \mathbf{g} ; (e) $NN = 28$ with \mathbf{g} ; (f) $NN = 28$ with \mathbf{g}

worse with the increase of NN when it is bigger than 12. Thus the weight factor \mathbf{g} is effective in controlling the quality of the predictions by reducing the contributions of the nearest neighbors which are farther away when their distances are distributed over a wide range. Also since the prediction efficiency drops when NN is larger than 12, better predictions are made with NN less than 12. Among the predictions with NN less than 12, we can define a narrow canyon when m is around 2-5 so that the whole phase space is unfolded well and yields good predictions. The resulting predictions are similar to those obtained using the weighted mean filter prediction.

The weight factor \mathbf{g} is expected to play an important role in the cases, such as extreme events, which do not have many similar states in the database. The predictions from different nearest neighbors (NN s) with and without the weight factors \mathbf{g} are shown in Figure 4.6. To highlight the differences clearly, the period of low activity before and after the storm main phase are neglected. In the case of $NN = 8$, the predictions with and without g factors are very similar. When NN is bigger than 12 as suggested from NMSE surface plots, the prediction with \mathbf{g} become much better than those without it. The comparisons for $NN = 18$ and $NN = 28$ during the storm main phase are shown on Figure 4.6(c)-(f). The effect of \mathbf{g} is more pronounced in the case $NN = 18$, as higher values lead to averaging over more neighbors which are significantly different.

4.4.2 April 2002 Superstorm

The intense storm of 17-20 April 2002 has a minimum value of Dst of -154.2 nT, occurring around 0900UT on April 20, 2002, and is a good case for modeling using the 2001 database for intense geomagnetic activity. During this storm the AL index reached a minimum of AL_{min} at -1851 nT and $-VB_Zmax$ reached a peak value of 16652 nT·km/s. A comparison of key parameters of the storms is given in Table 4.2. Compared with the AL index minima of -2778 nT and -2499 nT, and $-VB_Z$ maxima of 69330 nT·km/s and 32640 nT·km/s, respectively, for the October and November 2003 storms, it is clear that the storm of April 2002 is the least active of the three storms. Also from the two databases, it is clear that the biggest events during the year 1973 [Bargatze *et al.*, 1985] and the year 2001 are widely different. The biggest storm in year 2001 has the maximum and mean of solar wind input value of 32015 nT·km/s and 13116 nT·km/s, respectively, and the corresponding AL index values are -2701 nT and -450 nT. On the other hand, the biggest storms during 1973, it has only 14291 nT·km/s as the maximum of the solar wind input and 2989 nT·km/s as its mean value, which are about 30% - 50% of the corresponding values for the year 2001. Also the corresponding AL index values of -1867 nT and -413 nT are much smaller than those in the year 2001 database. From Table 4.2, we also note that the April 2002 storm has intensity similar to the biggest event of the BBMH database, and October and November 2003 storms have intensities similar with the biggest one in the year 2001 database.

The weighted mean field filter technique was applied to the April, 2002 storm

Table 4.2: Intensities of October 2003, November 2003, and April 2002 storms

	October 2003	November 2003	April 2002	Biggest Event in BBMH	Biggest Event in Year 2001
Maximum $-VB_Z$ (nT km/s)	69,330	32,640	16,652	14,291	32,015
Minimum AL (nT)	-2778	-2499	-1851	-1867	-2701
Mean of $-VB_Z$ (nT km/s)	4619	3560	2511	2989	13,116
Mean of AL (nT)	-441	-315	-316	-413	-450

period using the 2001 database as the training set. The prediction results and NMSE surface plots are shown in Figure 4.3(e and f) and Figure 4.4(e and f). The iterative predictions of the April 2002 storm were carried out for 10 days they yield a minimum NMSE of 0.748 and a maximum correlation of 0.831. These figures show that the model also reproduces the large-scale variations of AL very well. Also the NMSE surface plots (Figure 4.4) shows a single valley around $m \sim 2 - 4$ independent the value of NN , in contrast to the two minima in the cases of October and November 2003 storms.

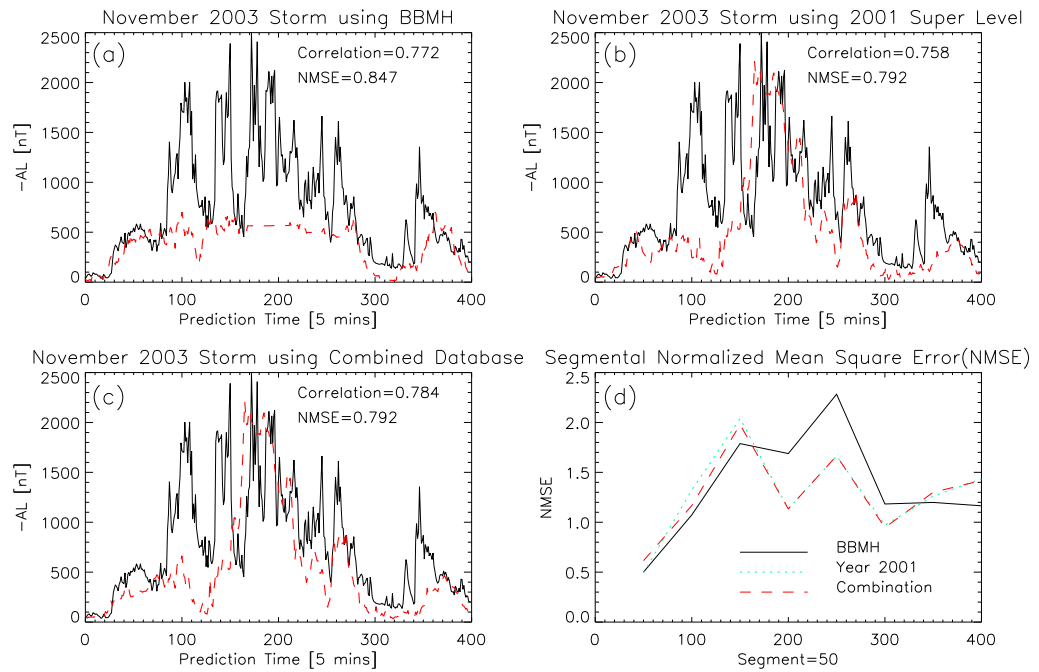


Figure 4.7: The weighted mean field predictions on November 2003 storm using the BBMH, Year 2001 and combined databases. The solid line is real AL data, dotted line is predicted results. (a) BBMH database (b) Year 2001 database (c) Combined database (d) NMSE for 250-minute segments, solid line represent BBMH database, dotted line represent Year 2001 database, dashed line represent combined database.

4.4.3 Comparison of Predictions using Bargatze *et al.* [1985] and Year 2001 databases

In order to compare the predictions using different databases as the training sets, the storms of November 2003 and April 2002 are predicted using the BBMH database. To highlight the differences clearly, the periods of quiet and low activity before and after the main phase of the storms are neglected. The results of the storm of November 2003 are shown in Figure 4.7(a). It is clear that the peaks of AL cannot be predicted, mainly due to the absence of similar strong substorms in the BBMH database. The overall predictions have an NMSE of 0.847 and a correlation coefficient of 0.772. The predictions of for the same period using the year 2001 database and the combined database of year 2001 and BBMH are shown on Figure 4.7(b) and 4.7(c), respectively. A comparison of these predictions, Figure 4.7(a)-(c), shows the substantial improvement with the inclusion of the year 2001 database, either as the complete training set or as a part of a bigger training set. This is clearly due to the presence of many events in the year 2001 database similar to those in the November 2003 storm. It may be noted that the correlations among the predicted and actual AL in the three cases are not substantially different in spite of the very different qualities of the predictions, e.g., between Figure 4.7(a) and Figure 4.7(b) or Figure 4.7(c). This brings into focus the inability of the linear correlation functions to provide an adequate measure of the predictive capability. In order to compare the predictability for different segments of the database, the November 2003 event was separated into smaller segments of 250 min or 50 data

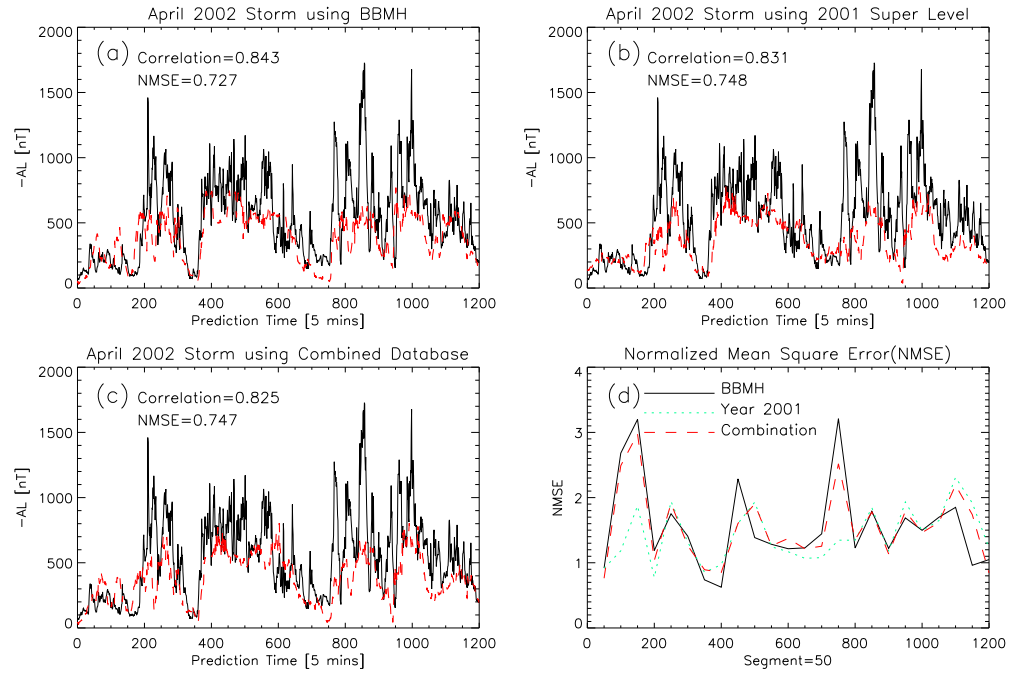


Figure 4.8: The weighted mean field predictions on April 2002 storm using the BBMH, Year 2001 and Combined databases. The solid line is real AL data, dotted line is predicted results. (a) BBMH database (b) Year 2001 database (c) Combined database (d) NMSE for 250-minute segments, solid line represent BBMH database, dotted line represent Year 2001 database, dashed line represent combined database.

points each. The comparisons of the NMSE for the different segments are shown in Figure 4.7(d). It is clear that the NMSE for the data segments with large values of AL in the 2001 dataset are much smaller than those of the similar segments in the BBMH dataset. Also the NMSE of the segments of the year 2001 database are very similar to those of the BBMH and 2001 datasets combined. Further, except for the segments containing the large values of AL , the NMSE for the other segments have similar values for both the datasets.

The BBMH database is expected to yield better predictions for the storm of

April 2002, a weaker storm compared to the November 2003 storm. The predictions and their NMSE are shown in Figure 4.8(a)-(c). The predictions are found to be almost the same when the three databases, viz. BBMH, year 2001, and the two combined, are used as the training sets. Also the NMSE values for 250 min intervals are shown in Figure 4.8(d), and that NMSE have similar values in most of the segments.

The NMSE values for the predictions of all three storms, using the BBMH, Year 2001 and combined databases as the training sets, are given in Table 4.3. This table compares not only the NMSE for the predictions for the whole storm period, but also those of the main phase of the storms. The errors in the predictions of the storm main phases are systematically higher than those for the whole storm period. This could be expected, at least partly, as the periods of intense activity are harder to predict than the less active periods. However it should be noted that the NMSE values is depend on the number of points N , as given by Eq. (3.17), and it can yield smaller values for larger N . Thus the NMSE values yield a useful comparison when the data sizes are similar and caution is essential otherwise. For the predictions for the entire intervals of October and November 2003 storms, NMSEs when the BBMH database alone is used are 1.003 and 0.847, respectively, much larger than the corresponding values of 0.911 and 0.792 for the year 2001 database. However NMSE for the year 2001 database alone are 0.911 and 0.792, which are very close to those for the combined database, viz. 0.939 and 0.792, respectively. The same results are obtained on the NMSE values for the main phases of the October and November 2003 storm predictions. For the main phase of the October event, NMSE

is 1.181 when the BBMH database is used, 1.064 for the 2001 database, and 1.101 for the two databases combined. For the November 2003 event, NMSE is 1.059 for the BBMH database, 0.979 for the 2001 database, and 0.955 for the combined database. Thus there are no significant differences in these cases.

Table 4.3: The normalized mean square error (NMSE) of the predictions of all three storms using the BBMH, Year 2001 and combined databases. Both the NMSE of the whole event and of the main phases are shown

	BBHM Database		2001 Level 3 Database		BBHM+2001 Level 3 Database	
	Whole	Main Phase	Whole	Main Phase	Whole	Main Phase
October 2003	1.003	1.181	0.911	1.064	0.939	1.101
November 2003	0.847	1.059	0.792	0.979	0.792	0.955
April 2002	0.727	0.924	0.748	0.952	0.747	0.943

In the case of the April 2002 storm, all the NMSE values obtained using different databases are similar, indicating that the BBMH and the 2001 databases yield similar predictions. However the 2001 database is a better choice for the October-November 2003 storms, as the comparisons in Figures 4.7 and 4.8 indicate. The remaining parts, viz. the quieter periods of the October-November 2003 and the whole of April 2002 storms can be predicted very well using both the BBMH and Year 2001 databases as the training sets.

To further compare the predictions using the BBMH and year 2001 databases,

the observed and predicted AL are plotted in Figure 4.9. The left panels are the plots of the observed and predicted AL index for the three storms. In order to examine the comparison in more detail, the AL values are averaged over a bin size of 20 nT, and this yields the three right panels. These plots show the similarities and differences between the two databases. For the April 2002 storm, the predictions (Figure 4.9, panels e and f), show no significant difference for the two datasets. However, for the November 2003 (Figure 4.9, panels a and b), and the October 2003 (Figure 4.9, panels c and d) storms, the predictions using the 2001 database are much better than those using the BBMH database. On the other hand, for the low activity periods of these two storms, the predictions are similar. Also for all three storms, the low activity periods show most points along the 45-degree line, implying predictions with high accuracy. The predictions for the entire April 2002 storm and the low activity periods of the 2003 October-November storms show similarities. The differences in the predictions are mainly in the high activity parts of 2003 October-November storms. These similarities and differences indicate that the magnetospheric responses to similar solar wind inputs are similar. The differences are likely to be due to the lack of the big events in the BBMH database, rather than fundamental differences in the magnetospheric response.

The analysis of the storms with different intensities and using different databases indicates that the geomagnetic response during the solar minimum and solar maximum periods have similar behavior. The 2001 and BBMH databases can thus be considered to complement each other. The combination of these two databases under different solar activities provides a comprehensive database for improved mod-

eling and prediction of magnetospheric activity under a wide range of solar wind conditions.

The size N of the databases used to reconstruct the phase space is an important issue. When the embedding dimension m is known, the number of the data in each dimension can be estimated broadly as $N^{1/m}$. Thus when m is relative large, the number of the data in each dimension will be significant small, which limit the phase space reconstruction, in principle. However, in our studies, $m \simeq 2 - 3$ for these 3 superstorms are proper embedding dimensions, in which cases the reconstructed phase space are well populated. Comparing the prediction results from using the databases of year 2002 level ($N = 5743$), BBMH ($N = 21108$) and the combination of the year 2002 and BBMH ($N = 55039$) in Figure 4.7 and 4.8, the prediction results are similar and independent of the sizes of the databases, indicating that the databases in our study are large enough for proper embedding.

4.5 Discussion

The modeling of magnetospheric response to strong driving by the solar wind is important not only for a better understanding of the solar wind - magnetosphere coupling and but also for developing our capability to forecast extreme conditions. During the last solar maximum there were many intense geospace storms and the existing models had limited success in forecasting these accurately. In order to develop better models and improve forecasting capability, a correlated database of the solar wind and the magnetospheric response was compiled for the year 2001

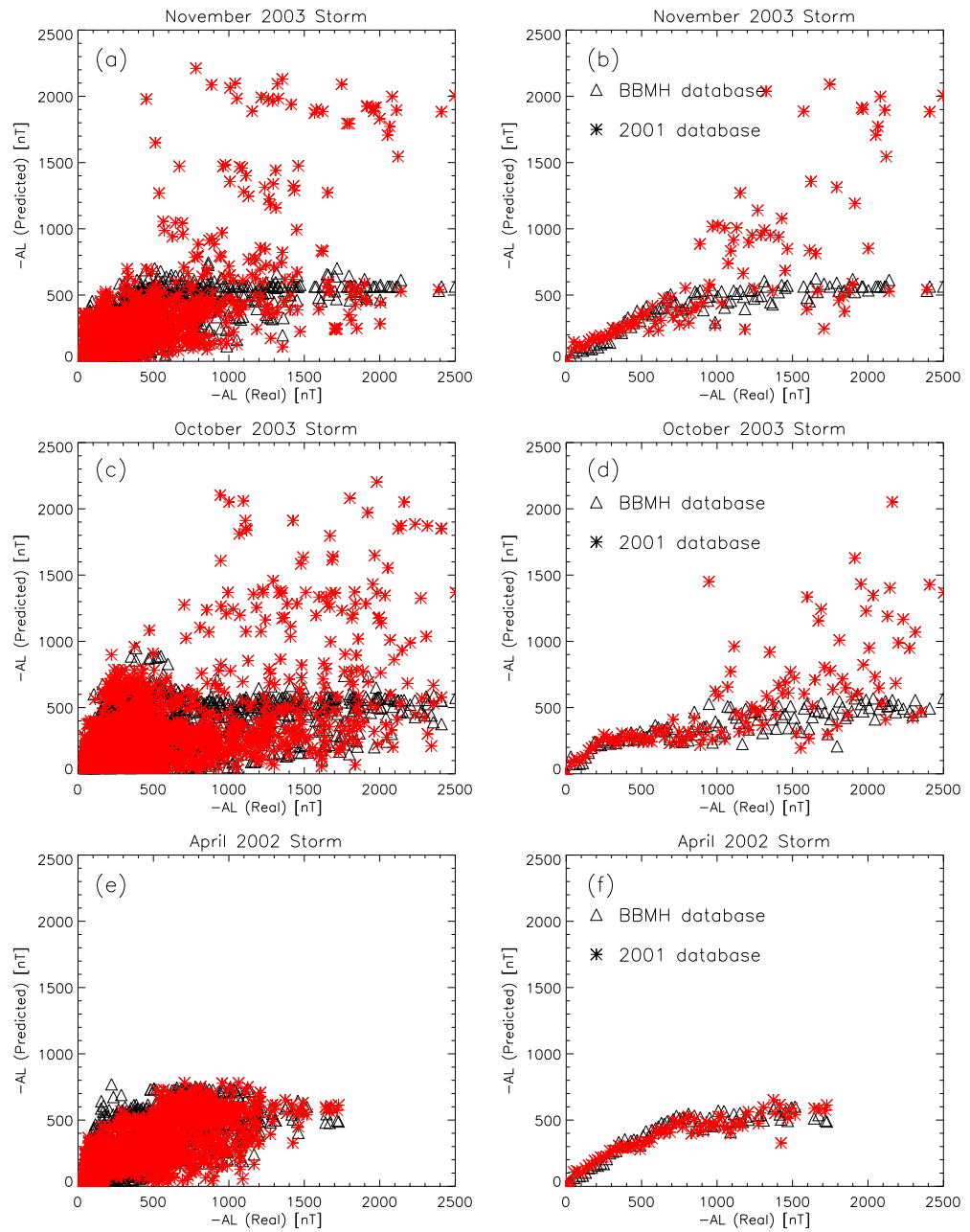


Figure 4.9: Comparison of real AL and predicted AL under the BBMH and Year 2001 databases. (a-b): November 2003 storm; (c-d): October 2003 storm; (e-f): April 2002 storm. The right panel are the averaged values at bin size=20 of the events in the left panel.

during the peak of the last solar cycle. In this database, the solar wind variable is the induced electric field and the magnetospheric response is the auroral electrojet index AL . This database is particularly well-suited for modeling using the phase space reconstruction techniques.

The mean field approach to the modeling of the global magnetospheric dynamics [Ukhorskiy *et al.*, 2002, 2004] is used to develop nonlinear dynamical models of the magnetospheric response from the year 2001 database. These predictions are then compared with the models based on the *Bargatze et al.* [1985] database, corresponding to a solar minimum period (1973 - 1974). The predictions for the big storms of October and November 2003 and April 2002 yields improved forecasts, especially for the intense storms.

The mean field approach has the advantage of yielding iterative predictions without having to fix model parameters, in particular the number of nearest neighbors NN and the dimension of the embedding space m [Ukhorskiy *et al.*, 2002, 2004]. However during intense storms the number of similar events is usually small and this limits the ability to predict big events. In order to improve the predictability in such situations the mean field approach is modified by assigning weights to each of the nearest neighbors. These weights are inversely proportional to the square of the distance and leads to improvements in the predictions. The forecasting capability of the model is quantified in terms of a normalized mean square error (NMSE) computed from the predicted and actual AL values.

For a reconstructed phase space, the evolutions of the system variables are closely related to the corresponding number of embedding dimension. The dynam-

ical model of the solar wind - magnetosphere coupling specifies its evolution in the reconstructed input-output phase space of dimension $2m$. The prediction error surfaces obtained from NMSE values, averaged over different nearest neighbors NN , and are shown on Figure 4.10 for all 3 storms. The prediction error surfaces have minima for $m \sim 2 - 4$, indicating proper embedding and this is in agreement with the results of *Vassiliadis et al.* [1995] based on the modeling using the BBMH database. These results show the low dimensional nature of the coupled solar wind-magnetosphere system on the global scale, corresponding to the length of the best filter $m * T \sim 10 - 20$ mins, which is in agreement with the loading time scales. However for the November 2003 event, NMSE surface yield another minimum at $m \sim 12 - 14$ corresponding the time scale of 60-70 min lengths, which is close to the typical unloading time scale. These values of the embedding dimension are in agreement with the results of *Ukhorskiy et al.* [2002], based on the modeling using the BBMH database. The averaged NMSE for the April 2002 storm (Figure 4.10), indicates a local minimum for $m \sim 12 - 14$, although it has lower value when m is over 20. Figure 4.10 shows that there are two minima in averaged NMSE, and these may be associated with directly-driven and unloading time scales. Considering that the October and November 2003 storms are stronger storms than the April 2002 storm, the differences in NMSE minima indicate a more complicated phase space for the superstorms compared to that of moderate storms. Further analysis is needed to draw clear conclusions on the nature of the reconstructed phase spaces under different solar activity conditions. However, it is clear that the embedding dimension $m \sim 2 - 4$, corresponding to time scales of 10-20 mins, yields minimum

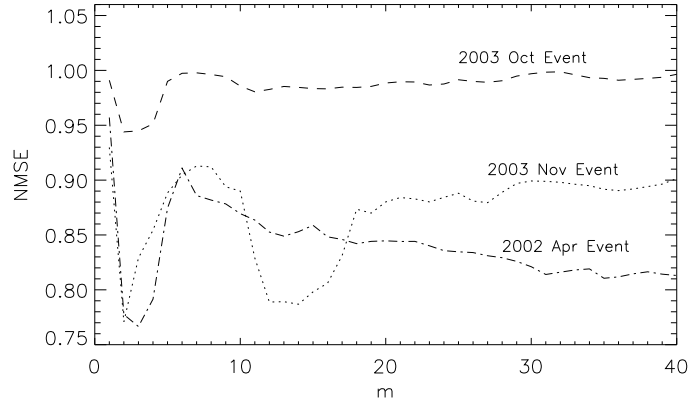


Figure 4.10: The averaged NMSEs over an ensemble of nearest neighbors (NN). Three curves correspond to averages of curves in Figure 4.4b, 4.4d, 4.4f, respectively. All three cases have two minima: the first minimum at $m=2-4$ is clear, while the second one at $m \sim 12 - 14$ is clear for the November 2003 storm and less so for the other two storms.

errors in all cases. The second minima in NMSE at $m \sim 12 - 14$ is more prominent in the case of the November 2003 storm. For modeling purposes, embedding dimension of $m \sim 12 - 14$ seems appropriate from the point of view of smaller errors in the predictions. However it raises important issues from the viewpoint of a proper reconstruction of the phase space.

Chapter 5

Spatio-Temporal Dynamics of the Magnetosphere During Geospace Storms: Mutual Information Analysis

5.1 Introduction

The magnetospheric response to the solar wind consists of global, regional and local features. The global features described by geomagnetic indices were discussed in the previous chapters. The spatio-temporal dynamics of the magnetosphere, viz. the spatial structures, the coupling among them, and their evolution, are not well studied nor understood. It is however a critical component of space weather studies because of the importance of forecasting the location and timing of events with potential for damage to technological systems.

Most of the recent studies based on state space reconstruction have used the global geomagnetic indices, such as the auroral electrojet index AL and disturbance storm time index Dst , as the representations of the geomagnetic activity. These studies provide a global understanding the nonlinear coupling of the solar wind and magnetosphere. The importance of understanding the spatial structure of geospace disturbances, especially for space weather studies, has led to the development of dynamical models based on the data from individual magnetometer stations [*Valdivia et al.*, 1999a; 1999b].

Valdivia et al. [1999a] modeled the evolution of the spatial structure of the ring current using the time series data from six mid-latitude ground magnetometers. A similar approach led to a two dimensional representation of the high latitude geomagnetic perturbations in magnetic latitude and magnetic local time from 15 magnetometers of the IMAGE magnetometer array [*Valdivia et al.*, 1999b].

The data from the high latitude chain of magnetometers have been used to study many geophysical processes, e.g., the double-cell convection pattern [*Friis-Christensen et al.*, 1988], field aligned current structure [*Lanzerotti et al.*, 1986], and correlations with transients in the solar wind [*Sibeck et al.*, 1989]. The development of models for spatio-temporal dynamics from the observational data is essential for advancing our understanding of the magnetosphere.

The spatial structure of the magnetosphere, e.g., during geospace storms as reflected in the ASYM index, a measure of the departure of the H perturbations from the axial symmetry expected for a ring current, arises from the correlations among different regions and from the solar wind variability. Such correlations are normally studied using linear cross-correlation functions which provide the simplest level of correlations in the system. However, considering the nonlinear nature of the magnetosphere and its evident complexity, it is essential to use functions which can reveal the more complicated dependence. The mutual information function [*Fraser and Swinney*, 1986] characterizes the degree to which a set of measured variables are independent of each other, and has been used to yield dynamical quantities such as the appropriate time delay for reconstruction of dynamics. In this chapter, the mutual information functions are used to study the spatial-temporal dynamics from

the solar wind data and the magnetic field variations measured by ground magnetometers. The average mutual information(AMI) functions are used to characterize inter-relationship among the magnetic field measurements from the high latitude magnetometer stations. Also the correlations of the average mutual information to the changes in the solar wind dynamic pressure and convective electric field are studied to yield new insights on the dominant physics. Such studies need long time series data and the dataset for the 6 month period January-June 1979 [*Kamide et al.*, 1998] is used in this study.

5.2 Mutual Information Function and Spatially Distributed Geospace Data

Along with the development of the global dynamical models, it is important to understand the correlations among the different regions of geospace and the mutual information (defined in Equation 3.6) is a suitable function for such studies. In a study focused on geomagnetic activity using *AL* data with 1-hour time resolution, *Prichard et al.* [1996] utilized the information theory to demonstrate some periodicity in substorm occurrence time from the mutual information functions. This study showed a significant level of predictability in the dynamics, in agreement with studies of the prediction using dynamical techniques. These studies [e.g.,*Edwards et al.*,2000 ; *March et al.*,2005] imply that mathematical constructs such as the mutual information are suitable to the study of the spatially dependent solar wind-magnetospheric coupling.

5.2.1 Average Mutual Information

Information theoretic functionals stress statistical relationships and emphasize both linear and nonlinear dependencies [Fraser and Swinney, 1986; Prichard and Theiler, 1995; Kantz and Schreiber, 1999]. The commonly used functions such as correlation functions are effective in bringing out the linear correlations in the data. In the studies of complex systems it becomes necessary to employ functions that can reveal both the linear and nonlinear correlations so that the underlying features of the system can be characterized properly. The function that we choose to employ is known as average mutual information (AMI) defined as Equation 3.5.

One may interpret AMI as a measure of the uncertainty of values of X_1 resolved by observing values of X_2 . Although fundamentally dimensionless, the units of AMI are commonly called *bits* to reflect the use of information in coding theory. In general, average mutual information is inversely proportional to the degree of statistical independence of its arguments. For a calculation on a time series data of a single variable, the AMI can be defined as

$$I(\tau, x, \delta) = \sum_{i=1}^K \sum_{j=1}^K p_{ij}(x(t), x(t - \tau)) \log_2 \left[\frac{p_{ij}(x(t), x(t - \tau))}{p_i(x(t))p_j(x(t - \tau))} \right] \quad (5.1)$$

where δ is defined such that $(\max(x) - \min(x))\delta^{-1} = K$, the number of bins in the discretized distributions. Here, we replace \wp by p to stress that Equation (5.1) is calculated from a finite data set and therefore is not the actual distribution, but rather, an approximation. Also, while Equation (3.5) represents a single value, Equation (5.1) is a function of the time delay τ . The function $I(\tau, x, \delta)$ is analogous

to the autocorrelation function of linear signal processing; however it is more general in the statistical sense previously described: the autocorrelation is the expectation of a quadratic polynomial statistic, while AMI represents the expectation of the average degree of independence incorporating all higher orders. Originally, AMI calculations were motivated by their ability to yield the measures of optimal time lag in the reconstruction of chaotic systems using time-delay embedding technique [*Fraser and Swinney*, 1986; *Abarbanel et al*, 1993]. However, their probabilistic nature hints at a more general applicability to any complex system. Figure 5.1(a) illustrates the calculation of AMI (Equation 5.1) for all twelve ground magnetometer stations in the auroral region and *AL* for three days of data centered on the April 3, 1979 storm. The average mutual information function of a time-lagged series represents the uncertainty in $x(t)$ resolved through knowledge of previous values of the series. Thus, $I(\tau, x_1) < I(\tau, x_2)$ implies that there is more certainty about (i.e. higher probability of certain) future values of $x_2(t)$ than $x_1(t)$, based on observations of their histories. More generally, the magnitude of this difference, $|I(\tau, x_1) - I(\tau, x_2)|$, is indicative of the degree to which different time series maintain the information content represented by Equation (5.1). It is this notion that we wish to exploit.

In analogy with time series of twelve spatially distributed magnetometers, consider n spatially separated time series, so that, one has an n -component time series $\{x_1(t), \dots, x_n(t)\}$. One may also determine the spread $\Delta_I(\tau)$ between the various $I(\tau, x_i)$ defined as

$$\Delta_I(\tau) = \max_i \{I(\tau, x_i)\} - \min_i \{I(\tau, x_i)\} \quad (5.2)$$

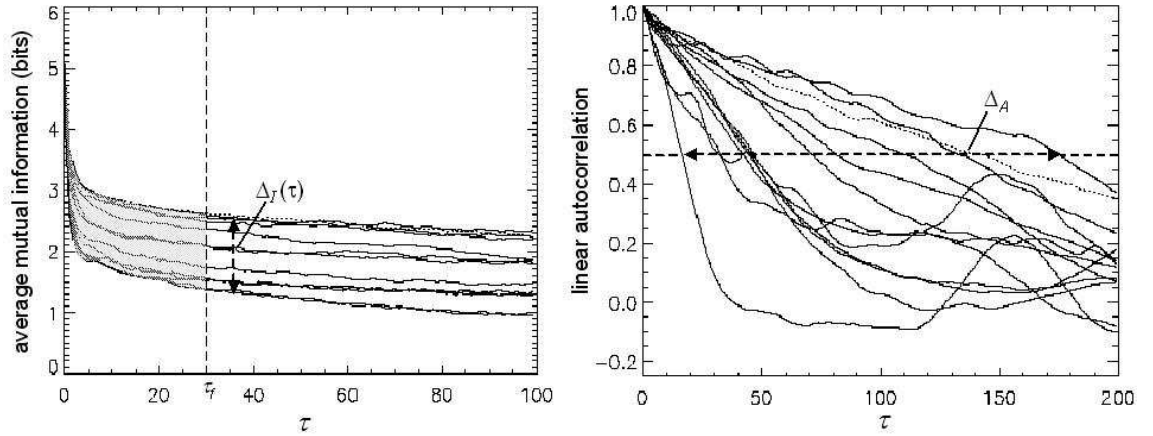


Figure 5.1: (a) Calculation of time-lagged average mutual information (AMI) for twelve magnetometer stations and AL (dotted) for three days of data centered on the April 3, 1979 storm. The shaded region is the LIMI quantity (Equation 6 in the text). The information spread (Equation 3) is also labeled. (b) Calculation of autocorrelation for the same data as (a). The localized autocorrelation spread (Equation 9) is labeled.

In accordance with the interpretation above, Equation (5.2) gives a measure of the global difference in information retention for a time delay τ . We wish to ascertain how this global measure varies in response to variations in system input and compare to variations in $I(\tau, x_{min})$. Additionally, we examine whether such a measure can better distinguish features through use of the commonly used quantities, such as the linear autocorrelation function.

We also mention the error and biases associated with computations using Equation (5.1), since they are often neglected in the literature. Naturally, information theoretic calculations will depend on the amount of data (N) and the discretization (δ) used to approximate the probability distributions. Since N will be somewhat small in many computations, one should have a reliable estimate for the

errors in the calculation. *Roulston* [1999] illustrates how the standard error formula familiar to physicists can be used to derive a relation for the variance in observed values of average mutual information. This relation is

$$\sigma_I(\tau) = \left[\frac{\ln 2}{N} \sum_{k=1}^K \sum_{l=1}^K \left[\log_2 \left(\sum_{i=1}^K p_{ki} \right) + \log_2 \left(\sum_{j=1}^K p_{jl} \right) - \log_2 p_{kl} + I(\tau, x, \delta) \right]^2 p_{kl} (1 - p_{kl}) \right]^{1/2} \quad (5.3)$$

where p_{ab} is understood to represent the joint probability $p_{ab}(x(t), x(t - \tau))$. The error is based on a Taylor expansion of Equation (3.5) to second order in the parameter $\varepsilon_k = (p_k - \wp_k)/\wp_k$ (i.e. the deviation from the "true" probability). The primary assumption is that for large enough N and δ , ε will be small.

5.2.2 Localized Integrated Mutual Information

Since the magnetospheric data sets consist of extended quiet and active periods, calculations of AMI over the entire dataset, e.g., the first six-month period of 1979 are inappropriate. Substorms represent intervals of increased informational complexity, and their specific characteristics could be lost in a calculation incorporating six months of data. To overcome this obstacle, we employ a sliding window of width w to compute the mutual information functions and the spread among them using Equations (5.1) and (5.2) for the entire magnetometer data set. Sliding calculations of information measures are effective indicators of complexity changes [*Torres and Gamero, 2000*]. Additionally, given a δ , the mutual information is generally greater as complexity increases. For situations where a disturbance is not

global (i.e., the time series for one or some stations fluctuates over a much greater range than the others), the mutual information function will likely be substantially different. To insure an appropriate baseline for the comparison of the different cases, independent of activity level, we define

$$I_l(t, x(t, w), \delta) \pm \sigma_{I_l} = \int_0^{\tau_f} I(\tau, x(t, w), \delta) d\tau \pm \int_0^{\tau_f} \sigma_I d\tau \quad (5.4)$$

as the localized integrated mutual information (LIMI). The quantity $x(t, w)$ is a time series data of length w centered at t , viz. it is defined on the interval $[t - w, t]$.

LIMI gives a means for quantifying the time scales of disparate intervals of activity at different spatial locations. We can generate a localized spread by substituting Equation (5.4) into Equation (5.2) resulting in

$$\Delta_{I_l}(t, \delta) = \max_i \{I_l(t, x_i(t, w), \delta)\} - \min_i \{I_l(t, x_i(t, w), \delta)\} \quad (5.5)$$

We can obtain a crude estimate of the error in Equation (5.5) by taking

$$\sigma_{\Delta_{I_l}}(t, \delta) = \sigma_{\max I_l} + \sigma_{\min I_l} \quad (5.6)$$

The resulting $\Delta_{I_l}(t, \delta) \pm \sigma_{\Delta_{I_l}}(t, \delta)$ is a local (in time) measure of the difference in information retention (repeatability) in a spatially extended system. The shaded region of Figure 5.1(a) delineates the quantity represented by Equation (5.5). At minimum, the LIMI spread quantifies the homogeneity of time scales at different spatial locations over an extended period of time. A broader interpretation suggests that $\Delta_{I_l}(t, \delta)$ quantifies the homogeneity of the response of the system to disturbances, whether external (solar wind induced) or internal (self-organizing). If a

disturbance is global and homogeneous in its spatial variations, the average mutual information functions should be similar at all locations. When the disturbance induces different information retention characteristics at different locations, LIMI spread will be larger. Of course, one can define a quantity similar to Equation (5.5) for the linear autocorrelation

$$A(\tau, x) = \frac{1}{\sigma_x^2} \sum_{i=1}^N [x(i + \tau) - \bar{x}][x(i) - \bar{x}] \quad (5.7)$$

where σ_x^2 is the variance of the length N series and \bar{x} is the arithmetic average. Since $-1 \leq A(\tau) \leq 1$, there is no need for the integrals of Equation (5.4). In fact, because $A(\tau)$ can be negative, an integral is ill advised. If the series is localized as in Equation (5.4), one can define the autocorrelation spread as

$$\Delta_{A_i}(t) = \max_i \{\tau_i \mid A(\tau, x_i(t, w)) = .5\} - \min_i \{\tau_i \mid A(\tau, x_i(t, w)) = .5\} \quad (5.8)$$

In other words, autocorrelation spread defined here represents the spread in autocorrelation functions at $A(\tau) = 0.5$. Figure 5.1(b) shows the calculation of autocorrelation functions for the same data as Figure 5.1(a). The dotted line with arrows represents the autocorrelation spread. One may attribute the general differences between LIMI and autocorrelation spreads to higher order, statistically significant nonlinear relationships that arise in response to disturbances in the solar wind or internally generated in the magnetosphere.

5.3 Database of Spatio-Temporal Variability of the Magnetosphere

The primary data set used in this study is one-minute resolution time series data set of the horizontal component of the magnetic field perturbations at the 12

high-latitude magnetometer stations in the auroral region. This data for the first six months of 1979 contains 260,640 values per time series with 1-min resolution for each station, and has been used for many studies [e.g., *Kamide et al.*, 1998]. Although the AL index values give a good measure of the maximum intensity of the westward electrojet, the construction of the index as an envelope raises concern about the loss of essential spatio-temporal information.

The solar wind data used for the same period of 1979, but with a time resolution of five-minutes is obtained from both the ISEE 3 and IMP8 satellites yielding the relevant solar wind parameters: the z -component of the interplanetary magnetic field, B_Z , the x -component of the solar wind velocity, V , and the number density of the ions n . From these parameters, the solar wind electric field, $E_{sw} = VB_Z$, and the dynamic pressure, $P_{ram} = nM_HV^2$, where M_H is proton mass, are derived. Since the magnetic reconnection of the dayside magnetopause, which is responsible for the transfer of the magnetic flux into the magnetosphere, is effective when B_Z is southward, we take $B_Z = -B_S$ and zero otherwise. Figure 5.2 shows the solar wind data, VB_S , P_{ram} and AL index corresponding to the first six months of 1979. It is apparent that there are plenty of active periods in both the solar wind and AL . Additionally, there are many quiet periods and intermittent bursts of activity that may or may not be correlated with the solar wind input. It is the goal of this chapter to analyze and characterize the key features of the nonlinear dynamics of the magnetosphere, especially its spatio-temporal behavior, by using mutual information function.

An important issue regarding the data sets that needs to be addressed is the

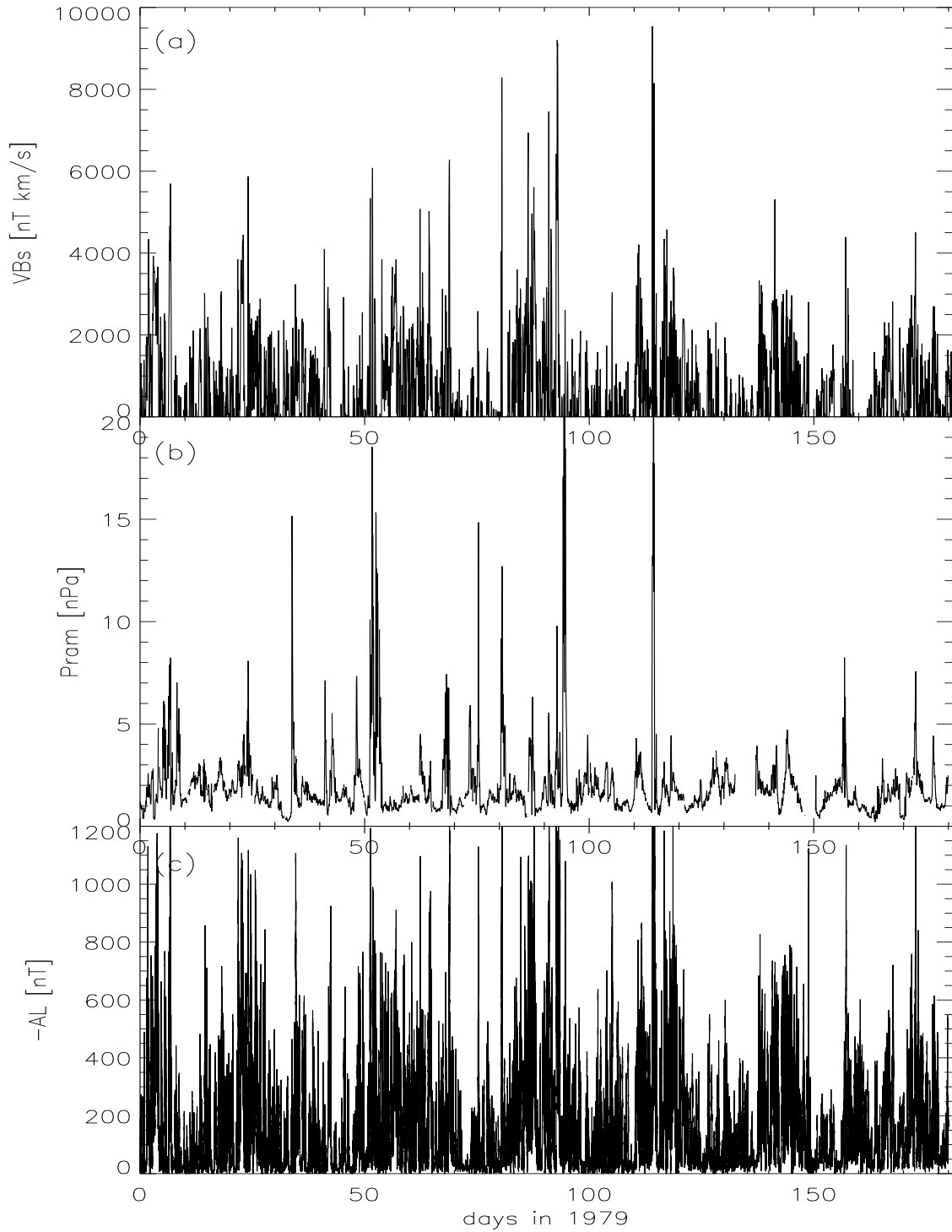


Figure 5.2: Solar wind parameters VB_S and P_{ram} for the first six months of 1979. The bottom panel is the $-AL$ index for the same period.

appearance of gaps in the ground magnetometer data. Though not significant over the entire period of 1979, the amount of magnetometer data gaps of ten minutes or more are significant enough to be of concern. Because techniques developed in this chapter utilize short duration (6 hour to few days) from the entire six months data, gaps on the order of tens minutes (representing the ratio of the invalid or missing data with the length of whole data subset $\alpha = 5\% - 10\%$) are significant. Since we will look at probability distributions of highly oscillatory data, interpolation procedures may contaminate the probability outcomes. Instead, when gaps account for greater than two percent of a magnetometer's reading over any data subset, the data is excluded from the analysis. Gaps below the two percent threshold are set equal to the average of the subset. This is expected to have a negligible effect on our results.

5.4 Average Mutual Information Analysis of Magnetospheric Dynamics

The average mutual information analysis is carried out for the above dataset of 12 high latitude stations during the first 6 months of 1979. For the computations using Equation (5.5), the moving window w is defined on the time series $[t - w, t]$, so that when the window slides every 60 minutes, total of $24 \text{ hour} \times 180 \text{ day} = 4320$ values of localized integrated self-mutual information (LIMI) are generated for each magnetometer station. The quantity represented in Equation (5.4) can be interpreted as the total amount of information conveyed by observing the

previous τ_f values of the series. We use an integral as opposed to a simple τ width, in Equation (5.4), because in contrast to autocorrelation, there is no upper bound on AMI. In general, one cannot define a mutual information time in a manner similar to autocorrelation (i.e. autocorrelation time is the time lag where autocorrelation is 1/2) because there are several minima for the mutual information of a data series. If the $I(\tau, x_i(t, w), \delta)$ are monotonically decreasing and nonintersecting to τ_f , $I(\tau, x_1(t, w), \delta) < I(\tau, x_2(t, w), \delta)$ for all $\tau < \tau_f$ implies $I(t, x_1(t, w), \delta) < I(t, x_2(t, w), \delta)$. The monotonic behavior of $I(\tau, x_i(t, w), \delta)$ is common in natural data sets, and it mimics the exponential decay in autocorrelation of systems exhibiting power-law statistics. In general, $I(\tau, x_i(t, w), \delta)$ is decreasing and nonintersecting to $\tau_f = 30$ minutes, so we chose τ_f equal to this value. To satisfy the error criteria of Equation (5.3) we use $\delta = 10$ nT.

We calculate the LIMI spread and its associated error as of Equations (5.5) and (5.6), and the localized autocorrelation spread as of Equation (5.8) for the entire six months with $w = 360$ and 1440 minutes. These window widths correspond to 1/4 day and 1 day of the 1 min resolution data. The window width is a critical choice in the estimation of the mutual information. A window width that is too long may cause long and slow variations in the mutual information functions because a sudden change can affect many sliding windows, from the moment it is located in the first sliding window to the moment it moves out of the last sliding window. Thus the mutual information will be dominated by the sudden changes although there might have been many quiet and active periods between these two windows. On the other hand, a window width that is too short may lead to poor estimates of

the mutual information when the time delay τ is relatively big compared with the length of a single sliding window. From Equation 5.1, the valid length of the dataset used to compute $p_{ij}(x(t), x(t - \tau))$ is shorter when τ is large. Also considering that substorms can last several tens minutes to several hours, the length of the dataset used to compute the mutual information should be significantly longer than these time scales. Thus we choose 2 different sliding window lengths: 6 hour and 24 hour to define two different cases. First, the focus is on the short, local but non-diurnal variations. Second, the focus is on the whole magnetosphere region including the diurnal variations. From these considerations the 6 hour and 24 hour window widths are appropriate for the studies of the long and short term variations using mutual information functions.

5.4.1 Analysis with Window Length $w = 24$ hour

We first analyze the time series data with a sliding window $w = 24$ hr or 1440 min. The locations and codes of the 12 high latitude magnetometers are given in Table 5.1 and the perturbations of the horizontal components H of the geomagnetic field under the same universal time are shown in Figure 5.3. Usually from these measurements at 12 individual stations, AL and AU indices are derived from the lower and upper envelopes of the perturbations, respectively, thus neglecting all spatial information. Consequently it is hard to determine effects of the changes in the solar wind variables such as the induced electric field and dynamic pressure on the spatial distribution of magnetospheric activity from these indices.

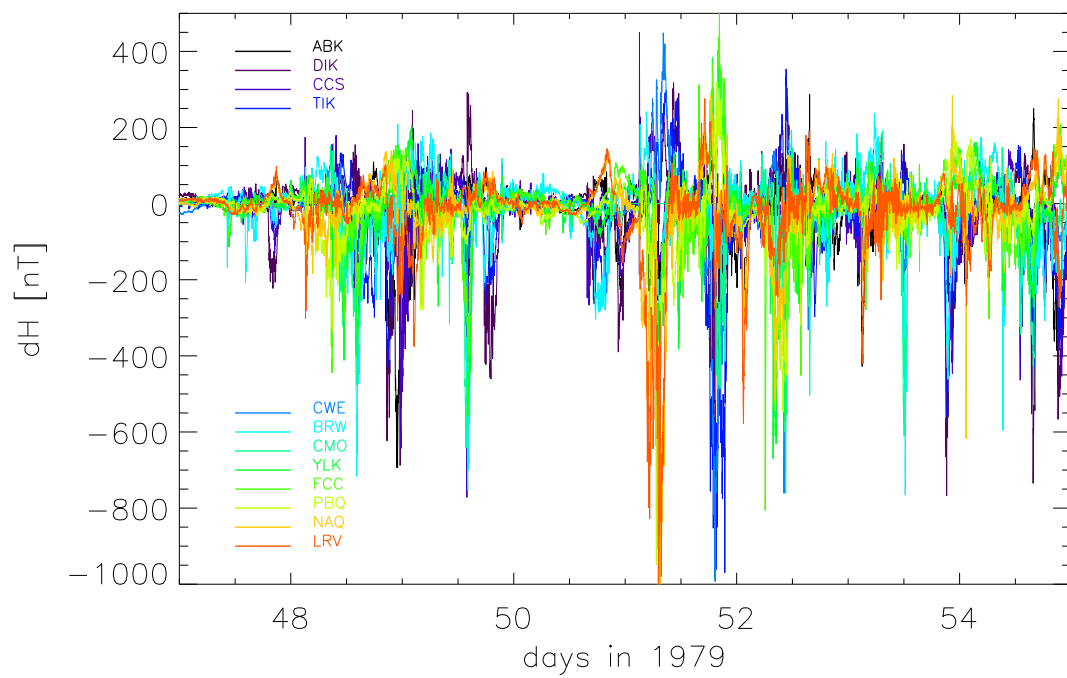


Figure 5.3: The horizontal component of the magnetic perturbations at 12 ground magnetometer stations during February 16-23, 1979. The 12 station (Table 1; *Mayaud, 1980*) color codes are indicated on the plot.

Table 5.1: Auroral Magnetometer Stations

Observatory	IAGA Code	Geographic Coordinates		Magnetic Coordinates	
		Lat.(° N)	Lon.(° E)	Lat.(° N)	Lon.(°E)
Abisko	ABK	68.36	18.82	66.04	115.08
Dixon Island	DIK	73.55	80.57	63.02	161.57
Cape Chelyuskin	CCS	77.72	104.28	66.26	176.46
Tixie Bay	TIK	71.58	129.00	60.44	191.41
Cape Wellen	CWE	66.17	190.17	61.79	237.10
Barrow	BRW	71.30	203.25	68.54	241.15
College	CMO	64.87	212.17	64.63	256.52
Yellowknife	YKC	62.40	245.60	69.00	292.80
Fort Churchill	FCC	58.80	265.90	68.70	322.77
Poste-de-la-Baleine	PBQ	55.27	282.22	66.58	347.36
Narsarsuaq	NAQ	61.20	314.16	71.21	36.79
Leirvogur	LRV	64.18	338.30	70.22	71.04

The main advantage of LIMI compared to the conventional AL and AU indices is its spatial dependence. And compared to the data from the magnetometer stations itself, LIMI can characterize in a statistical manner the correlation, linear and nonlinear, among the different regions.

The storm of February 16-23 (47-54th day of the year, defined as DOY 47-54) is analyzed first. During February 16-23, a geospace storm was driven by the solar

wind with velocities of 646-766 km/s, and southward IMF of -18 nT, leading to AL values as low as -863 nT and index Dst value going down to -106 nT. The sliding window $w = 24$ hr (1440 min) provides variations within a day, in particular those changes in the day side and the night side regions. The data gap threshold, the percentage of invalid or missing data to the whole sliding window length, $\alpha = 0.02$ is chosen to identify invalid data gaps among the data subsets of a window width w for each individual station. The AMIs of 12 individual stations computed with 24 hour windows are shown in Figure 5.4(a). Also the corresponding LIMI, the solar wind westward convective electric field VB_S and the dynamic pressure P_{ram} are shown in Figure 5.4(b)-(d). On DOY 47, an abrupt increase in the dynamic pressure the southward component of the interplanetary magnetic field drives enhanced magnetospheric activity, including a storm with $Dst = -106$ nT and many substorms. The AMIs, computed from the variations in the H component at each of the stations, increase with the increases in P_{ram} and VB_S , indicating growing complexity of the magnetosphere. This shows that the magnetospheric states have stronger correlation in time, say compared with quiet periods. However, if this magnetospheric disturbance is global and simultaneous, all 12 station distributed over the whole auroral region should have similar response to the variations of the solar wind conditions, and their AMIs should have similar characteristics, viz. similar changes in values. If the disturbance is local and it will have significant time delays relative to the different station locations, and the AMIs calculated at these locations should be different in times and amplitudes. The AMI values shown in Figure 5.4(a) exhibit a global pattern on the whole, with significant variations among the different

stations. We can see the difference not only on the time of the change from a low to a high level, but also on the amplitudes among stations. This is in agreement with the recognition that the magnetosphere has both global and multiscale features [Ukhorskiy *et al.*, 2002; Sharma *et al.*, 2005]. It should however be noted that the multiscale features are now evident from the spatial as well as temporal variations, compared to the temporal behavior obtained from the *AL* data alone [Ukhorskiy *et al.*, 2002, 2004].

As the dynamic pressure P_{ram} returns to a normal level and the solar wind magnetic field becomes more northward, the magnetospheric response is less active and all the AMIs decrease to lower levels around DOY 50. After being quiet for about a day, a sharp increase in P_{ram} , and an increase in VB_S , trigger a set of big substorms. The AMIs then return to higher values with wider variations among the stations. The localized integrated mutual information, representing the difference in the magnetospheric responses at the 12 stations to the same solar wind driver, is shown in Figure 5.4(b). As we can see, the enhancement of LIMI is a good synoptic representation of the differences in the local conditions as well as the correlations among them. Also as seen in Figure 5.4(c) and (d), the LIMI values have good correlations with the dynamic pressure P_{ram} and the convective electric field VB_S .

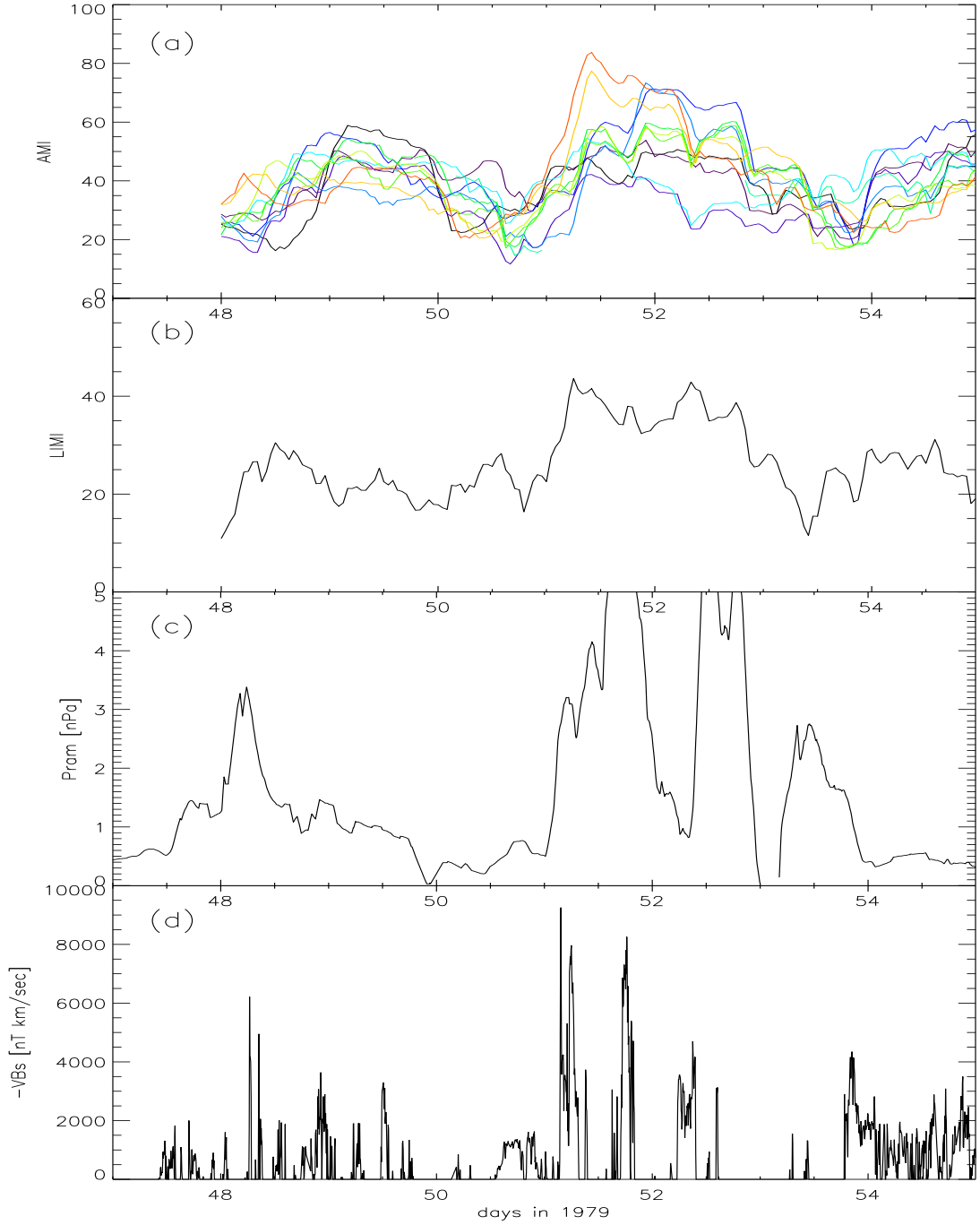


Figure 5.4: (a) Average mutual information for 12 auroral region magnetometers during Feb.16-23, 1979 computed for a moving window of $w = 1$ day. Each line represents a individual station (Table 1) and color coded as in Figure 5.3. (b) The LIMI spread (c) the solar wind dynamic pressure, and (d) the solar wind flow induced electric field VB_s at corresponding times. Each AMI and LIMI point are computed from the previous window length of 1 day, hence the 1-day initial gaps in LIMI and AMI.

5.4.2 Substorm Dynamics from LIM1 with Window Length $w = 6$ hour

The AMIs computed with a 1-day window length yield the local perturbations and their heterogeneity during storm times. However the spatial structure, such as the initial perturbation locations, and the coupling among the locations during an active storm are averaged over all local times. The magnetic field perturbations measured at a ground magnetometer always contain the day-night (positive and negative) periodic variations during both quiet and active periods. The effects of this day-night variation can be avoided to a large extent, by choosing a shorter sliding window within this periodicity, so that the computed AMIs correspond to similar local times or the local spatial regions. There are other considerations related to the choice of the time scales. First, $\tau = 30$ min is the time delay used in the computation and the length of a window should be much longer than τ . Because of the time delay τ , the maximum computational length used is $L - \tau$, L being the total length of the sliding window. To make the distribution of the effective dataset $L - \tau$ close to the actual distribution of the whole datasets, we need $L \gg \tau$. Second, the substorms usually last from several tens of minutes to several hours and the length of data should cover more than a whole substorm in order to extract its dynamical features. Based on these considerations, a 6-hour length window is a proper choice for computing the AMIs to study the dynamical variations characteristic of a localized region and for comparing the dynamics among different locations in longitude.

The AMIs for the 12 stations computed using a 6-hour sliding window for the same storm as Figure 5.4(a), viz. 16-23 February 1979 (DOY47-54), are shown in Figure 5.5(a). Unlike Figure 5.4(a), the variations of AMIs show strong fluctuations on shorter time scales. The intersections of different color lines indicate the complexity of the magnetosphere and the average or global behavior is now harder to define. Following the definitions of AU and AL , we use the upper and lower envelopes of all 12 AMI values of the individual stations to compute two new quantities AMIU and AMIL, and these are shown in Figure 5.5(b). A comparison of AMIU and AMIL with AU and AL , respectively, in Figure 5.5, shows that AMIU and AMIL are similar to AU and AL indices, which are directly derived from the magnetic field perturbations. The correlation of AMIU- AU and AMIL- AL are 0.61 and 0.73, respectively. The similarities of AMIU and AMIL with AU and AL show that the feature of the magnetosphere perturbations described by AU and AL are captured by AMIs. Although the plots of AMIU and AMIL are similar to the geomagnetic indices, AMIU and AMIL measure relationships, linear as well as nonlinear, among the multiple stations at the different locations instead of the maximum and minimum values of the perturbations. Thus the complexity of the spacial structure of the magnetosphere can be characterized by AMI which includes both temporal and spatial information. The AMIU measures the minimum correlation during one sub-storm period among the globally distributed magnetometers, while AMIL measures their maximum correlation.

In order to examine the magnetic field variations independent of the effects due to the rotation of Earth, the data are projected on 12 virtual regions with 30°

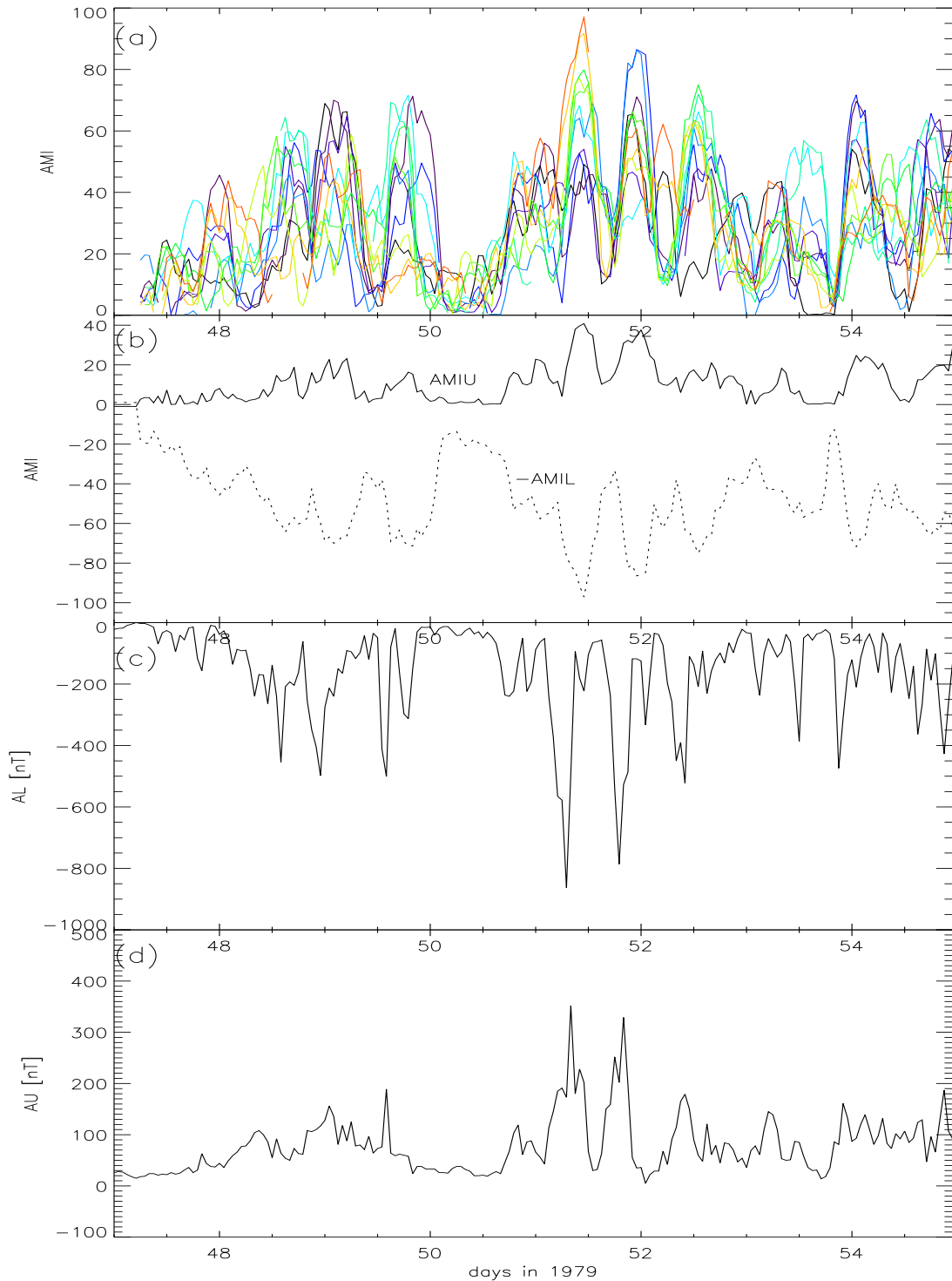


Figure 5.5: (a) Average mutual information for moving windows ($w = 6$ hours) from 12 auroral region magnetometer stations during Feb.16-23, 1979. Each line represents an individual station, and color coded as in Figure 5.3. (b) Upper and lower envelopes of the superposed plots of all moving AMI. (c) AL and (d) AU indices.

extent uniformly distributed in the high latitude region of magnetosphere, starting from noon and moving towards dusk. The AMIs are computed by using the linear interpolations from the 12 known stations in the Solar Magnetic (SM) coordinate system. In this coordinate system, the 12 virtual regions or sectors are fixed in the high geomagnetic latitude region of the Earth, and do not rotate with Earth, and thus are like 12 stationary detectors monitoring the magnetic field variations at any instant. The AMIs based on these 12 virtual fixed stations are shown in Figure 5.6(a). Unlike the many intersections of the data from different stations (color lines) in Figure 5.5(a), the greenish lines representing the virtual stations close to the midnight sectors are systematically above the bluish color lines representing the virtual stations close to the noon sectors, indicating that the AMIs of the stations close to the midnight sectors are higher than those of the stations close to the noon sectors. The AMIs with color ranges from dark green to light green correspond to the time series data with the center $[t - 3hour, t + 3hour]$, $t \sim 12 - 18hour$ in SM coordinate system. Figure 5.6(b) is a color map plot showing the evolution of the AMIs at the 12 virtual stations during 1979 February 16-23 (DOY 47 - 54) storm period. The entire storm evolution is clearly depicted in Figure 5.6(b). The substorm activity starts at DOY 47 and the AMIs start to increase in the midnight sector, then it gradually expands to the dusk and dawn sectors. After reaching the maximum expansion at DOY 49, AMI values decrease in the near-midnight sectors. One day later, another larger scale change in AMIs starts expanding from the midnight sectors to the dawn and dusk flanks, even reaches the dayside sectors, and then returns to the smaller AMI values corresponding to those of quiet time

periods. The substorm expansion starts in the midnight and post midnight sectors, and then the perturbations gradually expand to a wider region between the dusk and dawn sectors, extending up to the dayside sectors. The largest perturbations are located in the near midnight regions, consistent with the substorm phenomenology [McPherron, 1995].

5.4.3 Longer Time Scale Features of LIMI

In order to compare the localized integrated mutual information spreads with localized autocorrelation spreads, these quantities are computed for the entire January-June 1979 dataset with a window width $w = 1440$ minutes (1 day) and 1 min resolution. Figure 5.7(c) shows the time evolution of LIMI, or $\Delta_I(t)$, defined by Equation 5.5, while Figure 5.7(e) shows the autocorrelation spread $\Delta_A(t)$ defined by Equation 5.8. We note that there are apparent features of 5.7(c) that are not present in 5.7(e). Also the mean AMI of the 12 stations is shown in Figure 5.7(d). To assess the role of solar wind activity in the variations of Figure 5.7(c), we compare the results of LIMI, mean AMI and autocorrelation spread with VB_S and P_{ram} . From the mean AMI in Figure 5.7(d), we note that the increases in the AMI values have good correspondence with the variations in the solar wind VB_S and P_{ram} , especially with VB_S shown in Figure 5.7(a). The appearance of sudden maxima in $\Delta_I(t)$ is found to correspond to abrupt changes in the solar wind variations. However, this correspondence is not clear in the spread in the autocorrelation, shown in Figure 7(d). Figure 5.7 suggests that the $\Delta_I(t)$ maxima are associated with the abrupt changes

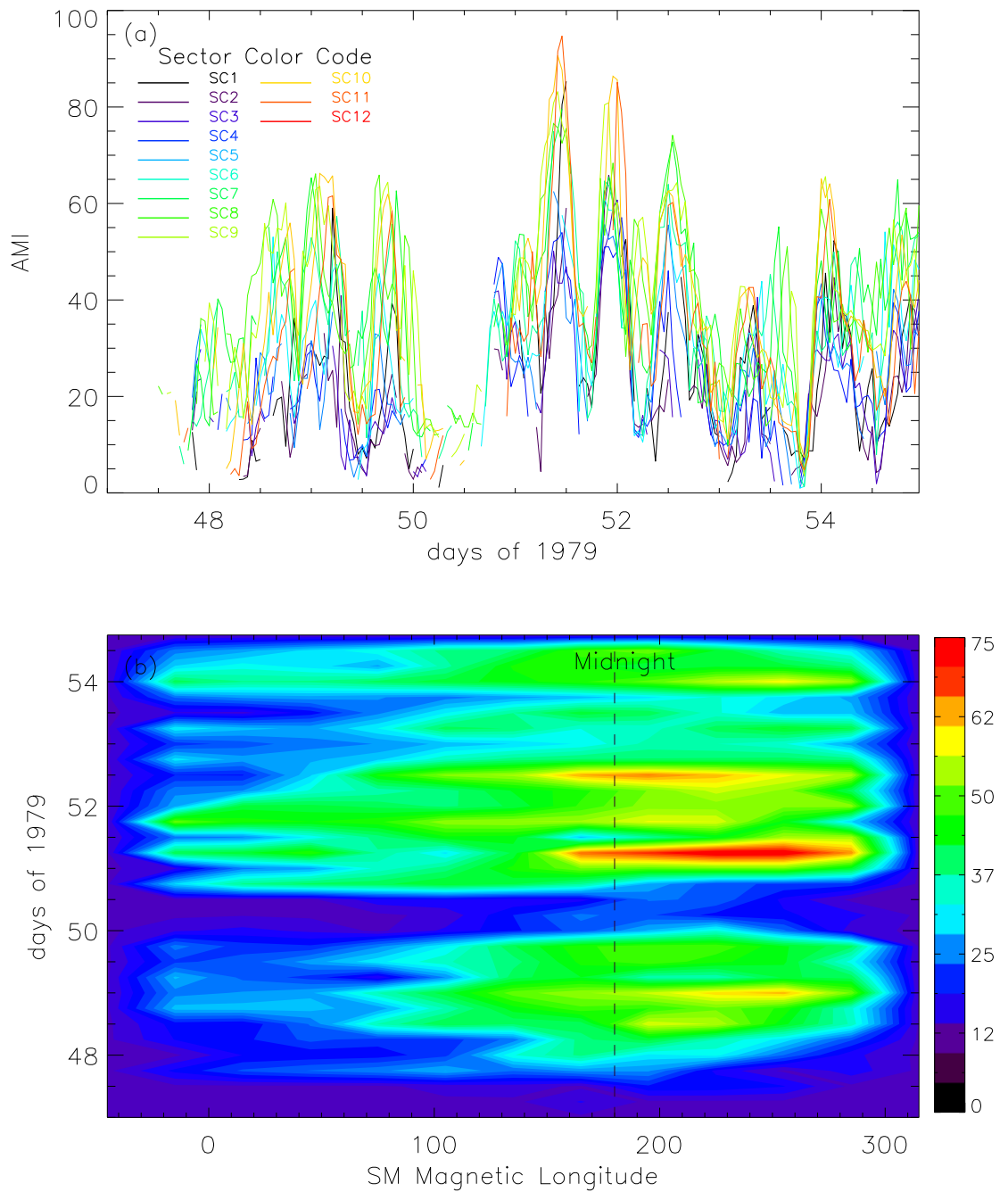


Figure 5.6: (a) Average mutual information with moving window of $w = 6$ hours for 12 sectors under the Solar Magnetic (SM) coordinate system during Feb.16-23 (DOY 47 - 54), 1979. Each line represents one virtual individual station; (b) The time evolution of AMI of 12 sectors. Dashed line represent the midnight sector. (12 sectors SC1-SC12: sectors starting from noon with 2-hour apart and its numbers increasing toward dusk.)

in P_{ram} and VB_S . Although, the correlation between sudden changes in VB_S with the peaks in $\Delta_I(t)$ is not exactly one-to-one, a peak in $\Delta_I(t)$ corresponds to strong variations in the solar wind. Also, the mean AMI always shows a good correlation with the solar wind changes. During extended period of southward interplanetary magnetic field and high dynamic pressure, the corresponding mean AMI values are always high, as shown in Figure 5.7(d). To further compare the LIMI and the mean AMI with the solar wind convective electric field VB_S , comparisons of the LIMI and the mean AMI of 12 stations with the solar wind VB_S are plotted on Figure 5.8(a) and (b), respectively. In order to examine the comparison clearly, LIMI and mean AMI are averaged over a bin size of 0.02 of the normalized VB_S , and this shows that the average AMI follows clearly a linear relationship with VB_S at both low values and saturates at higher values. LIMI shows a linear relationship with VB_S over a large range of the solar wind activity, and a wider scatter at higher activity levels.

5.5 Spatio-Temporal Dynamics Averaged over 6 and 24 hr Windows

The average mutual information function is applied to the data of local magnetic field variations using two window lengths of $w = 6$ hours and 24 hours and yields many interesting features. The 6-hr window covers a quarter of the auroral region, and the 24-hr window covers the entire dayside and nightside. The 24-hr window gives a longer and global scale information and the 6-hr window gives a shorter and localized information. From Figure 5.7, it is apparent that $\Delta_I(t)$ maxima correspond to the main solar wind disturbances, *viz.* VB_S and P_{ram} . Almost all

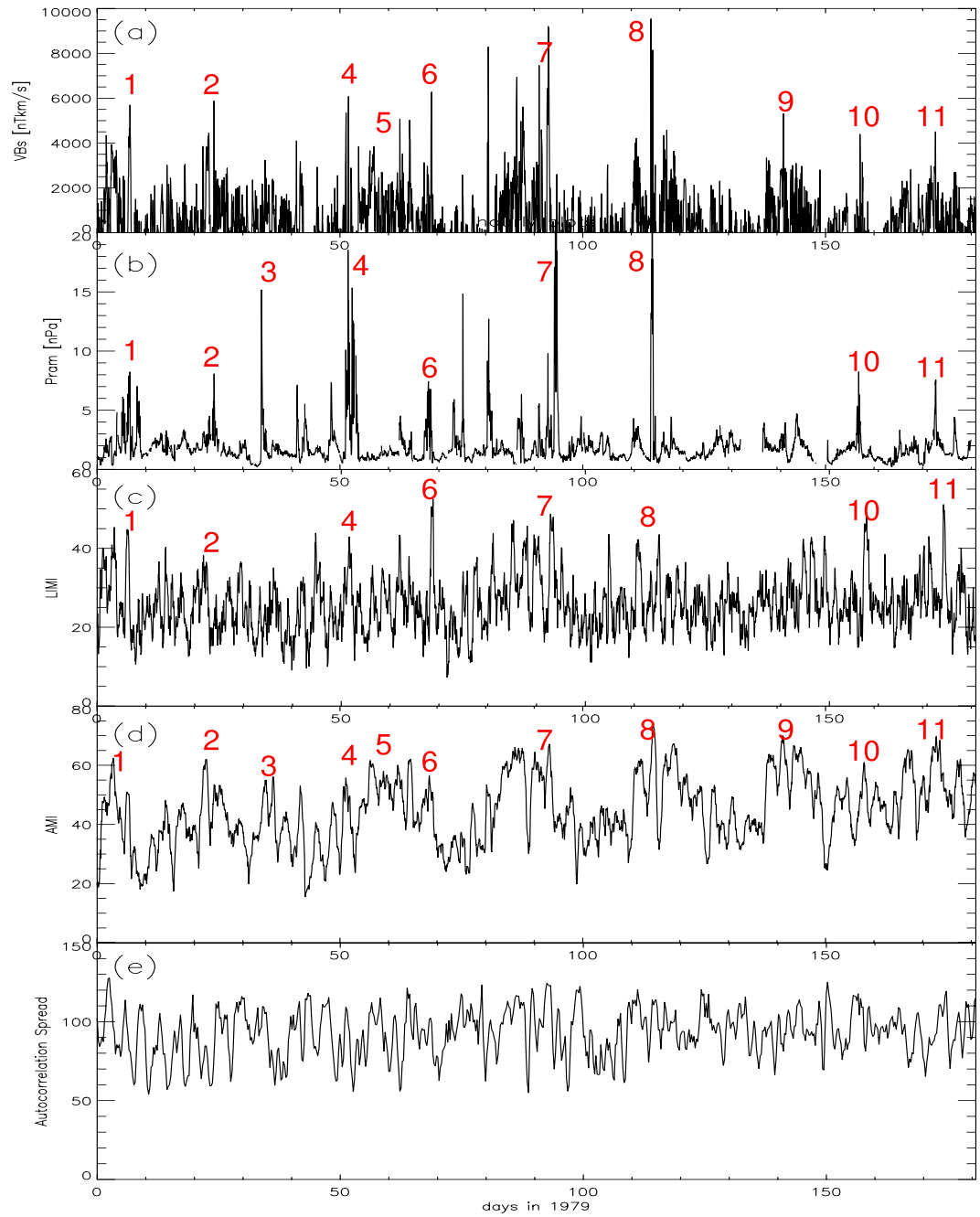


Figure 5.7: (a) Solar wind VB_S . (b) P_{ram} . (c) The spread in LIM computed with 24 hr moving windows during first 6 months of 1979. (d) Moving window ($w = 1$ day) calculation of AMI during first 6 months of 1979. (e) Moving window ($w = 1$ day) calculation of autocorrelation spread during the same period.

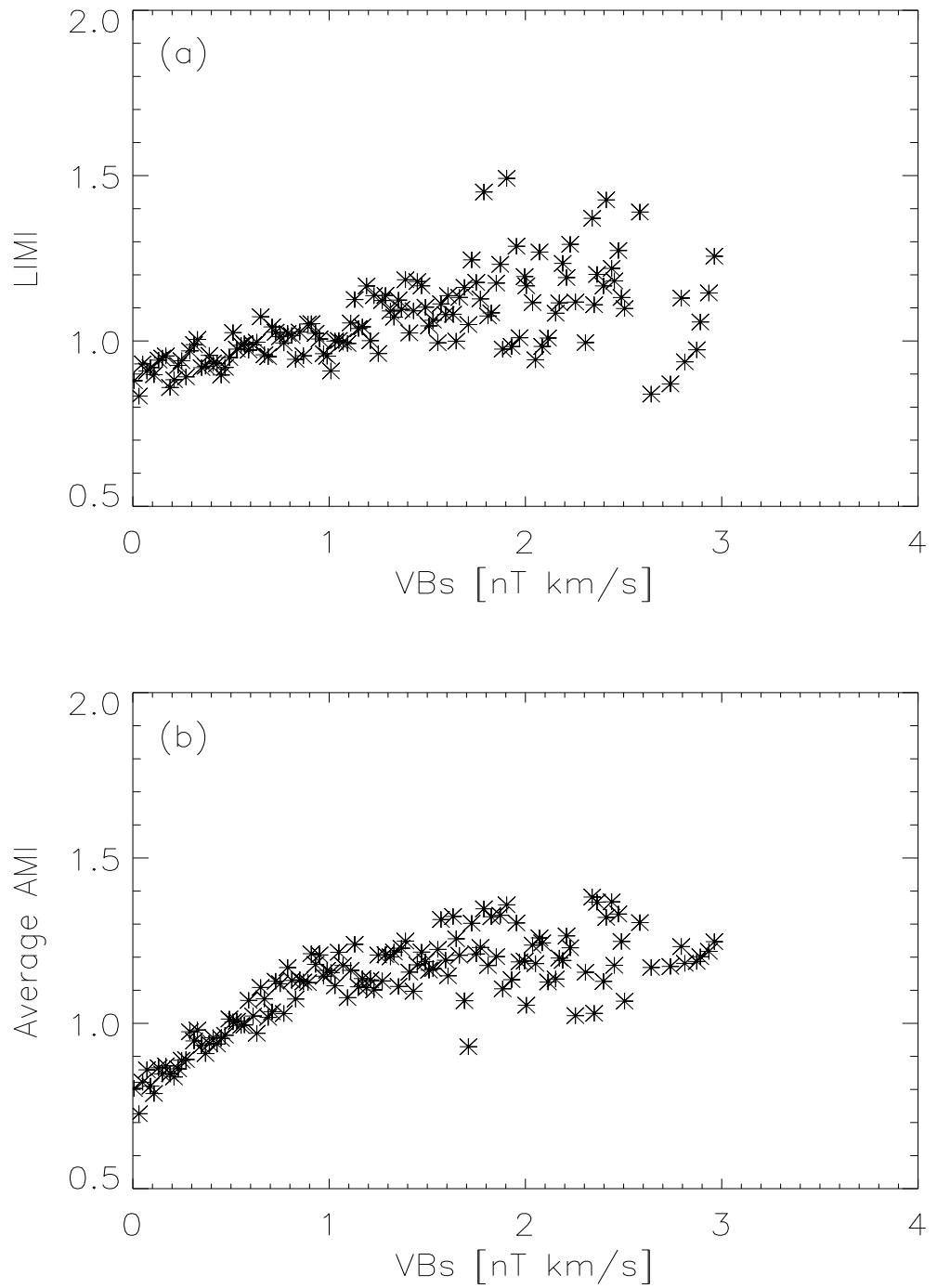


Figure 5.8: Comparison of the LIMI, AMI with the simultaneous VB_s . (a)The correlation between VB_s and LIMI at sizebin=0.02 of normalized VB_s during first 6 months of 1979. (b)The correlation between VB_s and Average AMI at sizebin=0.02 of normalized VB_s during the same period.

of the large perturbations result in large values of $\Delta_I(t)$, indicating a close connection between the magnitudes of the disturbances and LIMI. The magnitude of LIMI reflects the differences in the magnetospheric activities at different spatial locations, and relates to different levels of solar wind input conditions, particularly to the different magnitudes of the solar wind dynamic pressure (Figure 5.9). Figures 5.9(a) and (b) show two substorm epochs on DOY 78 and DOY 90, both corresponding to high values of the solar wind magnetic field, but with different magnitude of dynamic pressure. On DOY 80, driven by a high dynamic pressure and a significant VB_S , the AMIs of all 12 stations increase almost simultaneously and the increases in the amplitudes at individual stations are similar, leading to a high value of the mean mutual information and a moderate mutual information spread. But with a moderate dynamic pressure level and a high value of VB_S , the AMIs of individual stations rise at different times and with different amplitudes, which cause a large mutual information spread. These results can be interpreted in terms of the physical processes underlying substorms. With a southward interplanetary magnetic field, magnetic reconnection is enhanced at the magnetopause and the magnetic flux flows downtail, resulting in an unloading process and the growth of the westward electrojet current in the nightside ionosphere. This nightside current expansion is localized and the magnetometers register these effects with appropriate delays and with different amplitudes. This results in a wide range of the time scales of the auroral expansion at the different stations. However, with a sudden change in the dynamic pressure, the magnetopause is strongly compressed, thus facilitating a simultaneous expansion, and the entire magnetosphere is perturbed at approximately the same

time. The AMIs of all stations show the near simultaneous response in Figure 5.9(a), corresponding to nearly simultaneous activation and homogeneous scale variability over the entire auroral region.

It is clear from Figure 5.7, that the average mutual information function can resolve the spatial dependence and time scales, while the commonly used autocorrelation function cannot. To further compare the performance of these two functions to the spatially distributed time series data, we computed the autocorrelation function (Equation 5.8) for the storm of February 16-23 (Figure 5.6). A 6 hour data window is used to compute the autocorrelation spread and 12 virtual stations fixed in the magnetosphere to measure the spatial variation in the same manners as in the case of mutual information function. The autocorrelation spread on these 12 virtual stations during DOY 47-54 are shown in Figure 5.10(a) and its 2D plot is shown in Figure 5.10(b). Unlike in Figure 5.6(a), where the greenish color lines are always above the bluish color lines, the lines in Figure 5.10(a) show strong irregularity. All color lines intersect each other and represent the values of the autocorrelation at different locations do not have a systematic difference. Also as seen in the 2D plot of Figure 5.6(a), there is an apparent local maximum in the night sector during a strong storm. The region of high autocorrelation values appear not only on the night sector, but are also seen in the day sector. During the storm of DOY 48-49, there variations in the autocorrelation function do not indicate a clear picture of the westward current expansion during a substorm, which are seen in the previous studies [*Kidd and Rostoker, 1991; McPherron, 1995*]. The average mutual information function, on the other hand, is seen to be an appropriate method to describe

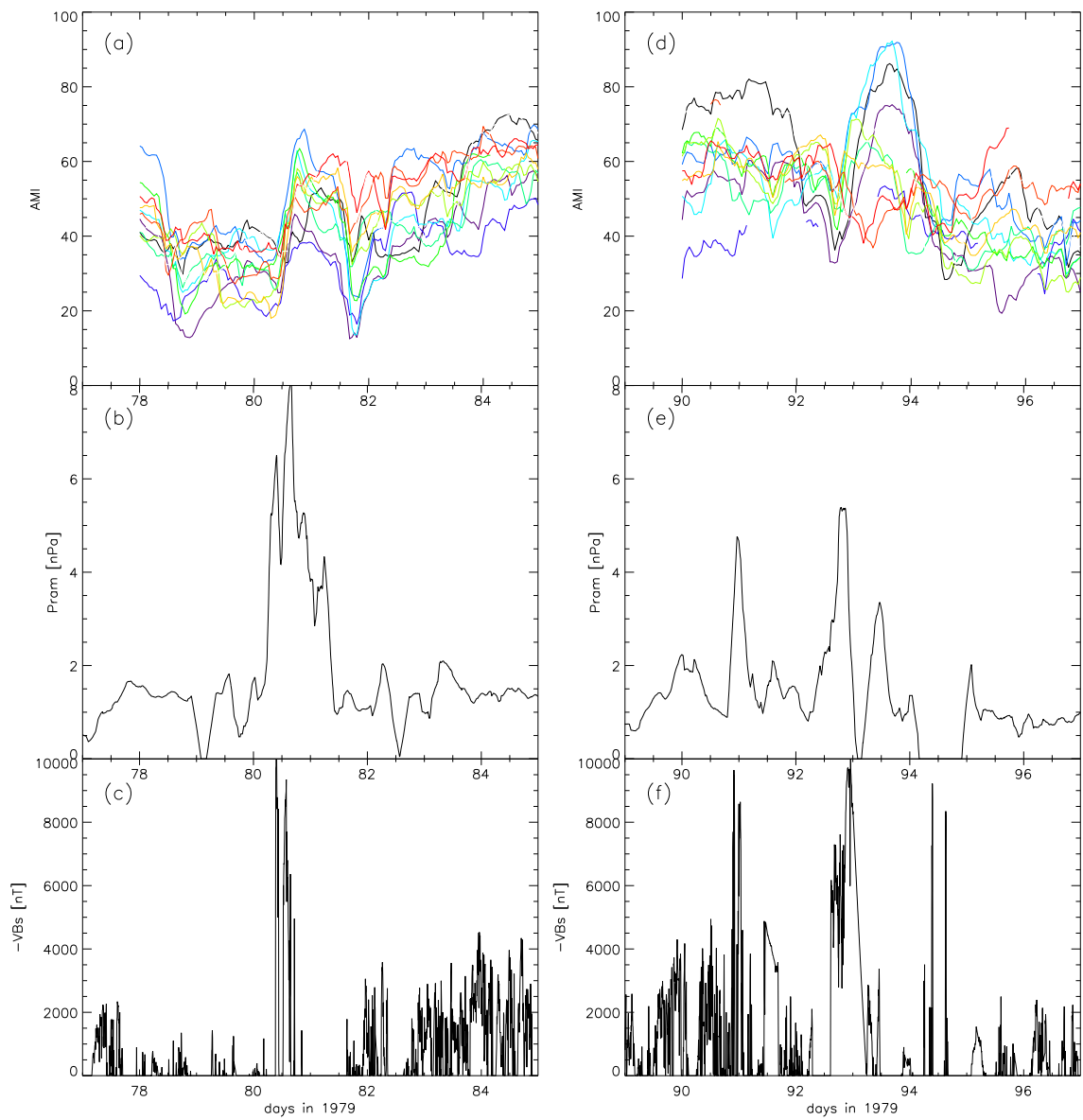


Figure 5.9: (a) AMI during March 19, 2006 (DOY 78) for $w = 6$ hour. (b-c) Corresponding VB_S and P_{ram} . (d) AMI during April 01, 2006 (DOY 90), and corresponding VB_S (e) and P_{ram} (f). The color codes are the same as in Figure (5.3).

changes in the variation in the ionospheric currents during substorms. Furthermore, we conclude that this spatial dependence has a strong nonlinear component, since generalized nonlinear statistics are necessary to isolate such behavior. For the cases with different w values, the inability of the autocorrelation functions to reveal the magnetospheric response to sudden changes in the solar wind is apparent. Clearly, for $w > 3$ days, the appearance of significant maxima is effectively eliminated due to the averaging of the probability distributions over different activity levels. This supports the need for using localized complexity measures. If measures are not localized in time, data influenced by qualitatively different processes (with different time scales) are grouped together, and essential information is lost.

The results discussed above show that the average mutual information is a more effective measure of correlation than the commonly used functions, such as linear autocorrelation, for a spatially extended time series data. This conclusion from studies of other nonlinear dynamical systems [*Fraser and Swinney, 1986; Roulston, 1999*] is further strengthened by the results presented here. The information theoretic functionals, such as average mutual information, have a more general applicability than previously recognized and can be used to yield new details of large scale open systems, such as the magnetosphere.

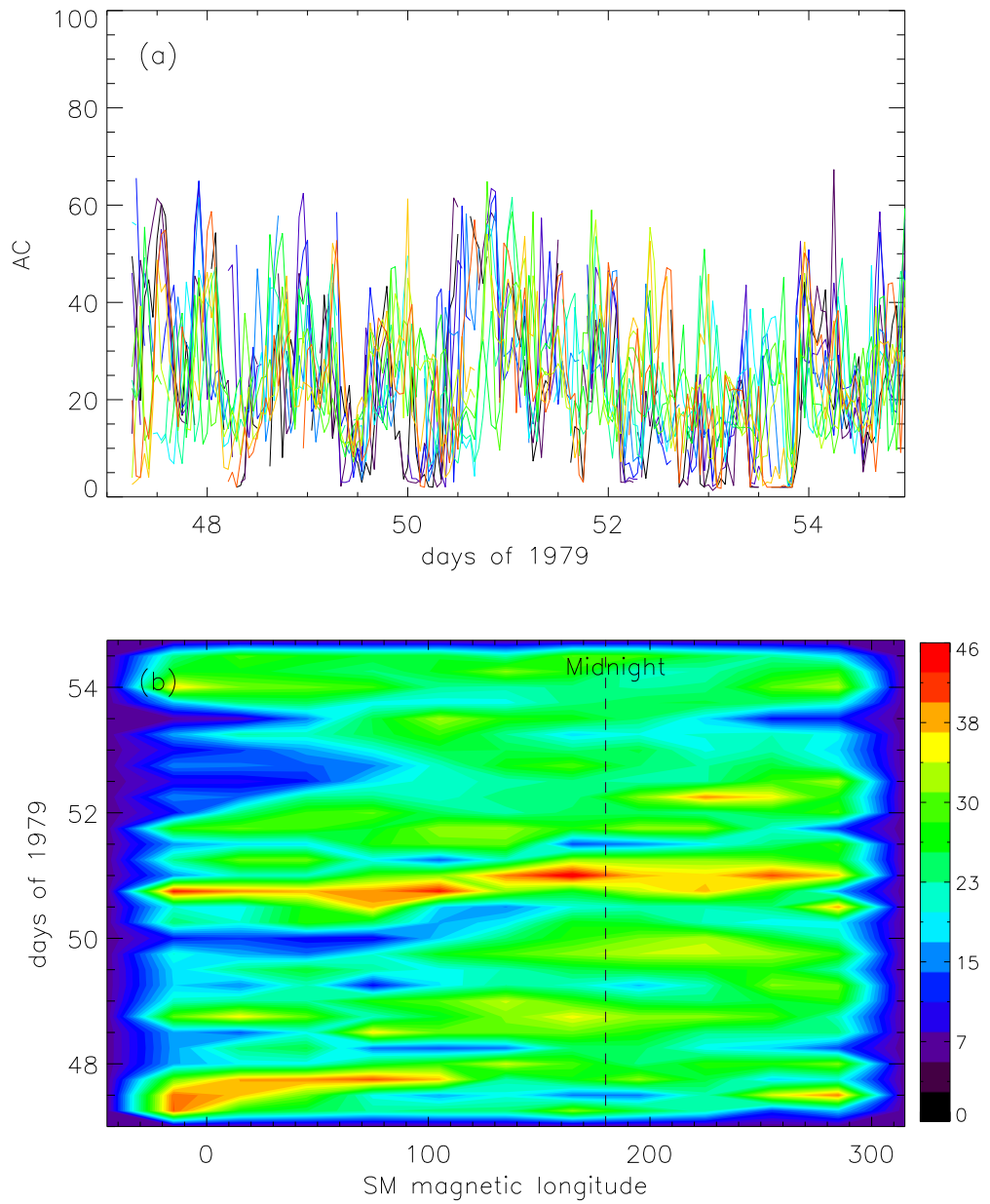


Figure 5.10: (a) Autocorrelation function for 12 sectors in the Solar Magnetic (SM) coordinate system during Feb.16-23, 1979 ($w = 6$ hours). Each line represents one virtual individual station; (b) The time evolution of the autocorrelation functions of the 12 sectors. (same color code as Figure 5.6). Dashed line represent the midnight sector.

Chapter 6

Spatial Structure of the High Latitude Magnetic Perturbations

6.1 Introduction

Ground based observations of ionospheric electrodynamic features are capable of tracking rapid changes in the electric fields and currents, conductivities and associated magnetic field perturbations [*Brekke et al.*, 1974]. However, individual instruments have limited spatial coverage, and many instruments are needed to obtain global coverage of the changing patterns of the electrodynamic feature. Currently some mostly detailed ionosphere electrodynamic information is provided by incoherent scatter radars, but relatively few instruments exist over the world. Magnetometers are much more numerous but do not measure the ionospheric field directly as do the radars. However, they provide complementary information about global electric currents with relatively good spatial coverage. Given the existence of many magnetometers chains around the globe, they became critical to the study of the solar wind-magnetosphere-ionosphere coupling.

The magnetic field variations, measured continuously at a number of locations on the ground, are produced by current systems and result in extensive spatio-temporal data. However, measurements from a large number of ground magnetometers are too variable to provide direct information. Consequently magnetic indices were introduced in the studies of solar-terrestrial physics. As discussed in

earlier chapters, many indices, e. g., *AL*, *AE* and *Dst* are widely used.

The detailed spatial structure of magnetic field, current system, conductance and its related parameters are very important for space physics modeling. These patterns are a direct result of solar wind-magnetosphere-ionosphere interaction, and reflect the flow of plasma and of electric current throughout much of the magnetosphere [e.g. *Burke and Doyle*, 1986; *Mauk and Zanetti*, 1987]. Models of the ionosphere require the details of these parameters in order to simulate the upper atmospheric dynamics, energetics, and chemistry with reasonable accuracy [*Schunk and Szuszczewicz*, 1988]. Also the models of thermospheric dynamics need to details of plasma convection at high latitudes in order to model correctly the effects of ion drag and Joule heating [e.g. *Robel et al.*, 1987; *Rees et al.*, 1987]. Knowledge of the large scale electric fields and current patterns can also be very useful for knowing how to interpret a variety of localized upper atmospheric observations in the global context [*Pellinen et al.*, 1982]. Modeling of inner magnetospheric convection and particle populations require knowledge of the electric potential distribution around the ionospheric poleward edge of auroral oval [*Wolf and Spiro*, 1985; *Senior and Blanc*, 1987]. This requires the details of the spatial patterns of ionosphere and magnetosphere. However, the electrodynamic state of the high latitude ionosphere is highly variable. This variability manifests itself in the global patterns of ionospheric convection and three dimensional electric current systems. While many relevant observations exist, they each typically cover only small portions of the entire high latitude ionosphere, and it has been difficult to synthesize them on a continuous basis. The well-known Assimilative Mapping of Ionospheric Electrodynamics

(AMIE) model is an empirical model derived from the observational data. The AMIE procedure synthesizes the diverse observations of high latitude ionospheric electrodynamics into schematic maps of conductances, electric field, currents and related parameters by using statistical information obtained from the available data [Richmond and Kamide 1988; Richmond, 1992; Knipp et al., 1994; Richmond et al., 1998]. AMIE makes it possible to establish the real-time links to the various important data sources.

Although AMIE is a powerful and useful tool to explore the spatial structure through the coherent pattern of conductivity, electric field and currents, the nonlinear couplings play an important role that requires improvement. The experience gained by AMIE applications so far points as a key improvement of the inclusion of nonlinear coupling effects between the conductivities and the electromagnetic fields. Another drawback of the fitting procedure is the restriction of the number of parameters allowed in the model. These limitations motivate the development of a data derived model using the measurements of magnetic field variation from the high latitude magnetometer arrays.

The shortcomings of the nonlinear global dynamical models in neglecting the spatial dependence have motivated studies of the evolution of the spatial structure of the magnetosphere using the time series data from ground magnetometers. *Valdivia et al.* [1999a] modeled the evolution of the spatial structure of the ring current using the time series data from six mid-latitude ground magnetometers. A similar approach led to a two dimensional representation of the high latitude geomagnetic perturbations in magnetic latitude and magnetic local time from 15 magnetometers

of the IMAGE magnetometer array [Valdivia *et al.*, 1999b]. The role of nonlinearity in the coupling between solar wind parameters and the local magnetic field perturbations was shown in both studies, although the models yield magnetic field perturbation patterns and their corresponding current patterns that are similar to the observations, the prediction errors are very high. The main problems of these models are:

1. The database (1-month) is very short and the prediction is within the same month, which makes the out of sample prediction to be similar to the whole database. Thus there is limited generality for wider usages of the model.
2. The relative prediction errors are too high compared with the original data.
3. The prediction result is only shown for a 12 hour interval, which limit its original day-night variation due to the diurnal variation of Earth.

Considering these and related problems, the difficulties and possible ways for improving the spatial pattern predictions from multi-station observations are studied next.

6.2 Database of Solar Wind-Magnetosphere Coupling

The database of the solar wind key parameters, like V , B_Z , n , from ACE spacecraft (through CDAWEB) and the measurements from ground magnetometer array distributed in high latitude auroral region, like IMAGE and CANOPUS, and from some WDC stations is compiled. The ground magnetometer stations are iden-

tified in Figure 6.1. The database spans 01 January to 31 December 2002 with 1 min resolution, giving $1440 * 365$ data points for each station. All the raw data from IMAGE and CANOPUS are provided with 1 min resolution. After removing the missing and invalid data and replacing them with the interpolated data in the original data series, the coordinate transformation from the Geographic coordinate (GEO) to the Solar Magnetic coordinate (SM) system is used to reflect the rotation of the individual magnetometer stations with Earth. This results in three components of the magnetic field perturbation: $H_x(\lambda, \xi)$, pointing to the geographic north, $H_y(\lambda, \xi)$, to the geographic east and $H_z(\lambda, \xi)$, to the geographic downside, where λ and ξ are the magnetic latitude and longitude of the magnetometer, respectively. In this study, we focus on the components of the horizontal magnetic field perturbation, corresponding the west-east and north-south currents in the polar region.

After the coordinate transformation from geolatitude and geolongitude to SM latitude and SM longitude, Earth's rotation and the tilt between the geographic pole and magnetic pole are taken into account. Now a local magnetometer station is like a monitor rotating with the ionosphere. Since the database is for the entire year, the baseline is chosen as the average value of the 15 quietest days in the year for each component and each magnetometer. This baseline is subtracted from the original data to get the perturbed geomagnetic field.

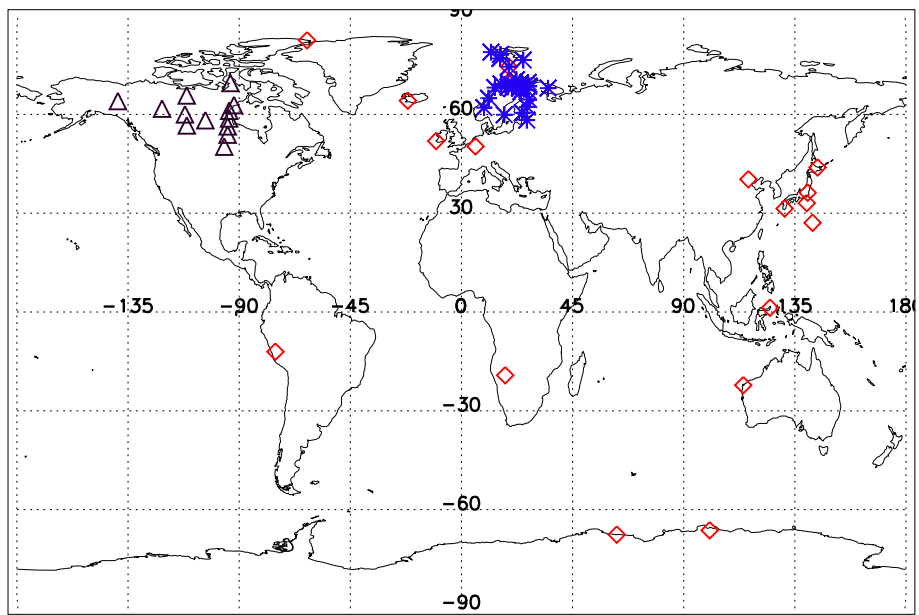


Figure 6.1: The distribution of all available ground magnetometers in year 2002. IMAGE(*), CANOPUS(Δ) and WDC(\diamond)

6.3 Spatial Structure from High Latitude Measurements

The IMAGE and CANOPUS magnetometer array clusters are located in the Europe and Canada, about 180° apart. In our studies, we always use IMAGE and CANOPUS independently, and thus the two datasets and the corresponding model results can be used to study the similarities and differences.

To analyze the properties of the spatial structure of the auroral region during quiet and active magnetosphere periods, an intense magnetic storm of April, 2002 is chosen. During this storm, the interval of April 17-18, 2002 is selected as an intense storm active period and a pre-storm interval of April 1-10, 2002 is selected as a quiet period. The spatial structure of the disturbances during both periods are obtained by averaging the measurements of n days at the same location for each individual station. Either during the active or quiet periods, the 2D perturbation map over the entire period, both in magnetic latitude and magnetic local time is given by:

$$\langle H(\lambda, \xi) \rangle = \frac{1}{n} \sum_{i=1}^n H_i(\lambda, \xi). \quad (6.1)$$

where n is the number of days used in the averaging procedure. The 2D magnetic perturbation for $\langle H_x \rangle$ and $\langle H_y \rangle$ from IMAGE during April 17-18 and April 1-10 are shown on Figure 6.2 and Figure 6.3, respectively. Also the $\langle H_x \rangle$ and $\langle H_y \rangle$ from CANOPUS during the same time are shown on Figure 6.4 and Figure 6.5. In these figures, the top points toward the sun.

During both the active and quiet periods, the maps from IMAGE and CANOPUS show the structured magnetic perturbations. The H_x component is related to

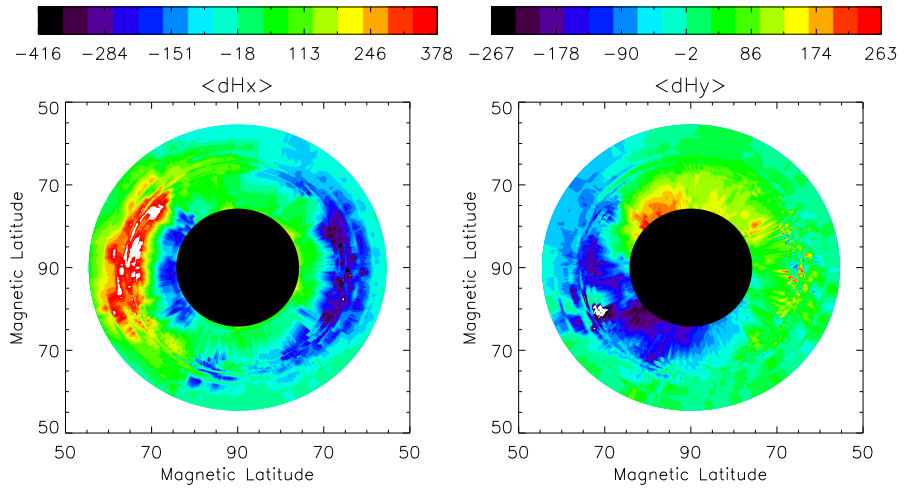


Figure 6.2: The average values of H_x and H_y components measured by IMAGE in both magnetic latitude and local time over April 17-18, 2002 (Storm Period).

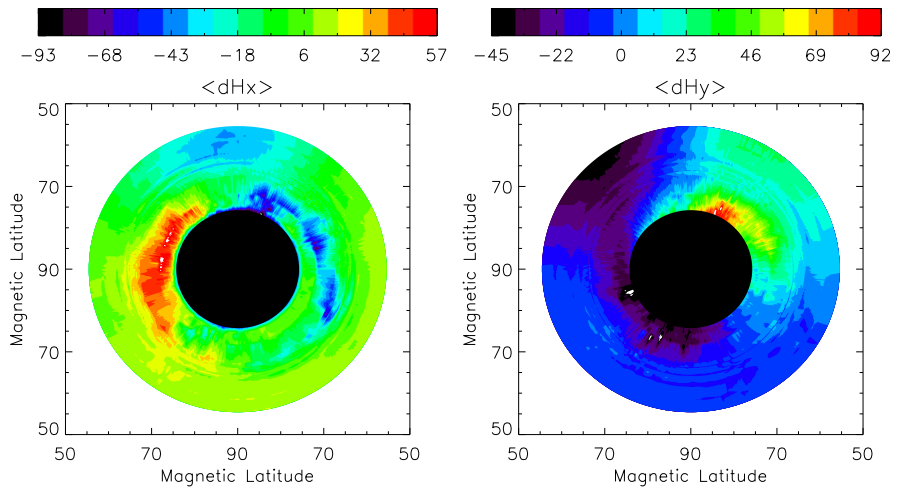


Figure 6.3: The average value of H_x and H_y components measured by IMAGE in both magnetic latitude and local time over April 1-10, 2002 (Quiet Period).

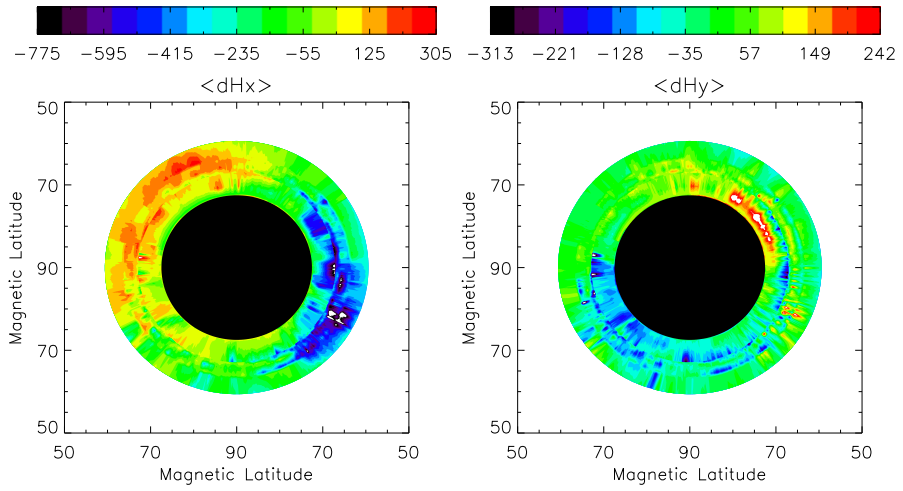


Figure 6.4: The average value of H_x and H_y components measured by CANOPUS in both magnetic latitude and local time over April 17-18, 2002 (Storm Period).

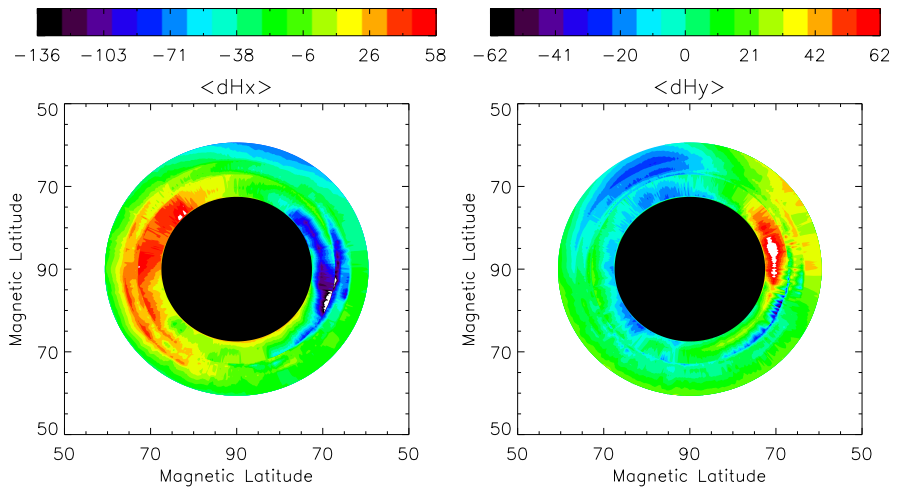


Figure 6.5: The average value of H_x and H_y components measured by CANOPUS in both magnetic latitude and local time over April 1-10, 2002 (Quiet Period).

the east-west component of the auroral current system, and the H_y component is related to the north-south component of the current system. From left left panels of Figure 6.2, 6.3, 6.4 and 6.5, clear patterns of the westward current, associated with a negative H_x in the dawn sector and the eastward current, associated with positive H_x in the dusk sector, are shown.

During the quiet time, as shown in Figure 6.3, the H_x from IMAGE is strongly disturbed close to the center of the area, and has values in the range $[-100nT, 60nT]$. However, during the active time (Figure 6.2), the H_x variations become bigger and equatorward expanding during April 17-18, which indicate the intensification of the westward and eastward currents during the storm time. Compared with the quiet period, H_x of the active period is also highly violent. From the right panels of Figure 6.2-6.5, a small cell of positive H_y values is clear near the dawn sectors, and a region of negative H_y is shown near the dusk sectors. The counterclockwise movement of H_y cell from quiet period to active period indicate the motion of the north-south currents. The same phenomenon also can be seen in the CANOPUS data, shown in Figure 6.4 and 6.5.

Using the infinite plane approximation, we can compute an equivalent current pattern of the eastward and westward electrojet current systems from both H_x and H_y . From $\nabla \times \mathbf{B} = \mu_0 \mathbf{J}$, we obtain:

$$\mu_0 J_x = \frac{\partial B_z}{\partial y} - \frac{\partial B_y}{\partial z}. \quad (6.2)$$

$$\mu_0 J_y = \frac{\partial B_x}{\partial z} - \frac{\partial B_z}{\partial x}. \quad (6.3)$$

If only the horizontal components of the magnetic field are considered and the vertical components are neglected, $H_z = \Delta B_z = 0$, we get $J_x = -\frac{\partial B_y}{\partial z}$ and $J_y = \frac{\partial B_x}{\partial z}$.

Then

$$\frac{J_x}{J_y} = -\frac{\partial B_y}{\partial B_x} = -\frac{H_y}{H_x}. \quad (6.4)$$

And the equivalent current flow pattern related with H_x and H_y are shown in Figures 6.6 and 6.7 for IMAGE and CANOPUS data, respectively. The westward and eastward electrojet current patterns are clearly seen in these figures. During the quiet time, in the left panel of Figure 6.6, the current near the dawn side shows westward flow and most of the current near the dusk side shows eastward flow. However the inner most part of the current shows westward direction, which is opposite to that of the outside currents. These flows constitute a current cell in the dusk side. During the storm time, as shown on right panel of Figure 6.6, both the westward and eastward currents become much more intense. The direction of the current in the inner part is in a direction opposite to that of the outside current flows and resulting in the two cell convective current patterns. The equatorward expansion of the current is also apparent because the locations of the current with opposite direction move equatorward. Meanwhile on the current flow pattern from CANOPUS in Figure 6.7, we can see the intensification of the westward current. However, we cannot see the current cells on both dawn and dusk sides because the location of the innermost station of CANOPUS is not as close to the north polar region of IMAGE.

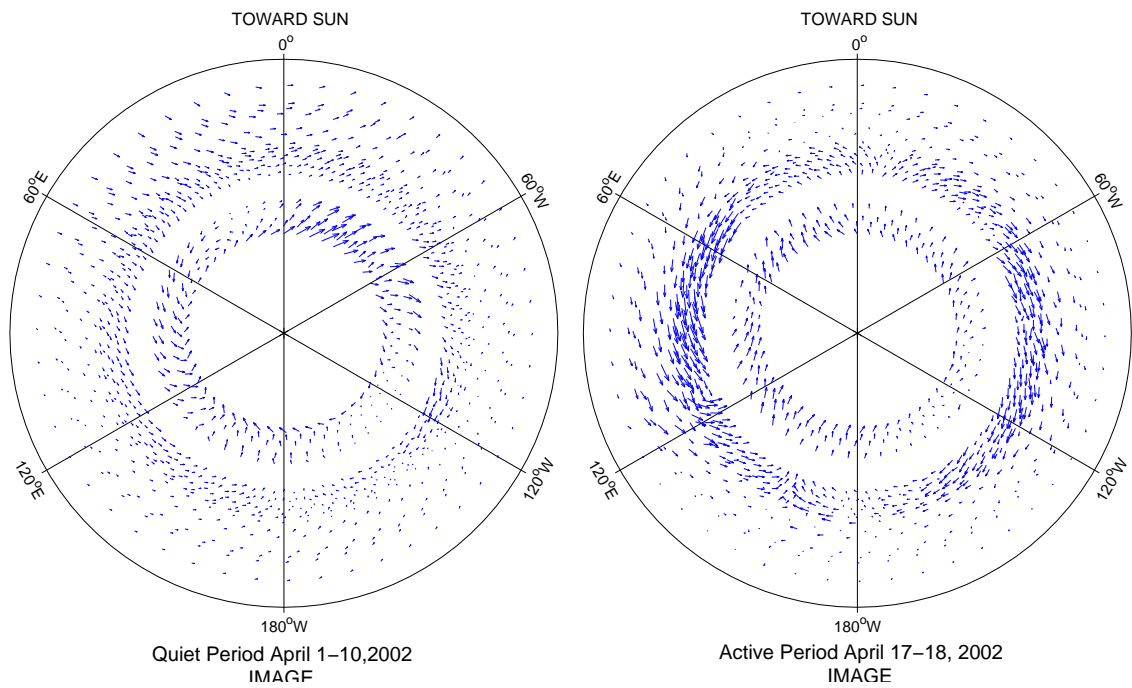


Figure 6.6: Using both H_x and H_y from IMAGE array, the 2D equivalent current patterns are displayed at (a) April 1-10, 2002 (Quiet Period) and (b) April 17-18, 2002 (Storm Period). It clearly shows the westward and eastward electrojet patterns.

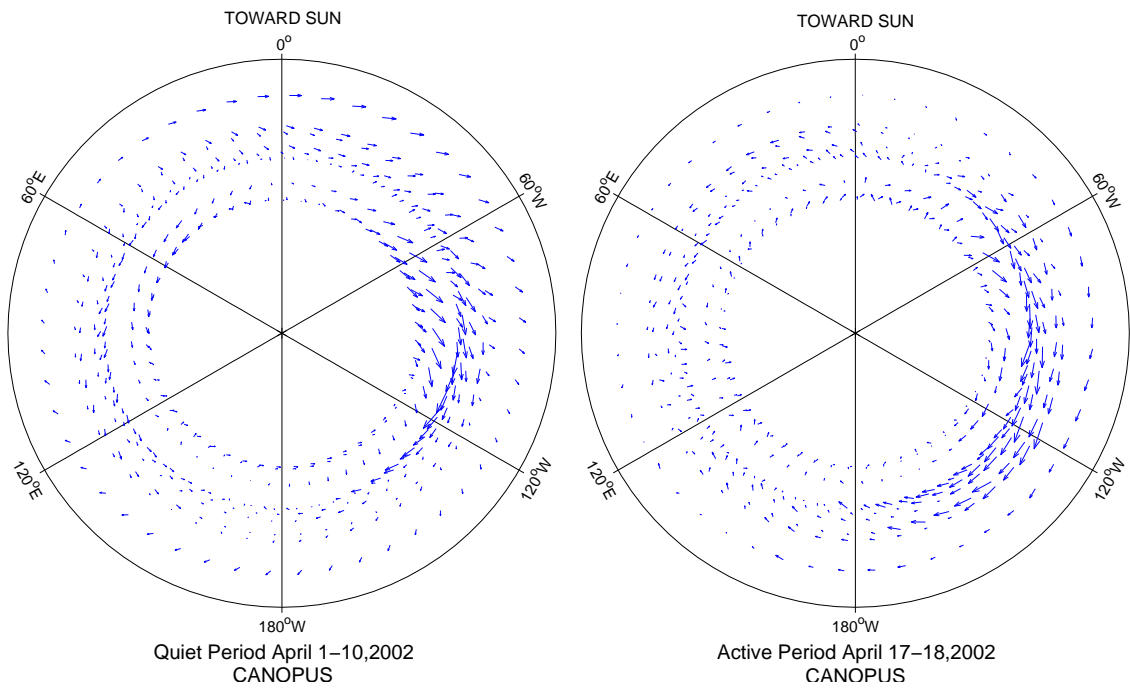


Figure 6.7: Using both H_x and H_y from CANOPUS array, the 2D equivalent current patterns are displayed at (a) April 1-10, 2002 (Quiet Period) and (b) April 17-18, 2002 (Storm Period). It clearly shows the westward and eastward electrojet patterns.

6.3.1 Partition of Distributed Magnetometer Data

The data from ground magnetometer arrays show that there are two cells within the auroral oval, one corresponds to positive magnetic perturbations related with northward enhancement of the magnetic field at dusk, another to negative perturbations related with southward enhancement of the magnetic field at dawn. These show that the magnetic field perturbations have diurnal variation which is positive at dusk and negative at dawn. The measurements of a magnetometer in the high latitude region show positive and then negative variations, as shown in Figure 6.8(a), with the rotation of Earth. Even during storm time, the magnetic field perturbations still show clear day-night variation although this kind of variation is stronger, as shown on Figure 6.8(b). This day-night variation is due to the existence of local currents over the auroral region, and has different patterns from measurements of a mid-latitude geomagnetometer as shown in Figure 6.9(a) and 6.9(b). For a mid-latitude station, the amplitudes of the variations are smaller compared with that at a high latitude station during a quiet period. During a storm time, the magnetic field perturbations always turn southward and no positive northward perturbations even the mid-latitude station is at the dayside, where the magnetic disturbance from a high latitude station always show northward changes as shown on Figure 6.8(b).

The magnetic field perturbations have clear day-night variations and this leads to the question whether we still use the nonlinear data derived models to analyze and predict the magnetic field perturbations at individual stations. Let us con-

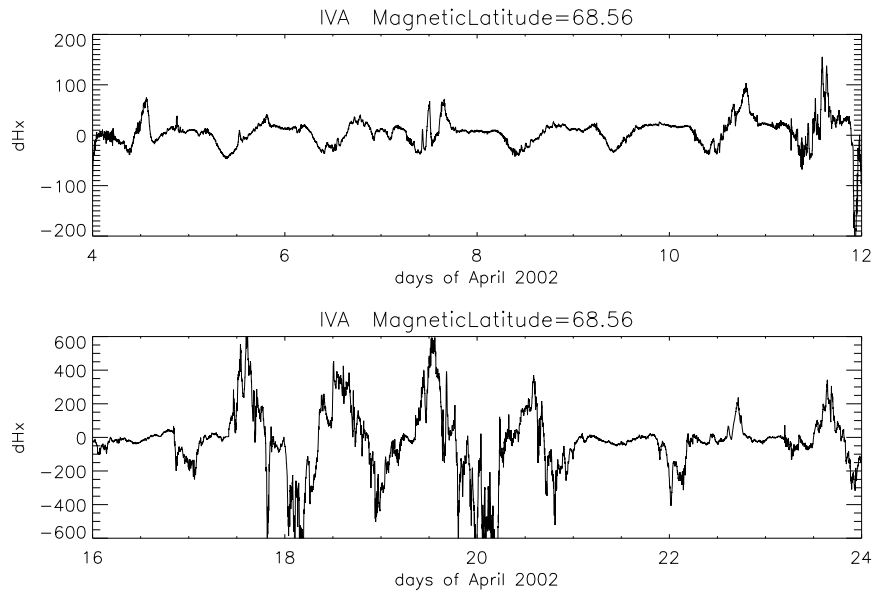


Figure 6.8: The magnetic perturbation H_x at IVA (a high latitude station of IMAGE chain) during April 4-12, 2002 (Quiet) and April 16-22, 2002 (Storm)

sider a storm case, the response represented by AL index does not have localized information because AL is the lower envelope of all station's measurements within auroral zone, and AL actually is the measurement of the westward current close to midnight region when ground stations are distributed uniformly. So the response of the magnetosphere to the solar wind has a one to one correspondence, either linear or nonlinear.

However, for a system of the multiple station measurements (multiple output) with a single solar wind input, the outputs of the system have a spatial dependence. For the same or similar solar wind input, the magnetic field variations at one station might have similar amplitudes and but with opposite phases. Thus the magnetic field perturbations can be positive or negative depending on the location of the

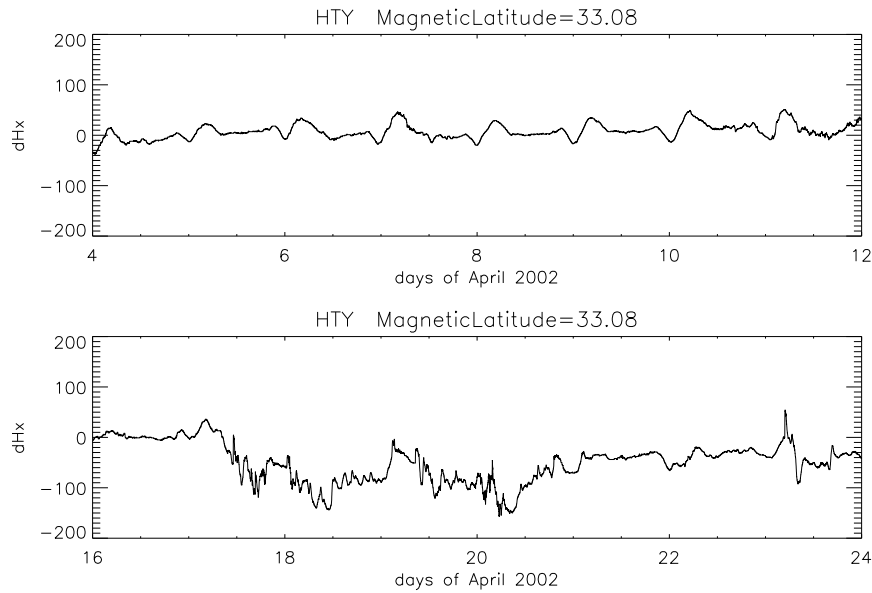


Figure 6.9: The magnetic perturbation H_x at HTY (a middle latitude station of WDC chain) during April 4-12, 2002 (Quiet) and April 16-22, 2002 (Storm)

magnetometer at a given time. When there is no parameter used to identify the location of the magnetometer, the average output value can compensate each other and the prediction results will be close to zero due to the averaging. For example, for a given solar wind condition, the nearest neighbors in the database can be shown in Figure 6.10, such that the vectors 1 and 2 are nearest neighbors of the current state, However the states with opposite phases among the ground stations can lead to cancelations in the local linear filter, and the averaged predicted output H_x can be close to zero.

In order to overcome the above difficulty a new representation of the data is proposed. H_x is measured at discrete magnetic latitude locations, and at discrete times, and these can be mapped to a 2D grid of magnetic longitude and magnetic

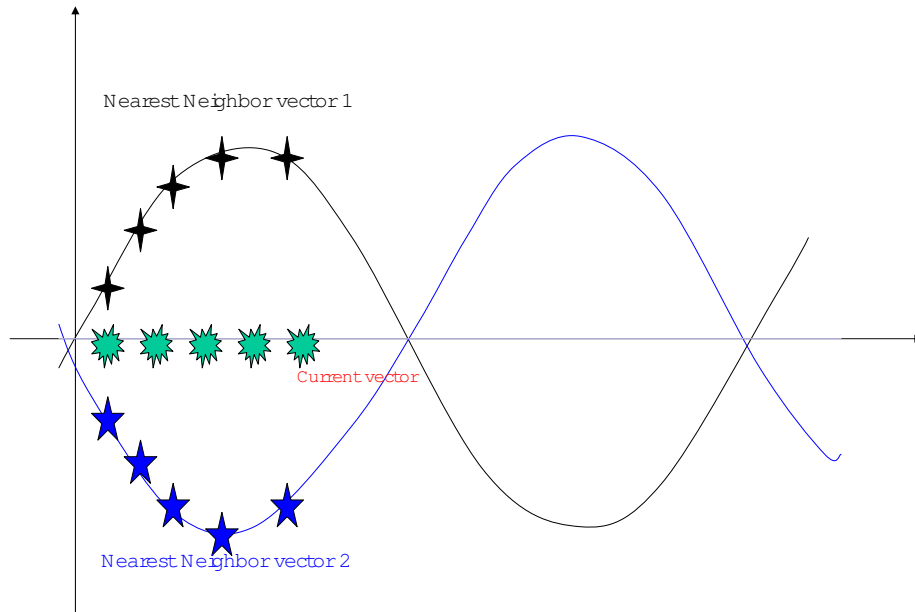


Figure 6.10: Nearest neighbor search and day-night variations. Due to the day-night variation, with similar solar wind condition, both the vectors 1 and 2 are nearest neighbors of the current state. And this can lead to cancelations in the mean-field filter.

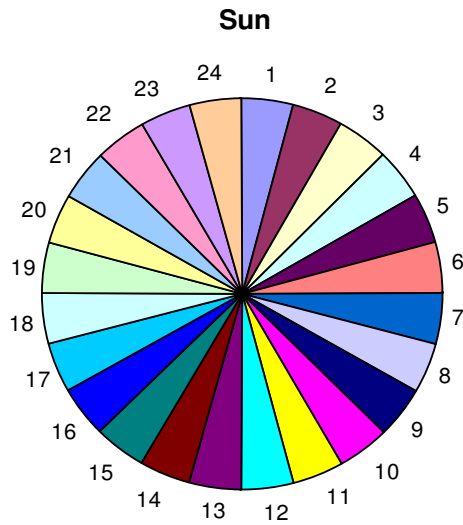


Figure 6.11: Zone partition on high latitude observation. The ground magnetometers of either CANOPUS or IMAGE spread over 15 degrees. The ground magnetometers are within a single zone. Zone 1 is at noon, and Zone 13 is at midnight

latitude. Such a mapping is possible because the magnetometer arrays sample the magnetic fluctuations at all local times as Earth rotates. Because the currents in the ionosphere are always approximately at the fixed locations in the magnetosphere while Earth rotates, the sector with the same magnetic longitude range should measure the magnetic perturbations from the same ionospheric currents. So a 2D mapping provides a feasible way to overcome the effects due to Earth's rotation.

In this representation, the whole polar region is separated to 24 sectors with 15° extension in magnetic longitudes, as shown in Figure 6.11. For each magne-

tometer array IMAGE or CANOPUS, the magnetometer measurements have been partitioned in a 2D grid containing 24 bins in magnetic longitude and N ($N = 26$ for IMAGE and $N = 13$ for CANOPUS) bins, corresponding to each magnetometer, in magnetic latitude λ . Each bin contains $N_t = 60 \times 365 = 21900$ values for a dataset with 1 min resolution. The solar wind input, after 1 hour propagation delay correction, is also partitioned with respect to the time in each bin. So each local time bin contain N_t measurements $H_x(\lambda, \xi_i)$ at the local magnetic longitude ξ_i for $i = 1, \dots, N_t$, with simultaneous solar wind input measurements $E_w(\xi_i)$. By following this procedure, the spatial-temporal is reduced to analysis a case similar as the previous nonlinear global dynamical model.

Unlike the continuous global index AL , the partitioned data set at each magnetic longitude bin are discontinuous and do not correspond well with the solar wind inputs. The magnetic perturbation in the $[\lambda, \xi_i]$ bin is continuous only for every 60 minutes. This discontinuity causes some problems on the phase space vector constructions if the gap between two adjacent datasets is big. The time delay between H_x in bin $[\lambda, \xi_i]$ and the corresponding solar wind is another important issue.

The time delay among the individual station measurements and the solar wind variations is important, especially when using narrowly partitioned zones, and cross-correlation function can be used to determine the proper time delay between two variables (station measurements H_x and solar wind VB_s). Cross-correlations for station NAL at midnight and noon for 3 hour segments are calculated in Figure 6.11. Both the midnight and noon sectors are 3 hour wide. The H_x data for three (1st-3rd day) continuous days at a designated sector and the corresponding

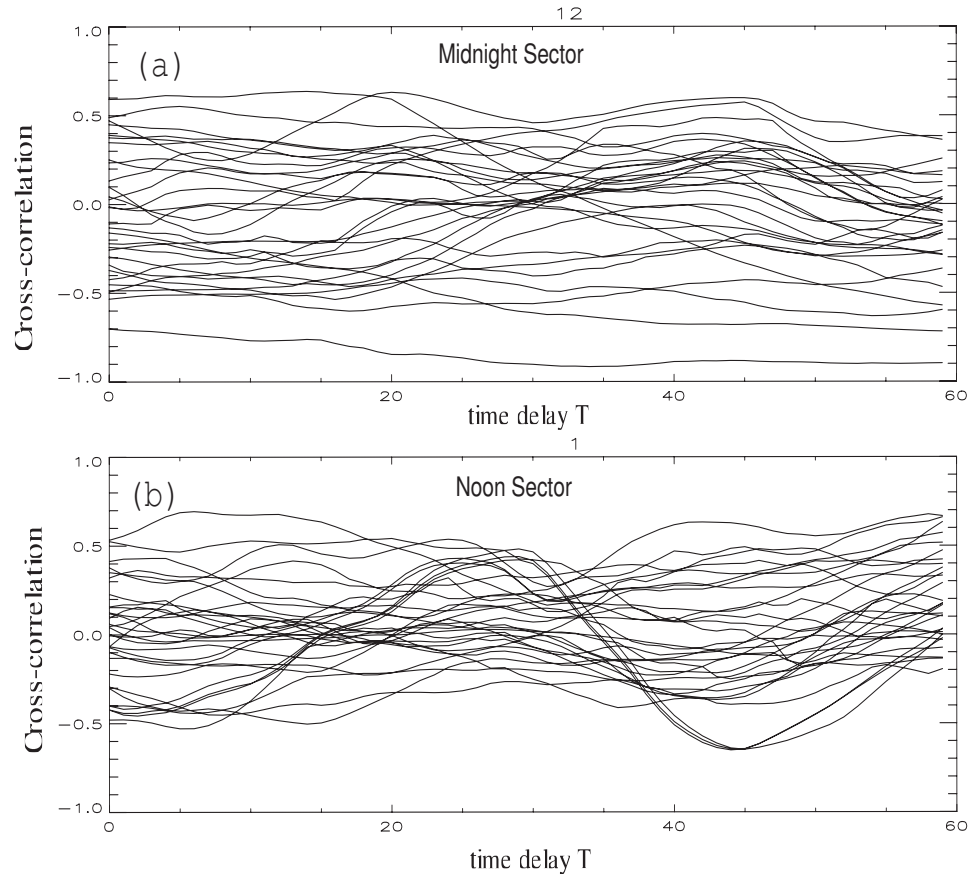


Figure 6.12: Cross-correlations for station NAL at midnight and noon for 3 hour segments. There is no clear peak for a specific time delay T .

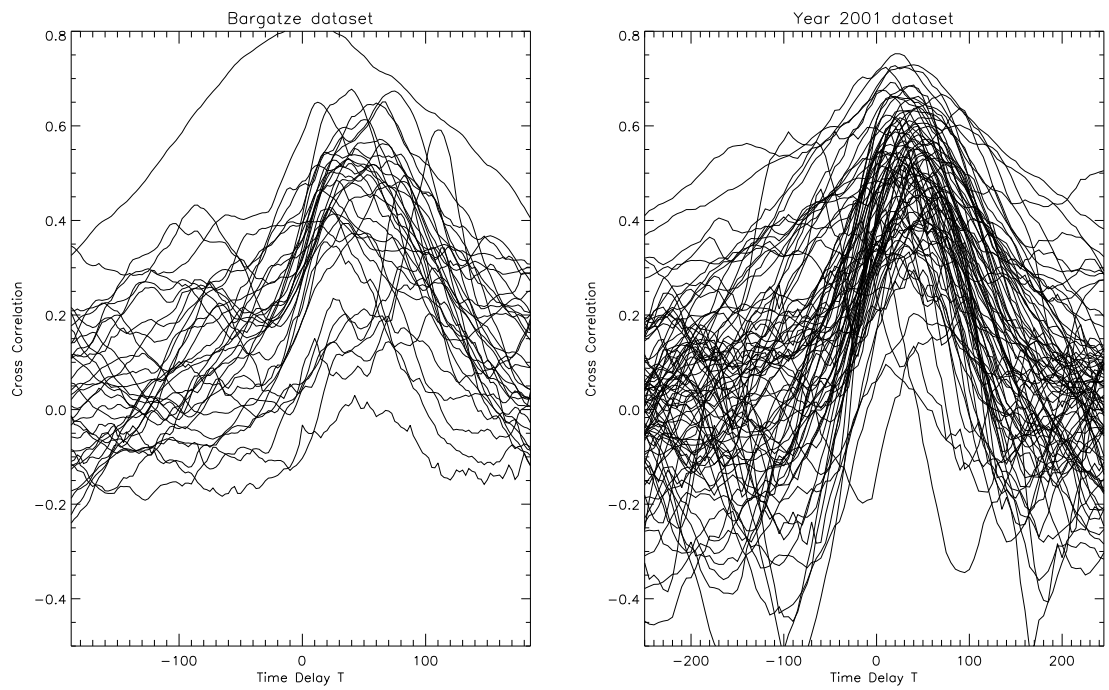


Figure 6.13: Cross-correlations for Bargatze dataset and Year 2001 dataset. Peak for a specific time delay T is clear.

solar wind data (after a correction for the propagation from L1 point) with time delay (0-60 mins) are used. After computing one cross-correlation curve, the data for second three (2nd-4th days) continuous days is selected to compute another cross-correlation curve. A total of thirty 3-day cross correlation curves are shown in Figure 6.12. There is no clear peak for a specific time delay T . The cross-correlations between the solar wind variables and AL index are shown in Figure 6.13, and so clear peaks around $T = 30 - 50$ mins for most of substorm events. This feature is important for the global prediction as the relative fixed time delay make the events in the whole database more uniform and thus suitable for proper predictions. On the other hand the variable time-delays T make the individual station predictions much more difficult.

Using the data of H_x at the stations and solar wind VB_s , the corresponding magnetic field at one IMAGE station MUO at midnight and noon sectors during April 17-18, 2002 are predicted by using local mean field model, as shown in Figure 6.14. Both predictions are under the similar solar wind conditions during the same time, and the predictions on midnight sector show negative perturbation and the predictions on noon sector show positive perturbation. The spatial dependence can thus be predicted by using nonlinear mean field method after the data partitions technique described above.

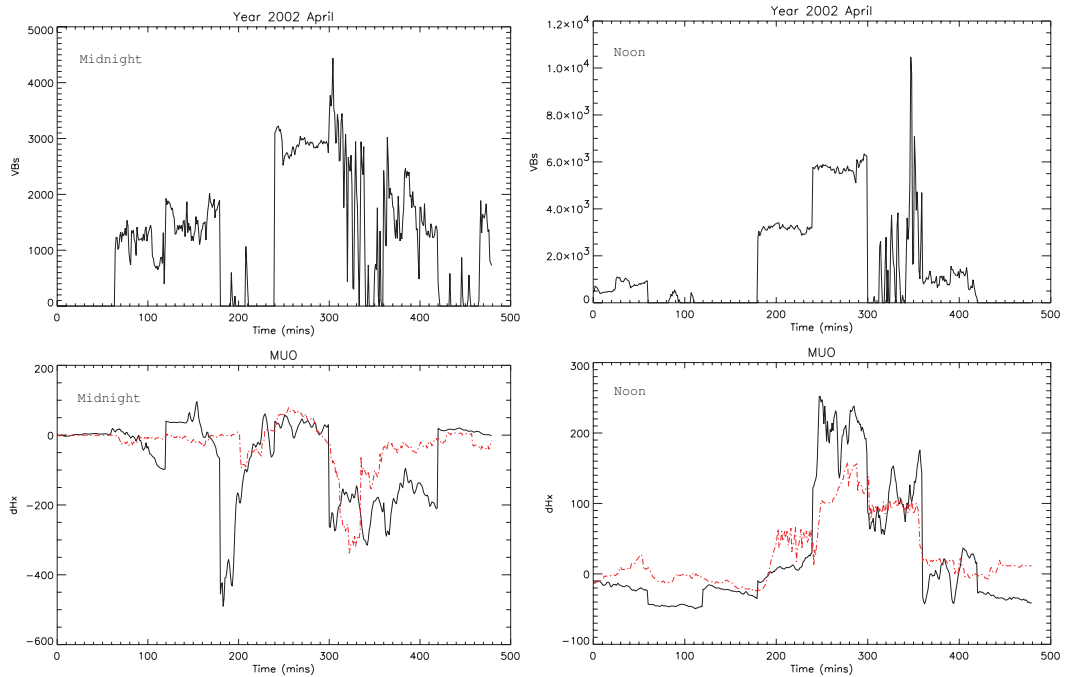


Figure 6.14: Under same days solar wind conditions, the prediction of MUO ground magnetometer (one station of IMAGE) at Noon and Midnight.

6.4 Discussion

A more complete understanding of the nonlinear behavior of the high latitude current system could be achieved with a careful analysis of the evolution of its spatial structure, namely, its spatio-temporal behavior. From the point of view of space weather the predictions of the spatial structure are crucial, as it is important to identify the regions of strong disturbances during intense geospace storms. For this purpose, we have carried out an input-output analysis of the polar region current system using multiple magnetometer measurements from the ground stations as outputs. These efforts are directed towards a comprehensive spatio-temporal model with multiple inputs and outputs.

Contour maps of the horizontal magnetic field perturbation show clear patterns of two cells, negative perturbations at dawn side and positive perturbations at dusk side, corresponding to westward and eastward currents, respectively, in the high latitude region. The corresponding flows of the current systems obtained from the ratio of H_x and H_y clearly show that there is a two cell pattern of the ionospheric current during magnetic disturbances with different directions and different strengths. This spatial structure makes it hard to predict the geomagnetic disturbances at local regions and forecast the spatial structure of geomagnetic disturbances during geospace storms.

The local-linear weighted mean field model can be used to study the magnetic longitude dependent local magnetosphere-solar wind coupling under some conditions. A technique that utilizes the daily rotation of Earth as a longitudinal sampling process is used to construct a two dimensional representation of the high latitude magnetic perturbations both in magnetic latitude and magnetic local time. The nonlinear model can be used to predict the spatial structure of geomagnetic disturbances by combining multiple forecasts from many individual stations. The predictions of the local magnetic perturbation is much more complicated and better techniques are needed. Several challenging issues need to be considered carefully:

1. The gaps between any adjacent dataset within the same longitude sectors cannot be too big.
2. The size of the sector with similar longitude should be as large as possible, which make the continuous data subset large, but in the same time the day-

night variation need to be excluded.

3. The proper time delay between the magnetic field disturbance in a specific sector with solar wind need to be carefully selected to maintain the cause-effect relationship in solar wind-magnetosphere coupling.

To overcome these difficulties, one should choose larger databases which include data during the storm periods with similar features [*Bargatze et al.*, 1985; *Chen and Sharma*, 2006]. The data related with mostly quiet periods should be excluded from the database, and the gaps between the adjacent databases of the same storm event should be smaller. Furthermore the time delay might be similar for most storm periods, thus the time delay between the ground measurements and solar wind condition in each longitude sector will be similar. However, because the entire high latitude region is partitioned to 24 or fewer sectors, in order to maintain the relative large databases for each sector, the one year database is not sufficient as only parts of the data can be selected in each sector during storm times. So a dataset for a large periods, e. g., 5-10 years, might yield better description of the spatio-temporal dynamics.

Chapter 7

Summary

Recent studies of the nonlinear dynamics of the magnetosphere using observational time series data have led to new advances in the understanding of its global dynamics. These studies use the phase space reconstruction techniques developed in the study of nonlinear dynamical systems to build nonlinear models independent of modeling assumptions.

This dissertation presents improved data-derived models, forecasting tools and study the spatial dependence of geomagnetic activity. Two new databases including the magnetic field data from ground magnetometers, and magnetospheric and solar wind data from satellites are compiled for these studies and used to develop the models.

The phase space reconstruction techniques for the spatio-temporal dynamics are implemented in three overlapping parts. First, an improved global model, a weighted mean field filter forecasting tool for the global indices, is proposed and used on the solar wind-magnetosphere coupling during the superstorms of October-November 2003 and April 2002. Second, the mutual information function analysis is applied to the data of local magnetic field variations at high latitude magnetometer stations. It is clear that the average mutual information function can resolve the spatial dependence and time scales, while the commonly used autocorrelation

function cannot. Third, the local-linear weighted mean field model is used to study the spatial dependence of solar wind - magnetosphere coupling. These studies also necessitated the compilation of new databases for the spatio-temporal studies and for periods of intense geomagnetic activity.

1. Weighted mean field filter and its application on superstorms

The mean field model of the global dynamics of the magnetosphere was developed earlier under the assumption that most of the NN nearest neighbor of the current state are similar. However the nearest neighbors are located at different distances from their center of mass, and the closer neighbors should contribute more than those farther away in deciding the predicted state. The new filter, the weighted mean field filter proposed in this dissertation, takes into account the distance of the nearest neighbors and the contributions of the nearest neighbors are weighted by factors inversely proportional to their distance in the reconstructed phase space. Thus in practise, a relative large NN can be selected because the inclusion of nearest neighbors farther away should not affect the prediction significantly as these will have smaller weights, thus making the prediction less sensitive on NN .

This weighted mean field filter can greatly improve the accuracy and efficiency of predictions, especially under some extreme driving by the solar wind, e. g., the three well known superstorms of October-November 2003 and April 2002 [*Chen and Sharma, 2006*]. Earlier prediction studies [e.g., *Vassiliadis et al., 1995; Ukhorskiy et al., 2002, 2004*] used the BBMH [*Bargatze et al., 1985*] dataset corresponding to the declining phase of a solar cycle and containing only a few weak storms. A new database of the whole year 2001, around the peak of solar cycle, is compiled to obtain

the optimal nonlinear weighted mean field filter for these superstorms. A comparison of the prediction results by using these two different databases indicates that the geomagnetic activities during the solar minimum and maximum periods have similar characteristics, thus the year 2001 and BBMH databases can be considered as a complementing each other.

The weighted mean filter closely reproduces the large-scale variations of AL for the three superstorms. Since such storms are uncommon, it is naturally hard to find many similar events in the available databases. So the nearest neighbor searches in these cases yield only a small number states close to the states of the superstorms. Thus using a large number of nearest neighbors with wide variations and with the averaging, the model output is smoothed over these and cannot capture the peaks of the substorms. In such cases the weight factors play an important role and yield improved predictions [*Chen and Sharma, 2006*].

In this study, the global AL index is used as the magnetospheric variable, and the southward IMF is the main driver of the geomagnetic storms. In spite of the improved predictions, the model cannot capture the geomagnetic response due to the effects from the highly enhanced positive IMF. Thus developing a nonlinear dynamical system including the multiple solar wind parameters as inputs is expected to yield better models.

2. Mutual information and its application on spatial dependent magnetospheric perturbations

Along with the development of the global dynamical models on the complexity of the magnetosphere, it is important to understand the correlations among the

different regions of geospace and the mutual information is a suitable function for such studies. The mutual information function stresses statistical relationships and emphasizes both linear and nonlinear dependencies. A key feature of the mutual information function is its ability to yield the linear as well as nonlinear correlations and such functions are needed to study the inherently nonlinear magnetospheric dynamics.

A database of the solar wind data from ISEE3 and IMP8 spacecraft, and ground-based magnetometer data from high latitude stations in 1979 [*Kamide et al.*, 1998] is used to study the magnetospheric response to solar wind variables during geospace storms by computing the mutual information functions for two window lengths of $w = 6$ hours and 24 hours. The 24-hr window covering the entire dayside and nightside gives a longer and global scale information and the 6-hr window covering a quarter of the auroral region gives a shorter and localized representation.

The average mutual information spread, computed from the magnetometer data for the time windows of 24 hours, show strong correlations with the solar wind convective electric field, which are not seen in the linear correlation functions. A westward expansion of the disturbed region is clearly shown in the time evolution of mutual information computed for the time window of 6 hours near midnight sectors.

The mutual information provides a computationally practical tool for the study of a nonlinear, spatially extended driven systems. From the space weather perspective these function, provide the correlations among the different regions, which are critical elements for enabling forecasts of regional, rather than global, conditions. In

the studies presented in this dissertation, the data from the magnetometer stations are used separately. Using the data from any two different stations together will yield the correlation between them, and these will provide more details of the spatial structure of the magnetospheric dynamics.

3. Spatial-temporal dynamics of the magnetospheric response

During geomagnetically active periods, the global features of the magnetosphere are in general captured by the geomagnetic indices and the regional features are measured by ground-based instruments. The time series data of the distributed observations on the ground are used to develop spatio-temporal dynamics of the magnetosphere using phase space reconstruction techniques. In this approach the solar wind - magnetosphere coupling is modeled as an input-output system with the solar wind variables as the input and the 39 ground-based magnetic field variations in high latitude during year 2002 as the magnetospheric response.

A two dimensional representation of the high latitude magnetic perturbations both in magnetic latitude and magnetic local time is constructed by utilizing the daily rotation of Earth as a longitudinal sampling process. The contour maps of magnetic field horizontal perturbation show clear patterns of two cells, negative perturbations in the dawn sectors and positive perturbations in the dusk sectors, which show the westward and eastward currents in the high latitude regions. By mapping the measurements in the magnetic latitude and longitude, a 2D grid is generated with local bins 1 hour apart in longitude. The local-linear weighted mean field model can be used to study the magnetic longitude dependent local magnetosphere-solar wind coupling in the partitioned regions.

The spatial variability of the geomagnetic disturbances make it more challenging to predict them at the individual local regions and forecast the spatial structure of geospace storms. The predictions of local magnetic perturbations at some stations are good but deviate significantly at others. Thus the modeling of spatio-temporal dynamics needs to be studied in more detail and with more extensive databases. A part of the difficulty is due to the way the different stations are affected by different current systems. To overcome this, larger amounts of data for similar conditions are needed. However, in order to maintain the relatively large databases for each sector, 5-10 years of ground observations might be needed.

An immediate application of these models is the development of space weather forecasting tools. The ultimate objective of the space weather program is the development of a suit of operational models that can reliably predict, as far in advance as possible, the effect of solar activity on the magnetosphere. The weighted mean field filter makes the predictions less sensitive on parameters by considering the distribution of the nearest neighbors, and assigning weights to improve the predictions. This approach can make the predictions more feasible.

From the nonlinear dynamical systems perspective, the spatial dependence has strong nonlinear component, since a generalized nonlinear statistic is necessary to isolate such behavior. The mutual information functions computed from the data from pairs of stations will contribute to the understanding of spatial correlation. From the point of view of space weather the predictions of the spatial structure are crucial, as it is important to identify the regions of strong disturbances during intense geospace storms.

In order to yield a more complete understanding of the nonlinear behavior of the magnetosphere, the modeling of its spatio-temporal dynamics is required. The results presented here contribute to this objective. Further studies using more extensive databases and with more refined techniques are directions for future researches.

The future studies of the solar wind-magnetosphere coupling should focus on making accurate, reliable and timely forecasts on the global and regional scales. The accuracy and reliability of regional models as space weather forecasting tools need to be studied in more detail. These models should be compared with the global MHD simulations and other models in order to complement each other. The use of multi-point ground based and satellite data will yield multi-variate models of the dynamical behavior of the different components of geomagnetic activity, identify the dominant physical processes from the data, and complement the first principle models.

Bibliography

- [1] Abarbanel, H. D., R. Brown, J. J. Sidorovich, and T. S. Tsimring, The analysis of observed chaotic data in physical systems, *Rev. Mod. Phys.*, *65*, 1331, 1993.
- [2] Baker, D. N., R. D. Belian, P. R. Higbie, R. W. Klebesadel, and J. B. Blake, Deep dielectric charging effects due to high energy electrons in Earth's outer magnetosphere, *J. Electrostat.*, *20*, 3, 1987.
- [3] Baker, D. N., A.J. Klimas, R.L. McPherron, and J. Buchner, The evolution from weak to strong geomagnetic activity: An interpretation in terms of deterministic chaos, *Geophys. Res. Lett.*, *17*, 41, 1990
- [4] Baker, D. N., S Kanekal, J. B. Blake, B. Klecker, and G. Rostoker, Satellite anomalies linked to electron increase in the magnetosphere, *EOS*, *75*, 401, 1994.
- [5] Baker, D. N., J. H. Allen, S. G. Kanekal, and G. D. Reeves, Disturbed space environment may have been related to pager satellite failure. *EOS*, page 477, October 6 1998.
- [6] Bargatze, L. F., and D. N. Baker, Magnetospheric impulse response for many levels of geomagnetic activity, *J. Geophys. Res.*, *90*, 6387, 1985.
- [7] Bargatze, L. F., T. Ogino, R. L. McPherron, and R. J. Walker, Solar wind magnetic field control of magnetospheric response delay and expansion phase onset timing, *J. Geophys. Res.*, *104*, 14,583, 1999.
- [8] Broomhead, D. S., and G. P. King, Extrating qualitative dynamics from experimental data. *Physica D*, *20* 217, 1986.
- [9] Burke, W. J., and M. A. Doyle, Interplanetary control of high latitude electrodynamics, *J. Geomagn. Geoelectr.*, *38*, 1115-1141, 1986.
- [10] Casdagli, M., A dynamical systems approach to modeling input-output system, in *Nonlinear Modeling and Forecasting*, edited by M. Casdagli and S. Eubank, pp.265-281, Addison-Wesley Press, Massachusetts, 1992.
- [11] Chen, J., and A. S. Sharma, Modeling and prediction of the magnetospheric dynamics during intense geospace storms. *J. Geophys. Res.*, *111*, A04209, doi: 10.1029/2005JA011359, 2006.
- [12] Chen, J., A. S. Sharma, and X. Shao, Spatio-temporal dynamics of substorm during intense geospace storms, *Proceeding 8th Int. Conf. on Substorms*, impress, University of Calgary Press, 2007.
- [13] Chen, J., A. S. Sharma, J. W. Edwards, X. Shao, and Y. Kamide, Modeling and prediction of the magnetospheric dynamics during intense geospace storms. (submitted to *J. Geophys. Res.*), 2007.

- [14] Clauer, C. R., The technique of linear prediction filters applied to studies of solar wind-magnetosphere coupling, in Solar Wind-Magnetosphere Coupling, Editors Y. Kamide and J. A. Slavin, *Astrophysics and Space Science Library*, Terra Scientific Publishing Company, Tokyo, 126, 2749, 1988.
- [15] Cover, T. M., and J. A. Thomas, *Elements of Information Theory*, John Wiley and Sons, Inc., New York, 1991.
- [16] Davis, T. N., and M. Sugiura, Auroral electrojet activity index AE and its universal time variations. *J. Geophys. Res.* 71, 785, 1966.
- [17] Dungey, J. W., The structure of the ionosphere, or adventures in velocity space, in *Geophysics: The Earth's Environment*, edited by C. DeWitt, J. Hiebolt, and A. Lebeau, p. 526-536, Gordon and Breach, New York, 1963.
- [18] Eckmann, J. P., and P. C. Hohenberg, Pattern formation outside of equilibrium, *Rev. Mod. Phys.*, 65, 617, 1985.
- [19] Edwards, J. W., A. S. Sharma, M. I. Sitnov, K. Papadopoulos, and Y. Kamide, Dynamical time scales of the magnetosphere: Comparisons using geomagnetic indices and magnetometer data, *Eos, Trans. AGU*, 81, Spring Meet. Suppl., Abstract SM61B-05, 2000.
- [20] Fedder, J. A., and J. G. Lyon, The solar wind-magnetosphere-ionosphere current-voltage relationship, *Geophys. Res. Lett.*, 8, 880, 1987.
- [21] Fedder, J. A., and J. G. Lyon, The Earth's magnetosphere is 165 R_E long: Self consistent currents, convection, magnetospheric structure, and processes for northward interplanetary magnetic field, *J. Geophys. Res.*, 100, 3623, 1995.
- [22] Fraser, A. M., and H. L. Swinney, Independent coordinates for strange attractors from mutual information, *Phys. Rev. A.*, 33, 1134-1140, 1986.
- [23] Friis-Christensen, E., M. A. Mcherry, C. R. Clauer, and S. Vennerstrom, Ionospheric travelling convection vortices observed near polar cleft: A triggered response to sudden changes in the solar wind, *Geophys. Res. Lett.*, 15, 253-256, 1988.
- [24] Gallager, R.G., *Information Theory and Reliable Communication*, Wiley, New York, 1968.
- [25] Gershenfeld, N. A. and A. S. Weigend, The future of time series: Learning and understanding: in Time Series Prediction: Forecasting the future and Understanding the Past, Santa Fe Inst. Stud. *In the Sci. of Complexity XV*, edited by A. S. Weigend and N. A. Gershenfeld, Mass., 1993.
- [26] Gombosi, T. I., D. L. Dezeew, C. P. T. Groth, K. G. Powell, and P. Song, The length of the magnetotail for northward IMF: Results of 3D MHD simulations, in *Physics of Space Plasmas (1998)*, edited by T. Chang, and J. R. Jasperse, vol. 15, p. 121, MIT press, Cambridge, 1998.

- [27] Hernandez, J. V., T. Tajima and N. Horton, Neural net forecasting for geomagnetic activity, *Geophys. Res. Lett.*, *20*, 2707, 1993.
- [28] Horton, W., and I. Doxas, A Low-Dimensional energy conserving state space model for substorm dynamics, *J. Geophys. Res.*, *101*, 27223-27237, 1996.
- [29] Horton, W., J. P. Smith, R. Weigel, C. Crabtree, I. Doxas, B. Goode and J. Cary, The solar-wind driven magnetosphere-ionosphere as a complex dynamical system, *Phys. of Plasmas*. *6*, 4178-4183, 1999.
- [30] Horton, W., R. S. Weigel and J. C. Sprott, Chaos and the limits of predictability for the solar-wind-driven magnetosphere-ionosphere system. *Physics of Plasma*. *8*, 2946-2952, 2001.
- [31] Kamide, Y. and W. Baumjohann, Magnetosphere-Ionosphere Coupling, *Physics and Chemistry in Space, v. 23*, Springer, 1993.
- [32] Kamide, Y., W. Baumjohann, I. A. Daglis, W. D. Gonzalez, M. Grande, J. A. Joselyn, R. L. McPherron, J. L. Phillips, E. G. D. Reeves, G. Rostoker, A. S. Sharma, H. J. Singer, B. T. Tsurutani, and V. M. Vasyliunas, Current understanding of magnetic storms: Storm-substorm relationships, *J. Geophys. Res.* *103*, 17,705, 1998.
- [33] Kantz, H., and T. Schreiber, *Nonlinear Time Series Analysis*, Cambridge University Press, Cambridge, UK, 1999.
- [34] Kidd, S. R., and G. Rostoker, Distribution of auroral surges in the evening sector, *J. Geophys. Res.* *96*, A4, 5697-5706, 1991.
- [35] Klimas, A. J., D. N. Baker, D. A. Roberts and D. H. Fairfield, A nonlinear dynamical analogue model of geomagnetic activity, *J. Geophys. Res.*, *97*, 12253-12266, 1992.
- [36] Klimas, A. J., D. Vassiliadis, D. N. Baker and D. A. Roberts, The organized nonlinear dynamics of the magnetosphere, *J. Geophys. Res.*, *101*, 13089, 1996.
- [37] Klimas, A. J., D. Vassiliadis, D. A., Roberts, Data derived analogues of the magnetospheric dynamics, *J. Geophys. Res.*, *102*, 26993, 1997.
- [38] Klimas, A. J., V. M. Uritsky, D. Vassiliadis and D. N. Baker, A mechanism for the loading-unloading substorm cycle missing in MHD global magnetospheric simulation models, *Geophys. Res. Lett.*, *32*, L14108, doi:10.1029/2005GL022916, 2005.
- [39] Knipp, D. J. B. A. Emery, and A. D. Richmond, HairstoG. Lu, Application of the Assimilative Mapping of Ionospheric Electrodynamics (AMIE) procedure to cusp identification, in *Physical Signatures of Magnetospheric Boundary Layer Process*, edited by J. A. Holtet and A. Egeland, pp. 401-420, Kluwer Academic Publishers, Netherlands, 1994.

- [40] Lange, K. , Induktionseffekte in Nordskandinavien- untersucht am Beispiel zweier ostwärts fließenden polarer Electrijets über Skandinavien. Diplomarbeit, Inst. f. Geophys. Uni. Munster, FGR, 1979.
- [41] Lanzerotti, L. J., L. C. Lee, C. G. MacLennan, A. Wolfe, and L. V. Medford, Possible evidence of flux transfer events in the polar ionosphere, *Geophys. Res. Lett.*, *13*, 1089-1092, 1986.
- [42] Lorenz, E.N., Determining nonperiodic flow, *J. Atmos. Sci.*, *20*, 130, 1963.
- [43] Lui, A. T. Y., Chapman S. C., Liou K. et al., Is the dynamic magnetosphere an avalanching system? *Geophys. Res. Lett.*, *27*, 911, 2000.
- [44] Lui, A. T. Y., Multiscale phenomena in the near-Earth magnetosphere, *J. Atmos. Solar Terr. Phys.*, *64*, 125, 2002.
- [45] Lyon, J. G., The solar wind-magnetosphere-ionosphere system, *Science*, *288*, 1987, 2000.
- [46] March, T. K., S. C. Chapman, and R. O. Dendy, Mutual information between geomagnetic indices and the solar wind as seen by WIND: Implications for propagation time estimates, *Geophys. Res. Lett.*, *32*, L04101, doi:10.1029/2004GL021677, 2005.
- [47] Mauk, B. H., and L. J. Zanetti, Magnetospheric electric fields and currents, *Rev. Geophys.*, *25*, 541-554, 1987.
- [48] Mayaud, P. N., *Derivation, Meaning, and Use of Geomagnetic Indices*, pp.96-115, American Geophysical Union, Washington, DC, 1980.
- [49] McComas, D. J., S. J. Bame, P. Baker, W. C. Feldman, J. L. Phillips, P. Riley and J. W. Griffee, Solar Wind Electron Proton Alpha Monitor (SWEPAM) for the Advanced Composition Explorer, *Space Sci. Rev.*, *86*, 563, 1998.
- [50] McPherron R. L., Magnetospheric Dynamics, in *Introduction to Space Physics*, edited by Kivelson, M.G., and C. T. Russell, pp. 400-458, Cambridge Univ. Press, New York, 1995.
- [51] Mersmann, U., Baumjohann, W., Kuppers, F., Lange, K., Analysis of an eastward electrojet by means of upward continuation of ground-based magnetometer data. *J. Geophys.* *45*, 281-298, 1979.
- [52] McComas, D. J., S. J. Bame, P. Baker, W. C. Feldman, J. L. Phillips, P. Riley and J. W. Griffee, Solar Wind Electron Proton Alpha Monitor (SWEPAM) for the Advanced Composition Explorer, *Space Sci. Rev.*, *86*, 563, 1998.
- [53] Packard, N. H., J. P. Crutchfield, J. D. Farmer and R. S. Shaw, Geometry from a time series, *Phys. Rev. Lett.* *45*, 712, 1980.

- [54] Pellien, R. J., W. Baumjohann, W. J. Heikkila, V. A. Sergeev, A. G. Yahnin, G. Marklund, and O. Melnikov, Event study on pre-storm phases and their relation to the energy coupling between solar wind and magnetosphere, *Planet Space Sci.*, *30*, 371-388, 1982.
- [55] Prichard, D. and C. P. Price, Spurious dimension estimates from time series of geomagnetic indices, *Geophys. Res. Lett.*, *19*, 1623, 1992.
- [56] Prichard, D., and J. Theiler, Generalized redundancies for time series analysis, *Physica D*, *84*, 476-493, 1995.
- [57] Prichard, D., J. E. Borovsky, P. M. Lemons, and C. P. Price, Time dependence of substorm recurrence: An information theoretic analysis, *J. Geophys. Res.*, *101*, 15359-15369, 1996.
- [58] Raeder, J., Modeling the magnetosphere for northward interplanetary magnetic field: Effects of electrical resistivity, *J. Geophys. Res.*, *104*, 17357, 1999.
- [59] Rees, D., T. J. Fuller-Rowell, S. Quegan, R. J. Moffett, and G. J. Bailey, Thermospheric dynamics: Understanding the unusual disturbances by means of simulations with a fully-coupled global thermosphere/ionosphere model, *Ann. Geophysical*, *5A*, 303-328, 1987.
- [60] Richmond, A. D. and W. Baumjohann, Three-dimensional analysis of magnetometers array data, *J. Geophys. Res.*, *54*, 138-156, 1983.
- [61] Richmond, A. D., and Y. Kamide, Mapping electrodynamic features of the high-latitude ionosphere from localized observations - Technique, *J. Geophys. Res.*, *93*, 5741-5759, 1988.
- [62] Richmond, A. D., Y. Kamide, B. H. Ahn, S. I. Akasofu, and R. P. Lepping, Mapping electrodynamic features of the high-latitude ionosphere from localized observations - Combined incoherent-scatter radar and magnetometer measurements for January 18-19, 1984, *J. Geophys. Res.*, *93*, 5760-5776, 1988.
- [63] Richmond, A. D., Y. Kamide, S. I. Akasofu, D. Alcayde, and M. Blanc, Global measures of ionospheric electrodynamic activity inferred from combined incoherent scatter radar and ground magnetometer observations, *J. Geophys. Res.*, *95*, 1061-1071, 1990.
- [64] Richmond, A. D., Assimilative mapping of ionospheric electrodynamics, *Adv. Space Res.*, *12*, (6)59-(6)68, 1992.
- [65] Richmond, A. D., G. Lu, B. A. Emery, and D. J. Knipp, The AMIE procedure: Prospects for space weather specification and prediction. *Adv. Space Res. Vol.22*, No.1 pp.103-112, 1998.

- [66] Robel, R. C., J. M. Forbes, and F. A. Marcos, Thermospheric dynamics during the March 22, 1979 magnetic storm, 1, Model simulations, *J. Geophys. Res.*, **92**, 6045-6068, 1987.
- [67] Robert, D. A., Is there a strange attractor in the magnetosphere?, *J. Geophys. Res.* **96**, 16031, 1991.
- [68] Roulston, M. S., Estimating the errors on measured entropy and mutual information, *Physica D*, **125**, 285-294, 1999.
- [69] Ruelle, D., Chaotic Evolution and Strange Attractors, Cambridge Press, Cambridge, UK, 1989.
- [70] Schunk, R. W., and E. P. Szuszczewicz, First-principle and empirical modeling of the global-scale ionosphere, *Ann. Geophysicae*, 1988.
- [71] Senior, C., and M. Blanc, Convection in the inner magnetosphere: Model prediction and data, *Ann. Geophysicae*, **5A**, 405-420, 1987.
- [72] Shan, L. H., Hansen, P., Goertz, C. K., Smith, R. A., Chaotic appearance of the AE index, *Geophys. Res. Lett.*, **18**, 147, 1991a.
- [73] Shan, L. H., Goertz, C. K., and Smith, R. A., On the embedding-dimension analysis of AE and AL time series, *Geophys. Res. Lett.*, **18**, 1647, 1991b.
- [74] Shao X., M. I. Sitnov, A. S. Sharma, K. Papadopoulos, C. C. Goodrich, P. N. Guzdar, G. M. Milikh, M. J. Wiltberger, and J. G. Lyon, Phase transition-like behavior of magnetospheric substorms: Global MHD simulation results, *J. Geophys. Res.*, **108(A1)**, 1037, doi:10.1029/2001JA009237, 2003.
- [75] Sharma, A. S., D. Vassiliadis and K. Papadopoulos, Reconstruction of low-dimensional magnetospheric dynamics by singular spectrum analysis, *Geophys. Res. Lett.*, **20**, 335, 1993.
- [76] Sharma, A. S., Assessing the magnetosphere's nonlinear behavior: Its dimensional is low, its predictability is high, *Rev. Geophys. Suppl.*, **33**, 645, 1995.
- [77] Sharma, A. S., Nonlinear Dynamical Studies of Global Magnetospheric Dynamics, in *Nonlinear Waves and Chaos in Space Plasmas*, edited by T. Hada and H. Matsumoto, pp. 359-389, chap. 11 Terra Sci., Tokyo, 1997.
- [78] Sharma, A. S., D. N. Baker, and J. E. Borovsky, Nonequilibrium phenomena in the magnetosphere, in *Nonequilibrium Phenomena in Plasmas*, edited by A. S. Sharma and P. K. Kaw, pp3-22, Springer Press, Berlin, 2005.
- [79] Sibeck, D. G., W. Baumjohann, R. C. Elphic, D. H. Fairfield, J. F. Fennell, W. B. Gail, L. J. Lanzerotti, R. E. Lopez, H. Luehr, A. T. Y. Lui, C. G. MacLennan, R. W. McEntire, T. A., Potemra, T. J. Rosenberg, and K. Takahashi, The magnetospheric response to 8-minute period strong amplitude upstream pressure variations, *J. Geophys. Res.*, **94**, 2505-2519, 1989.

- [80] Siscoe, G., The magnetosphere: A union of interdependent parts, *EOS, Trans. AGU*, 72, 494, 1991.
- [81] Sitnov, M. I., A. S. Sharma, K. Papadopoulos, D. Vassiliadis, J. A. Valdivia, A.J. Klimas and N. D. Baker, Phase transition-like behavior of the magnetosphere during substorms, *J. Geophys. Res.*, 105, 12955, 2000.
- [82] Sitnov, M. I., A. S. Sharma, K. Papadopoulos, and D. Vassiliadis, Modeling sub-storm dynamics of the magnetosphere: From self-organization and self-organized criticality to nonequilibrium phase transitions, *Phys. Rev. E.*, 65, 016116, 2001.
- [83] Skoug, R. M., J. T. Gosling, J. T. Steinberg, D. J. McComas, C. W. Smith, N. F. Ness, Q. Hu and L. F. Burlaga, Extremely high speed solar wind: 29-30 October 2003, *J. Geophys. Res.*, 109, A09102, doi:10.1029/2004JA010494. 2004.
- [84] Smith, J. P., J. L. Thiffeault, and W. Horton, Dynamical range of the WINDMI model: An exploration of possible magnetospheric plasma states. *J. Geophys. Res.* 105, 12983, 2000.
- [85] Strogatz, S. H., *Nonlinear Dynamics and Chaos. With Applications to Physics, Biology, Chemistry, and Engineering*, Westview, Cambridge, Mass. 2000.
- [86] Takalo, J., J. Timonen, and H. Koskinen, Correlation dimension and affinity of AE data and bicolored noise, *Geophys. Res. Lett.*, 20, 1527, 1993.
- [87] Takens, F., Detecting strange attractors in turbulence, in *Dynamical Systems and Turbulence*, Springer, Berlin, 1981.
- [88] Theiler, J., Spurious dimension from correlation algorithms applied to limited time series data, *Geophys. Phys. Rev.*, A, 34, 2427, 1986.
- [89] Torres, M. E., and L. G. Gamero, Relative complexity changes in time series using information measures, *Physica A*, 286, 457-473, 2000.
- [90] Tsurutani, B., M. Sugiura, T. Iyemori, B. E. Goldstein, W. D. Gonzalez, S-I Akasofu, and E. J. Smith, The nonlinear response of AE to the IMF Bs, *Geophys. Lett.*, 17, 279, 1990.
- [91] Ukhorskiy, A. Y., M. I. Sitnov, A. S. Sharma, and K. Papadopoulos, Global and multiscale aspects of magnetospheric dynamics in local-linear filters, *J. Geophys. Res.*, 107,1369, 2002.
- [92] Ukhorskiy, A. Y., M. I. Sitnov, A. S. Sharma, and K. Papadopoulos, Global and multiscale features in a description of the solar wind-magnetosphere coupling, *Ann. Geophys.*, 21(9), 1913, 2003.
- [93] Ukhorskiy, A. Y., M. I. Sitnov, A. S. Sharma, and K. Papadopoulos, Global and multi-scale features of solar wind-magnetosphere coupling: From modeling to forecasting, *Geophys. Res. Lett.*, 31, L08802, doi:10.1029/2003GL018932, 2004.

- [94] Valdivia, J. A., A. S. Sharma, and K. Papadopoulos, Prediction of magnetic storms by nonlinear models, *Geophys. Res. Lett.*, *23*, 2899, 1996.
- [95] Valdivia, J. A., D. Vassiliadis, A. Klimas, A. S. Sharma, and K. Papadopoulos, Spatiotemporal activity of magnetic storms, *J. Geophys. Res.*, *104*, 12239-12250, 1999a.
- [96] Valdivia, J. A., D. Vassiliadis, A. Klimas, and A. S. Sharma, Modeling the spatial structure of the high latitude magnetic perturbations and the related current systems, *Phys. of Plasmas*. *6*, 4185-4194, 1999b.
- [97] Vassiliadis, D. V., A. S. Sharma, T. E. Eastman, and K. Papadopoulos, Low Dimensional chaos in magnetospheric activity from AE time series, *Geophys. Res. Lett.*, *17*, 1841, 1990.
- [98] Vassiliadis, D., A. J. Klimas, D. N. Baker, and D. A. Roberts, A description of the solar wind-magnetosphere coupling based on nonlinear filters, *J. Geophys. Res.*, *100*, 3495-3512, 1995.
- [99] Weigel, R. S., W. Horton, and T. Tajima, Forecasting Auroral Electrojet Activity from Solar Wind Input with Neural Networks, *J. Geophys. Res.*, *26*, 1353-1356, 1999.
- [100] Wolf, R. A., and R. W. Spiro, Particle behavior in the magnetosphere, in *Computer Simulation of Space Plasma*, edited by H. Matsumoto and T. Sato, pp.227-254, Terra, Tokyo, 1985.
- [101] Wu, J. G., and H. Lundstedt, Prediction of geomagnetic storms from solar wind data using Elman recurrent neural networks, *Geophys. Res. Lett.*, *23*, 319, 1996.
- [102] Wu, J. G., and Lundstedt, Neural network modeling of solar wind-magnetosphere interaction, *J. Geophys. Res.*, *102*, 14457, 1997.
- [103] Zhou, X., and B. T. Tsurutani, Rapid intensification and propagation of the dayside aurora: Large scale interplanetary pressure pulses (fast shocks), *Geophys. Res. Lett.*, *26*, 1097-1100, 1999.